Synthesis and characterization of B-substituted nanoporous carbon with high energy of hydrogen adsorption

Katarzyna Walczak

THÈSE POUR OBTENIR LE GRADE DE DOCTEUR DE L'UNIVERSITÉ DE MONTPELLIER

En PHYSIQUE

École doctorale Université de Montpellier

Unité de recherche Université de Montpellier

Synthesis and characterization of B-substituted nanoporous carbon with high energy of hydrogen adsorption

Présentée par KATARZYNA WALCZAK
Le 13 Décembre 2018

Sous la direction de Professeur LUCYNA FIRLEJ
et Professeur CATHERINE JOURNET-GAUTIER

Devant le jury composé de

ÉRIC ANGLARET, Président du jury, Professeur des universités

CATHERINE JOURNET-GAUTIER, Membre du jury, Professeur des universités

BOGDAN KUCHTA, Membre du jury, Professeur des universités

LUCYNA FIRLEJ, Directeur de Thèse, Professeur des universités

VIRGINIE HORNEBECQ, Rapporteur, Maître de conférences

CARLOS WEXLER, Rapporteur, Professeur

UNIVERSITÉ
DE MONTPELLIER

\-

"You should not be afraid of anything in life,

you just have to understand it"

- Maria-Curie Skłodowska

PREFACE

The present work constitutes a contribution to the world effort to search for a material that could store hydrogen by physisorption, at ambient temperatures, and moderate pressures. The ultimate goal of this research is to synthetize the material that is cheap, safe, light, and can reversibly store hydrogen in the quantity that will allow its massive use as fuel in fuel cells-powered light vehicles. The detailed list of requirements that hydrogen-operating systems should fulfil to be introduced on the market was formulated by US Department of Energy. It concerns all aspects of the future hydrogen-powered vehicles, from fuel tank and fuelling procedure to operation of combustion engine (fuel cell). Here we focus only on one aspect of this complex problem: the search for a sorbent that could extend the current limits of hydrogen storage at room temperature by physisorption.

The work realized during the thesis consisted in experimental proof of concept that the boron containing nanoporous carbons, theoretically predicted to have large hydrogen storage capacity, can be produced by the electric arc discharge between boron-containing graphite electrodes.

The first chapter of the thesis (*Hydrogen storage – technological challenge*) introduces briefly the problems related to the intensive exploitation of the fossil sources of energy, then reviews the current state of art in developing sorbents for hydrogen storage by physisorption. A special attention is payed to theoretical and experimental works devoted to analysis of applicability of carbon-based materials for hydrogen storage: their synthesis, characterisation and predicted/measured storage capacity, at cryogenic (T = 77 K) and ambient conditions.

The second chapter (*Physical synthesis of nanoporous carbons by electric arc discharge technique and description of characterization methods*) describes the general concept and technical details of physical synthesis of all-carbon and boron-substituted carbon structures in the electric arc. Furthermore, the chapter provides short description of characterization methods used in the present work: microscopies, spectroscopies, X-ray diffraction, and adsorption techniques. Their basic principles are briefly explained to give a reader a necessary background to easily follow the presentation of the results in chapters 3 and 4.

The third chapter (*Characterisation of adsorptive properties of nanoporous carbons prepared by arc discharge technique*) presents the analysis of arc-prepared all-carbon samples. The chapter is divided into two parts, providing samples' characterization successively before

and after activation (by thermal and chemical activation procedures). The detailed description of activation procedures is also provided.

The fourth chapter (*Characterisation of adsorptive properties of nanoporous boron-carbon samples prepared by arc discharge procedure*) focus on characterisation of boron-containing carbon samples. A special attention is devoted to analysis of morphology and structure of boron-reach fragments of the samples, and to evaluation of homogeneity of boron distribution in the material. As for all-carbon samples, the samples' characterisation was conducted both: before and after activation procedure.

The ensemble of presented results constitutes only the first step in exploring of possibility of arc–discharge preparation of substituted nanoporous carbons for efficient hydrogen storage. This study brought to the light more experimental questions that we were able to answer during the limited time allocated to this PhD project. Therefore, chapter five (*Final conclusions and perspectives*) summarizes the obtained results and indicate possible ways to (i) overcome the encountered problems, and (ii) explore other types of substituted carbons.

Acknowledgments

First of all, I would like to thank my supervisor prof. Lucyna Firlej and co-supervisor prof. Catherine Journet-Gautier, for their guidance throughout my Ph.D. thesis. They gave me a permanent support whenever I needed it. They believed in my capability to solve the most intricate problems, and taught me how to become independent, consistent and organized in the future challenges in science.

I would also like to thank the researchers from Madirel in Marseille and from Laboratory Charles Coulomb in Montpellier: prof. Bogdan Kuchta, dr Marie-Vanessa Coulet, dr Phillip Llewellyn, dr Thomas Neisius, dr Christoph Goze-Bac, dr Emily Bloch for experimental help and interpretation of the results, and Fabio Ziarelli (Université Aix-Marseille, SPECTROPOL, Marseille) and Vasile Haresanu (CNAM, Marseille) for making the spectroscopy and diffraction measurements possible.

I would also like to thank for technical support in the laboratories. It was a great pleasure to work with Laurence Bois (Université Claude Bernard Lyon 1; LMI) and Saïd Tahir (Université de Montpellier; L2C) on synthesis and activation experiments.

In all laboratories where I had a pleasure to work (Lyon, Montpellier, Marseille) I had met many students of different nationalities. All of them are exceptional people and it was a pleasure to talk and to spend time together at work and during the outdoor activities. I would like to thank especially my officemates: Christophe for your support, your positive energy and songs we sang together, and Paul for your company, scientific help in adsorption field and glass sculpturing lessons. PHy, Evićka, Damian, André, Rifi, Behnny, Ephy, Alex, Yass, Ping Pong, Khacky: thank you for being a part of my life during my PhD thesis. I hope our friendship will continue this way in the future.

The presence of my best Polish friends Marcelina, Ada and Ola, and their faithful support during the final stages of this PhD was much appreciated.

Finally, I would like to thank my family for all their love and encouragement. My parents, who raised me with a love of science and supported me in all steps I made in this direction. Thank you.

Table of contents

CHAPTER 1

Hydrogen storage – technological challenge

1.1. Introduction

Over ages, energy requirement became one of the most important factors in humans' life. Since XIX century until now fossil fuels (coal, oil, natural gas) are main natural energy sources. They are used to produce the primary forms of energy (electricity, transport fuels) and contribute to industrial evolution which allowed to change almost all aspects of human life.

Fossil fuels created naturally from ancient plants and organisms in carboniferous period hundreds of millions years ago, are considered as non-renewable energy sources at the scale of human life. Fig. 1.1 presents the production of fossil fuels since 1800, and projected until 2200 with the peak of maximum production predicted in 2050 [1.1]. Global energy request inevitably leads to the exhaustion of economically and technically accessible resources in about 200 years. Although a residual amount of fossil fuels will still remain underground at this moment, their geographic location and dispersion of deposits will make them inaccessible, and their extraction energetically expensive and risky.
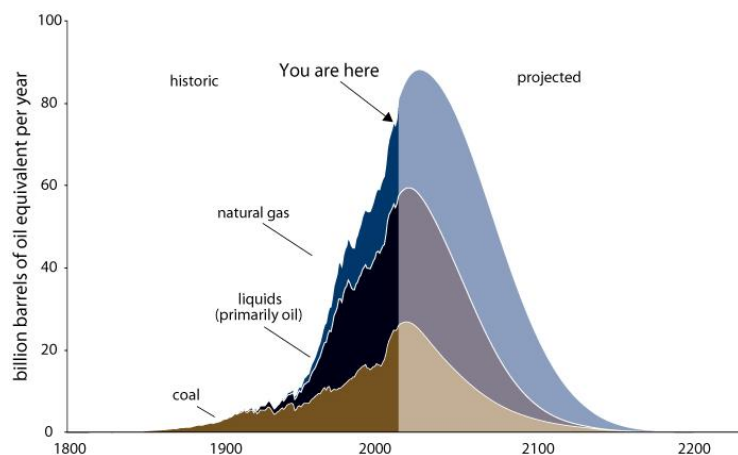
Figure 1.1. Global production of fossil fuels from 1800 to 2200 [1.1].

Additionally, the exploitation of fossil fuels contributes to the climate change. When burning, they are the largest emitters of carbon dioxide (CO_2), one of the major greenhouse gases (together with methane). Carbon dioxide contributes to global warming by absorbing invisible, infrared radiation (heat) coming from the Earth's surface and preventing its evacuation toward space. Fig. 1.2 (left panel) shows the evolution of the carbon dioxide concentration in the atmosphere since 1960 [1.2]. The CO_2 concentration increased nearly 100

ppm (30%) during the last 50 years, and continues to rise, mainly because of the intense exploitation of fossil fuels. Fig. 1.2 (right panel) shows temperature anomaly over the last 140 years [1.2]. The term *temperature anomaly* means a departure from a reference value or long-term average, and its value is averaged over the entire planet. Starting 1960 a drastic change in temperature anomaly evolution is clearly seen. Today, in average, the temperature of the planet atmosphere is 1 degree higher than in 1960. The environmental consequences of global warming caused by human activities are now widespread: more intense heat waves, accelerated rise of sea level, glaciers melting, species extinction, and many others [1.2].
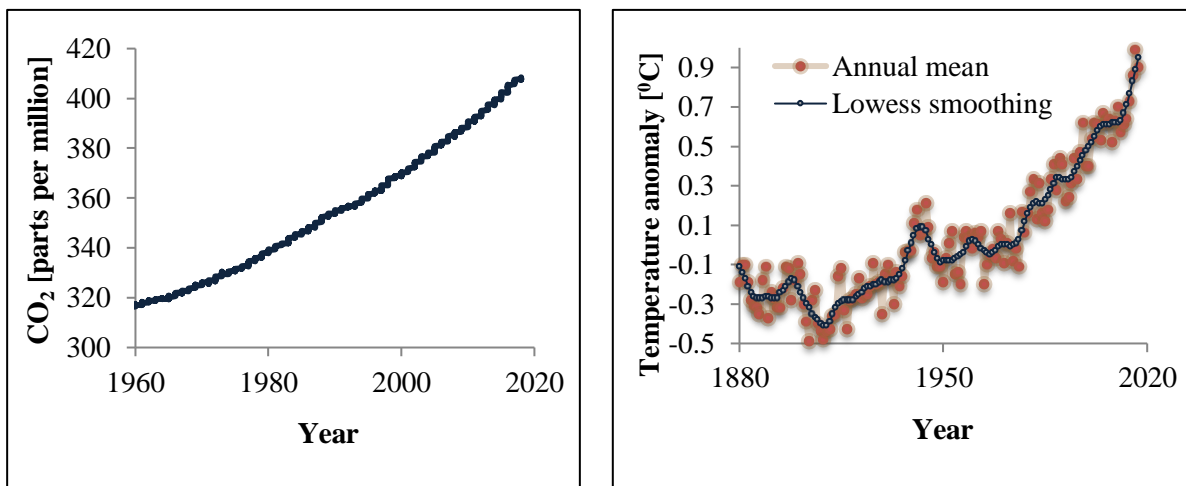
Figure 1.2. (left) Carbon dioxide concentration – monthly measurement (in ppm); (right) global land-ocean temperature index [1.2].

The environmental and human health issues caused by overconsumption of energy by modern societies, and the exploitation of fossil fuels at the level that overpassed the planet capacity to absorb its consequences forces humanity to look for alternative sources of energy. They should be environmentally sustainable and renewable. Many of such resources (fluxes or deposits) are now widely exploited: it includes solar and geothermal energy, energy of wind and water, and energy of biomass, a main energy resource for centuries, now rehabilitated. These so called 'green' energy resources are mainly used to produce electricity.

One of the most expanding sectors using fossil fuels is transportation. Vehicular transport and aviation are currently the main responsible for the fast growth of CO_2 emissions (~30% of total CO_2 emissions in the most developed countries) [1.3]. Therefore, transportation sector requires new technological advances in the field of engine performance, those operating using conventional fuels (gasoline or diesel) or natural gas and biofuels, and development of high capacity batteries for improvement of the range of electric vehicles. Another possibility

2

consists in using alternative energy vector, hydrogen: clean, renewable and non-toxic gas, that can supply fuel cells, but today is mainly used as a rocket fuel (together with oxygen) [1.4].

Hydrogen has higher energy content per unit mass than organic compounds made from fossil fuels. Fig. 1.3 compares the gravimetric and volumetric densities of energies of common fuels [1.5]. Gravimetric density of hydrogen (33 kWh/kg) is nearly three times higher than gasoline (12 kWh/kg). Additionally, the exothermal reaction of hydrogen with oxygen produces energy and water vapour only (combustion by-product). These two facts make hydrogen an ideal energy vector to be used in transportation. Unfortunately, the development of hydrogen-fuelled vehicles faces a major difficulty related to of on-board hydrogen storage. Hydrogen has low volumetric density of energy (2.5 kWh/L for liquid hydrogen), whereas that of gasoline is nearly 4 times larger (9.5 kWh/L). It means that 5–13 kg of hydrogen must be stored on-board to meet the convenient driving range of the light-duty vehicle of ~500 km [1.5].
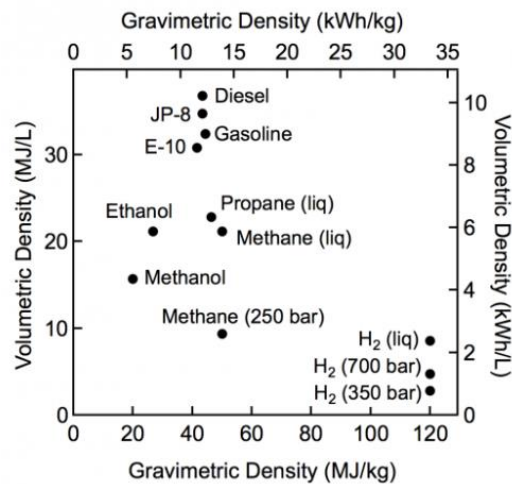
Figure 1.3. Comparison of specific energy (energy per mass or gravimetric density) and energy density (energy per volume or volumetric density) for several fuels based on lower heating values [1.5].

Hydrogen on-board storage systems have to meet cost, safety and size requirements. According to DOE requirements, storage system should allow to drive more than 500 km without refilling the tank. To reach this goal, storage system must provide 1.5 kWh/kg of gravimetric capacity and 1.0 kWh/L of volumetric capacity [1.5]. In the case of hydrogen, these numbers imply the development of hydrogen storage system allowing the gravimetric storage of 4.5 wt.% of hydrogen, with simultaneously volumetric capacity of 0.030 kg of hydrogen per litre of tank (Table 1). Such high-density storage of hydrogen is technologically challenging.

Theoretically, hydrogen can be stored either (i) physically, in form of gas (compressed at ambient temperature in high-pressure tanks), in form of liquid (at ambient pressure but cryogenic temperatures), or in form of gas confined inside a porous solids (reversibly physisorbed on pores walls through weak van der Waals forces), or (ii) chemically, in hydrogen-containing materials (hydrogen is then forming strong chemical bonds with other elements). Today compression is the most widely used method of hydrogen densification. The gas, compressed to the high pressure, is storaged in cylindrical bottles, containers or large volume underground caverns. This method is relatively inexpensive and allows for large scale stationary storage. It used in refuelling stations, as its additional advantage is fast filling-releasing rate. However, it is inconvenient for vehicular applications, as it is not safe for massive use. In fact, to guarantee the necessary gravimetric and volumetric gas density the pressure inside the fully loaded vehicle's tank should be very high. It is a consequence of the fact that the stored quantity does not scale proportionally with pressure. According to the review published by Zhang et al., at 350 bar the gravimetric and volumetric gas densities are 1.8 kWh/kg and 0,6 kWh/L, respectively; when the pressure increases to 700 bar the values are 1.5 kWh/kg and 0.8 kWh/L, only [1.6].

Table 1. Storage system targets; data presented by DOE [1.5]

Storage System Targets	Gravimetric Density kWh/kg system ($kg H_2$/kg system)	Volumetric Density kWh/L system ($kg H_2$/L system)	Cost $/kWh ($/$kg H_2$)
Ultimate	2.2 (0.065)	1.7 (0.050)	$10 ($333)
2020	1.5 (0.045)	1.0 (0.030)	$8 ($266)
Current Status (from Aragonne National Laboratory)	Gravimetric Density kWh/kg system ($kg H_2$/kg system)	Volumetric Density kWh/L system ($kg H_2$/L system)	Cost $/kWh ($/$kg H_2$)
700 bars compressed single tank	1.4 (0.042)	0.8 (0.024)	$15 ($500)

4

The small 700 bar hydrogen tanks are today the most successful in meeting most of the DOE 2020 requirements (see Table 1) [1.7]. The two already manufactured fuel cell cars, Toyota Mirai (released in 2015) and Hyundai Nexo (2018) have two or three 700 bar hydrogen tanks with total volume of ~156 L to provide around 400 km of drive. However, for safety reasons and costs, a massive production of such vehicles will not be possible in the near future.

The density of stored energy is higher when hydrogen is stored in the liquid form. However, this method of storage needs an initial expense of large amount of energy: first, to cool the gas down to 21 K, and then to liquefy it [1.8]. As the vessels containing liquid hydrogen are usually stored at ambient conditions, the heat input from outside the vessel causes hydrogen loss (5% of total hydrogen mass per hour) via evaporation (boil-off phenomenon). In the case of vehicular applications, the boil-off effect should be eliminated, not only to reduce the refuelling frequency and costs, but also to improve the energy efficiency and safety [1.6, 1.9]. Additionally, the big weight of the storage vessels of both gas and liquid hydrogen (the tanks are made mostly of metals and carbon fibers [1.10]) and their small capacity make the physical storage of liquid/gaseous hydrogen expensive and hard to implement on board of vehicles.

The nanotechnology appears to be an efficient strategy to address the challenges mentioned above. Physical storage can be facilitated by trapping hydrogen inside the high surface area nanostructured materials such as zeolites, carbon materials (i.e. graphene, nanotubes, fullerenes), Metal Organic Frameworks (MOFs), Covalent Organic Frameworks (COFs), or Porous Polymer Networks (PPN). The optimization of hydrogen sorbent has been summarized in many review articles [1.11-1.16]. According to current state of knowledge it will be difficult to reach the high H_2 storage in conventional high surface area adsorbents, because of their low average adsorption energy, heterogeneity of surfaces, macroporosity and poor volumetric packing. In carbon-based materials (with specific surfaces up to 3200 m^2/g) the main limitation results from the relatively small hydrogen binding to the graphene surface (4-6 kJ/mol) [1.11]. The porous MOFs and COFs structures with exceptionally large surface areas (up to 5500 m^2/g) have been also tested for hydrogen storage [1.17-1.19]. These materials are built from metal or metal oxide vertexes interconnected by organic linkers. In COFs, metal sites are replaced by light elements to decrease the structure weight. Depending on choice of the building elements a variety of 3D structures has been prepared, with very high and tunable porosity [1.20]. Many experimental and theoretical studies have shown impressive hydrogen storage capacity in COFs (in particular, COF-108 exceed 20 wt.% storage capacity at 100 bar [1.20]), but at cryogenic temperature and high pressure. However, the optimization of pore size

distribution in order to maximize sorbent specific surface is not easy to achieve with simultaneous maintain of necessary high volumetric density defined by DOE. The average binding energy of H_2 in MOFs and COFs is even lower than that of the activated carbons. In consequence, their performance at ambient temperature and moderated pressure still falls short from the DOE targets.

Chemical methods of hydrogen generation and storage are based on a reversibility of the hydrogenation/dehydrogenation reactions upon changes in temperature and pressure [1.21]. Unfortunately, in many cases, the hydrogenation reaction requires high operating temperatures from (80^0C to 600^0C) and must be done off-board (no on-board refuelling is possible) [1.22]. In addition, a platinum-based or noble-metal supported catalyst is required to enhance the kinetics of hydrogen cycling.

Although a large scientific effort is focused nowadays on the formation of hydrides, and storage in zeolites and metal organic frameworks, the modest progress of performance and relatively high cost of these methods lead to the search of alternative ways of hydrogen storage. The physisorption appears today as the best way of physical hydrogen storage. However, an optimal H_2 sorbent should be developed. The current trends focus on a search for materials with higher binding energy of hydrogen. Carbon-based adsorbents (activated carbon and carbon nanotubes) remain amongst the most promising materials for this purpose.

1.2. Literature review

To be successfully applied in mobile devices, the hydrogen adsorbent has to fulfil many requirements. It should not only store at room temperature 0.045 kg of H_2 per kilogram of system (thus 4.5 wt.%, the 2020 goal, see Table 1), but also 0.030 kg of H_2 per litre of system. The adsorbent has also to be chemically stable, of low weight, low cost, and has to allow reversible storage at room temperature. Finding the best adsorbents to reach these targets basically consists in optimizing two essential adsorption parameters: the energy of hydrogen binding to the material and the surface available for adsorption [1.11]. Too high adsorption energy will lead to a large amount of residual adsorptive at the exhaustion pressure, and therefore to reduced delivery, whereas too low hydrogen-sorbent interaction will result in low density of stored gas [1.12]. Therefore, the adsorption at ambient temperature must be almost entirely governed by the weak van der Waals (VdW) interactions (physisorption). Chemisorption requires too high desorption temperatures (> 600 K), impossible to implement in mobile devices [1.23].

1.2.1. Carbon materials

1.2.1.1. Graphene – a base for other forms of carbon

Pure carbon materials such as graphite, activated carbons, and carbon nanotubes (CNT) adsorb hydrogen with energy of 4-6 kJ/mol. These values are too low to efficiently store required amount of hydrogen at room temperature and reasonable (lower than 120 bar) pressures. Theoretical calculations predict storage capacities of graphene-based absorbents do not exceed 1 wt.% at 100 K and rapidly decrease at higher temperatures [1.24]. Maximal storage capacities at 77 K and ambient pressure are found to be about 1.90 and 2.25 wt.% for stacks of graphene sheets and isolated graphene sheets, respectively. Patchkovskii et al. [1.25] pointed out that the low attractive H_2-graphene reaction energy at ambient temperature makes graphite unsuitable for practical H_2 storage. However, if the distance between graphene layers that compose graphite increases (graphite is expanded), hydrogen may penetrate between layers and adsorb with much higher energy.

Graphene is a two-dimensional one-atom-thick crystal, composed of carbon atoms, sp^2 hybridized and arranged in honeycomb-like pattern. It is a promising adsorbent for many gases due to its high specific surface area, of the order of ~ 2600 m^2/g (Klechikov et.al., [1.26]). Hydrogen can be adsorbed on graphene either by physisorption (involving Van der Waals interactions) or by chemisorption, i.e. by forming a chemical bond with the carbon atoms [1.27]. At ambient temperature the energy of hydrogen physisorption on graphene is around 0.6 kJ/mol [1.25]. At high pressures and low temperatures hydrogen forms dense monolayer on of graphene, which corresponds to 3.3 wt. % of gravimetric storage capacity [1.28].

The chemisorption of atomic hydrogen on graphene occurs with the energy of 15 kJ/mol. It is not observed at ambient temperature because of the high energy required for the dissociation of the hydrogen molecule in two atoms. Atomic hydrogen chemically attached to the graphene layer creates graphane by changing carbon hybridization from sp^2 to sp^3. This structural modification induces several changes in electrical properties of the material: the conducting p-bands disappear, the energy gap appears between conduction and valence band [1.29, 1.30], and the material becomes a semiconductor. The modifications of electrical and structural properties of graphene upon hydrogenations have been observed using a variety of characterization tools. It was reported by Elias et al. [1.31], that electron diffraction patterns change after 4 hours of exposure of graphene membranes to atomic hydrogen. Raman spectra also change when hydrogenation takes place. In general, the intentional formation of defects and/or imperfections in sp^2 structure of graphite/graphene is considered to be a promising

approach to improve the capacity of carbon-based materials to store hydrogen. There are several types of structural defects that can be generated in graphene. The first category consists in the presence of non-hexagonal rings (pentagons or heptagons) in the graphene layer. These defects induce curvature of the graphene-like layers. Another, related type of defects consists in bond rotations (called Stone-Wales–type transformations, Figure 1.4). These defects are created by rotating by 90^0 a carbon—carbon bond; as a result, four adjacent hexagons transform into two pentagons and two heptagons.

a)   b)
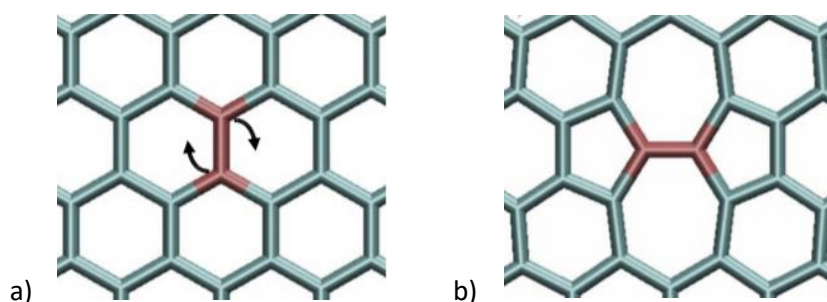
Figure 1.4. Stone-Wales defect. a) rotation of one carbon-carbon bond over 90°, b) the resulting defect, consisting in two pentagons adjacent to two heptagons [1.32].

The last category is non-sp^2 carbon defects. In this case, highly reactive carbon species are present in the form of dangling bonds, interstitial atoms, adatoms, or vacancies. All these defects can be doped/substituted by different atoms [1.33]. Graphene edges can be considered as defects, and they also fall in this category [1.34]. The graphene edges can occur in different atomic configurations (zig-zag, Klein edge, arm-chair, reconstructed 5–7 edge). All these structures have chemical and electronic properties that differ a lot from those of 'bulk' graphene [1.35, 1.36]. Theoretically, graphene edges are very easily passivated with hydrogen as this lowers the edge energy [1.36]. A variety of other elements (N, O, H, Fe and Si) are also known to chemically bond to the graphene edges. The edges of fragmented graphene sheets create additional surface for adsorption [1.37].

Graphene is a basic building block of other carbon allotropes, like buckyballs or carbon nanotubes (Fig. 1.5). In fact, the inclusion of 12 pentagons in a graphitic cluster leads to formation of fullerenes, all-carbon closed clusters with no boundaries. Such spherical surface is electronegative; therefore, the chemistry of fullerenes is very rich, and makes them become good candidates for hydrogen adsorption [1.38]. Similarly, the presence of heptagons and octagons could produce Schwarzite-like materials or nanotube networks with micropores

[1.33], where adsorption can take place. The adsorption properties of above-mentioned materials will be described in detail in the chapter 1.2.1.2.
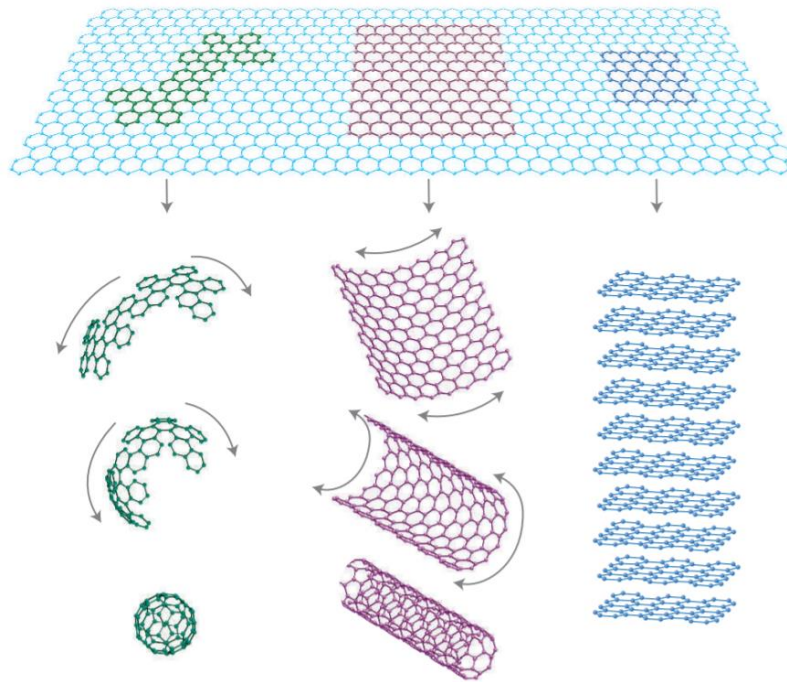
Figure 1.5. Graphene is a 2D building material for carbon materials of all other dimensionalities. It can be wrapped up into 0D buckyballs, rolled into 1D nanotubes or stacked into 3D graphite [1.39].

1.2.1.2. Carbon nanotubes, fullerenes, and nanocones

Carbon nanotubes (CNT) are organized cylindrical structures which can be synthetized by many techniques such as the arc-discharge [1.40], laser-ablation (vaporization) of graphite [1.41], or chemical vapour deposition (CVD) [1.42]. Their diameters range from subnanometer to tens of nanometers, and the length from less than a micron to several millimetres. CNTs are made up of a rolled graphite basal plane. Depending on the number of cylinders that constitute a CNT, we distinguish single-walled CNTs (SWCNTs), double-walled CNTs (DWCNTs), and multi-walled CNTs (MWCNTs), with a central tubule of nanometric diameter surrounded by several graphitic layers separated by about 0.36 nm [1.43]. The rolling up direction of graphene sheet (a chiral vector, Fig. 1.6), and in consequence, the angle between C-C bonds and the tube axis determine the chirality of a tube. The two extreme situations, "zigzag" (chiral angel $\theta = 0°$ and m = 0) and "armchair" ($\theta = 30°$ and n = m) CNTs are showed on Fig. 1.6.

Figure 1.6. a) Schematic diagram showing how a hexagonal sheet of graphite is 'rolled' to form a carbon nanotube; Illustrations of the atomic structure of (b) an armchair and (c) a zigzag nanotube [1.44].

The electronic properties of a nanotube depend on its structure. Armchair nanotubes are metallic, zigzag can be either metallic or semiconducting [1.43, 1.44]. The optical, mechanical and conductive properties of nanotubes where largely investigated [1.45-1.48]. Their microporous nature was also explored (theoretically and experimentally) to investigate 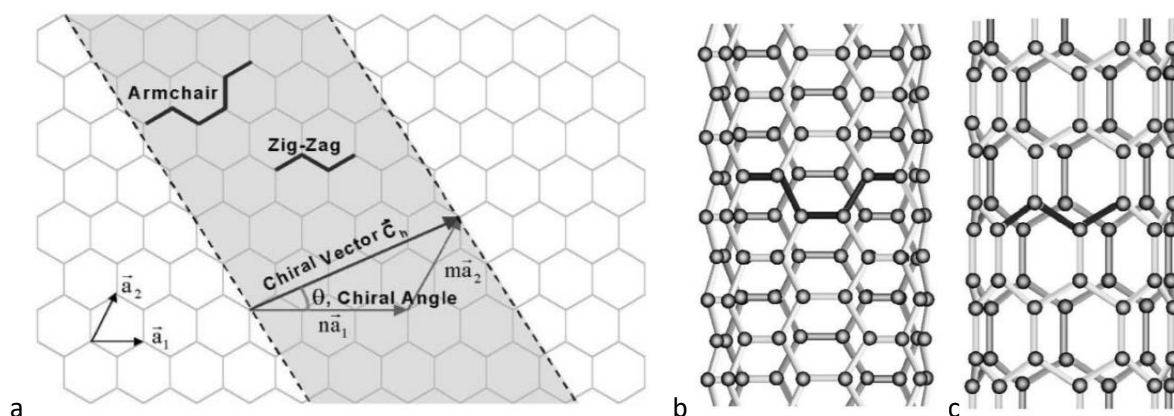the possibility of CNTs application as gas adsorption/separation material. Darkim et. al [1.49] reported the Monte Carlo simulations of hydrogen adsorption in SWCNT with diameter from 0.7 to 1.1 nm, at the pressure of 10 MPa, and temperature of 293 K. The authors showed that the number of adsorbed molecules decrease when the tube diameter increase. This result pointed out the importance of the solid–gas interaction for the total gas uptake and stressed that the space available for adsorption of hydrogen molecules has to be small enough to maximize the gas interaction with the confining walls. A year later Liu et al. [1.50] reported the synthesis of SWCNTs using semi-continuous hydrogen electric arc discharge technique. In contrary to the traditional electric arc method, they used a large, rotatable cylindrical anode (400 mm in diameter and 35 mm in height) composed of 94.5 atomic weight % of graphite, evenly dispersed catalysts powders (3 wt.% of Ni, 0.75 wt.% of Co, 0.75 wt.% of Fe), and growth promoter FeS (1 wt.%). The anode and cathode are not facing each other, but rather make an oblique angle. The produced carbon nanotubes have the diameter of ~1.85 nm and can store 4.2 wt.% of hydrogen at room temperature and pressure of 12 MPa. Moreover, the authors showed that higher hydrogen uptake can be reached in nanotubes with bigger diameter. This disagreement between the results obtained by both research groups can be tentatively attributed to the differences of SWCNTs diameters and/or different purity of the samples. Wang and Johnson [1.51] calculated the adsorption isotherms for optimized tube arrays as a function of the tubes'

diameters, the structure of the tube bundles, and the interaction potential between hydrogen and the tube walls. The tubes of 0.9 nm of diameter show the highest volumetric densities of adsorbed hydrogen comparing to the tubes with bigger diameters 1.2 and 1.8 nm, at both 298 and 77 K. At 298 K and the pressure of 100 bar the gravimetric and volumetric densities of the adsorbed hydrogen are 0.043 kg/L and 0.042 kg/kg, respectively. Williams and Eklund [1.52] performed Monte Carlo simulation of H_2 physisorption in finite-diameter carbon SWCNT ropes and found that at constant pressure the amount of adsorbed hydrogen increases with decreasing temperature: from 1.4 wt.% (T = 300 K) to 9.6 wt.% (T = 77 K), for the storage pressure of 10 MPa. For lower hydrogen pressure (p = 10 MPa) the stored amount is considerably lower, 0.2 wt.% (T = 300 K), and 5.9 wt.% (T = 77 K). Experimentally measured hydrogen uptake in SWCNTs (at ambient temperature and pressure) is of 1.5 wt.% per 1000 m^2/g of surface [1.28]. Although the results reported in the literature present many inconsistencies, all groups agree that SWCNTs are not the best material for hydrogen storage due to their low hydrogen uptake at ambient temperature.

Another allotrope of carbon, fullerenes, are the closed quasi-spherical structures isomeric of CNT. [1.53]. The deviation from planar geometry of graphene sheet causes the change of the hybridization of carbon from purely sp^2 (as in graphite) toward sp^3, with electron density strongly localized on selected carbon atoms [1.54, 1.55]. Theoretically, hydrogen may be adsorbed either in octahedral interstices of close-packed crystalline structures of fullerenes or inside the fullerene cage. Venkataramanan et. al [1.56] showed experimentally that the storage capacity of the C_{60} crystals is small, of only 0.28 wt.% at 40 ^{0}C. The mechanism of hydrogen adsorption inside the fullerene C_{60} cage was theoretically calculated by Pupysheva et al. [1.57]. The authors demonstrated that hydrogen has tendency to create chemical bonds with the nanoparticles with bent surface (such as nanotubes or fullerenes). These bonds are mainly formed on the convex surface of the nanoparticle as the carbon p-orbital participating in bond formation is localized outside the carbon cage. At high pressures hydrogen can also chemically attach to carbon atoms on concave surface of fullerene. It has been shown that the C_{60} molecule with 58 hydrogen atoms chemically attached to the internal fullerene surface becomes unstable at room temperature; this leads to the breaking of the fullerene nanocage (Fig. 1.7) and to the release of molecular hydrogen. Therefore, the storage of hydrogen in this system is reversible. However, to reach DOE goal, the hydrogenated fullerenes with larger cage should be considered. The fullerene C_{720}, encapsulating more than 800 hydrogen atoms could reversibly store ~ 10 wt. % of hydrogen at T = 300 K [1.57].
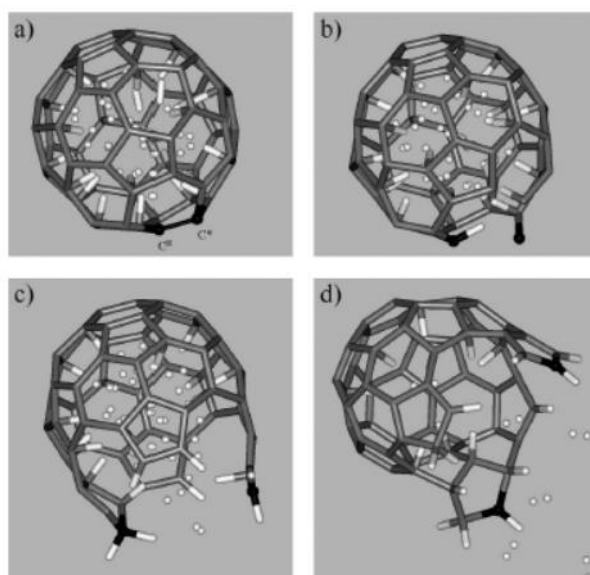
Figure 1.7. Snapshots of ab initio molecular dynamics simulations of H58@C60 structure at 300 K: (a) 0 fs, (b) 250 fs, (c) 350 fs, and (d) 800 fs. Breaking of bond between two carbon atoms shown in black initiates cage opening [1.57].

A large experimental and theoretical literature describes the possibilities of hydrogen storage in chemically modified fullerenes. This aspect will be referred in Chapter 1.2.2.

Carbon nanohorns for effective hydrogen storage have attracted less attention than fullerenes and nanotubes. They are subclass of the carbon nanocones (CNCs) and are usually synthetized by laser ablation of graphite. They are considered as model systems to investigate the nucleation and growth of curved carbon nanostructures. An example of a nanocone structure is shown on Fig. 1.8. As in all carbon allotropes, the presence of pentagons is essential in definition of atomic construction of a cone. A pentagon introduced into graphene honeycomb lattice constitutes a $60°$ disclination defect and, in consequence, the curvature of the flat graphene sheet (Charlier et, al [1.58]). The typical nanohorns nanoparticles have the specific surface areas around 1500 m^2/g. Due to their low cost and relatively high surface area they were considered as potential candidates for hydrogen storage. It was also reported that the energy of hydrogen binding to the nanohorn surface may be as high as 9.6-11.6 kJ/mol [1.59]. However, the nanohorns sample that exhibit simultaneously both: high surface required for hydrogen adsorption and high binding energy was not yet synthetized.

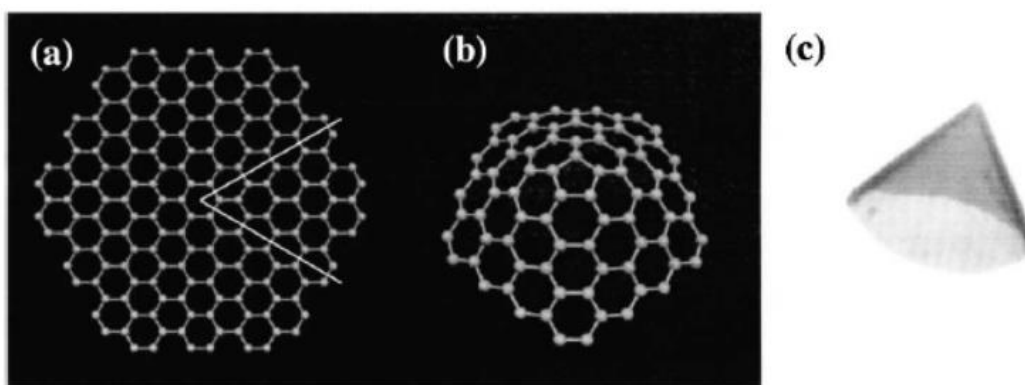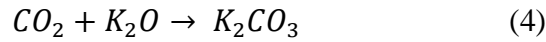**Figure 1.8.** (a) Extraction of a 60± section from a graphene sheet in order to form a cone structure (b) by incorporation of a single pentagon defect. (c) High-resolution transmission electron microscopy image of a nanocone which contains three pentagons at its tip apex [1.58, 1.60].

1.2.1.3. Activated carbons

Activated carbon are porous carbon materials with highly developed surface area and porosity. They can be prepared by any carbonization process from a variety of organic matter sources like pistachio-nut shells [1.61], corncob [1.62, 1.63], fire wood [1.64], Spanish anthracite [1.65], and any other organic waste. The materials are generally amorphous, and the distribution of pores sizes is usually wide. The activated carbons structures contain mostly micro (pore diameter smaller than 2 nm) and mesopores (pores of diameter between 2 and 50 nm). These pore sizes allow to accommodate a large variety of gases and liquids. The high surface area of activated carbons is obtained through an activation process. Physical activation consists in gasification of carbon precursor in the furnace under vacuum or controlled atmosphere; chemical activation is usually performed using acids or bases [1.62, 1.66].

Chemical activation is considered as the most efficient method of carbon activation. It can produce activated carbons with specific surface larger than 3000 m^2/g (the specific surface of an ideal, infinite graphene layer is equal 2600 m^2/g). It consists in mixing or impregnation of carbonized material with a chemical agent (KOH aqueous solution [1.62, 1.67], zinc chloride ($ZnCl_2$) or sulfuric acid (H_2SO_4), [1.61]), and then exposing the mixture to high temperature (above 700 °C) under gas flow (nitrogen, steam, helium, argon). Below T = 700 °C the activation with KOH proceeds in four steps [1.68]: (1) dehydration of KOH to K_2O, (2) carbon consumption, and ((3) and (4)) formation of carbonate.

$$2KOH \rightarrow K_2O + H_2O \qquad (1)$$
$$C + H_2O \rightarrow CO + H_2 \qquad (2)$$
$$CO + H_2O \rightarrow CO_2 + H_2 \qquad (3)$$
$$CO_2 + K_2O \rightarrow K_2CO_3 \qquad (4)$$
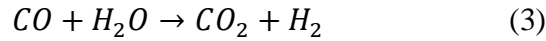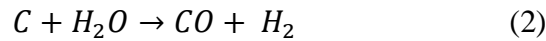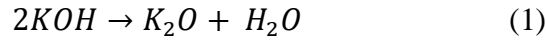
The process is generating micropores and small mesopores. The high temperature is necessary to maximize the yield and speed of the activation process, and to increase the fraction of micropores in the resulting product. Above 700 °C, activation occurs alongside the formation of metallic potassium. The mechanism is described by reaction (5) and (6): and it is related to formation of micropores:

$$K_2O + H_2 \rightarrow 2K + H_2O \qquad (5)$$
$$K_2O + C \rightarrow 2K + CO \qquad (6)$$
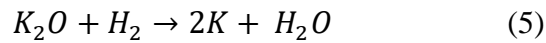
Metallic potassium penetrates between graphitic layers, pushing them away and create a path for KOH molecules (Fig. 1.9). This process generates mainly the micropores. The final porosity of activated carbon depends on activation temperature and KOH:C weight ratio used to prepare impregnated samples. According to Romanos et.al, [1.62], the maximum of both porosity and surface area of the material can be reached when KOH:C weigh ratio is around 3.5 and activation is performed at 900 °C.
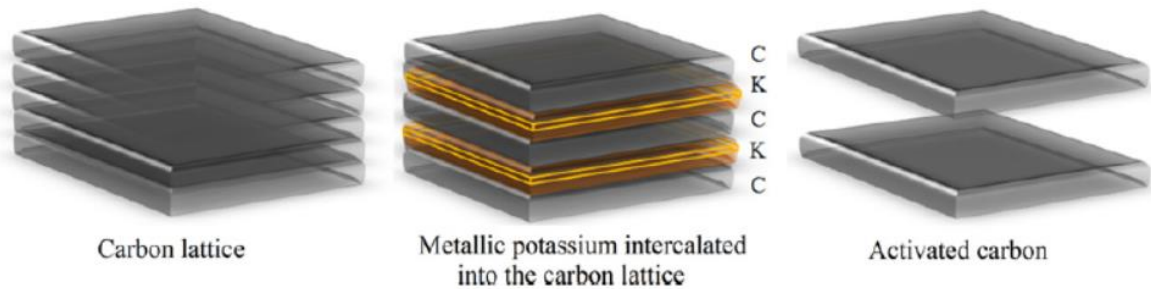
Figure 1.9. Activation mechanism above 700 °C by the penetration of metallic potassium into the lattice of the carbon, the expansion of the lattice by the intercalated potassium, and the rapid removal of the intercalate from the carbon matrix [1.62].

The possibility to use other hydroxides as activation agents was also analysed. Spanish anthracite was activated using both NaOH and KOH hydroxide [1.69]. In the case of activation with NaOH, physical mixture with weight ratio 3:1 (NaOH: precursor) was heated up to 760 °C under constant flow of N_2, CO_2 or mixtures of them. Depending on the gas flow used, a significant variation of the resulting porosity was observed. For sample annealed under nitrogen

flow of 500 ml/min (40 ml/min) the specific surfaces of 2193 m^2/g (1588 m^2/g) have been obtained. The activation was totally inefficient in CO_2 atmosphere. In fact, NaOH in contact with CO_2 transforms into Na_2CO_3 salt that is stable at 760 °C and remains attached to the carbon structure. On the contrary, the K_2CO_3 salt that forms during KOH activation at about 400 °C significantly decomposes into K_2O and volatile CO_2 in higher temperatures (~800 °C [1.67]) and the porosity of the resulting carbon material is high.

Porosity of closed nanostructures can be also increased by both chemical and thermal activation. Geng et al. [1.70] describe the mechanism of reversible opening/closing of oxidized SWCNTs (synthetized using laser ablation method, etched by sonication in H_2SO_4 and annealed in vacuum at 400 °C for 10h) depending on annealing conditions. The HRTEM images (Fig. 1.10) of the sample showed tubes that remained open after annealing. When these structures were subsequently annealed for 1 h at 800 °C, the SWNTs observed were closed and/or covered with some disordered structures. The opening of oxidized structures by thermal annealing was further confirmed by the comparison of ethane adsorption in the sample, before and after annealing at 800 °C (Fig. 1.10): the ethane uptake in open SWCNTs is three times higher than in topped tubes, because of the increase of the surface accessible for adsorption by that of tubes' interior.

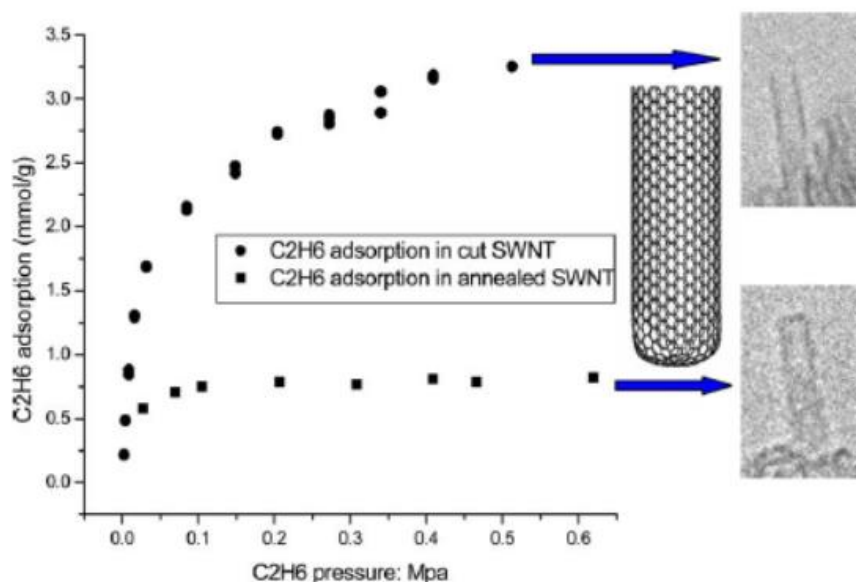**Figure 1.10.** Pressure dependence of the intensities of the broad peaks of the 1H NMR spectra of cut SWNTs before and after 800 ^{0}C annealing exposed to C_2H_6 at room temperature [1.70].

Chemical activation has some intrinsic advantages over physical activation: (i) it is usually carried out in a single step; (ii) it typically produces higher yields and very high specific surface areas; and (iii) it is possible to control the resultant microporosity and pore size distribution. On the other hand, it presents also many disadvantages: (i) the necessity of careful washing of the resulting material to remove by-products of the activation reactions, (ii) some of reaction product (salts or oxide) may remain chemically bonded to carbon structure, obstructing the pore entrance and affecting chemical properties of the activated carbon. Even though chemical activation has been successfully applied to the production of activated carbons for many years, the fundamental processes involved in the activation are still not completely understood, primarily due to the large number of variables involved in the process, including different activation agents and a large variety of organic precursors.

Although the activation procedures allow to prepare materials with large specific surface, the hydrogen uptake in activated carbons at ambient conditions is low. Webley and Sun [1.71] showed that corncobs derived carbons, activated with KOH and exhibiting specific surface larger than 2500 m^2/g, give the hydrogen uptake at 298–303 K ranging from 0.4–0.8 wt.% for hydrogen pressures between 20 and 120 bar. This result was confirmed by Pfeifer et. al. [1.72]. The activated carbons prepared from polystyrene (PSI)-based ion-exchangeable resins by KOH activation at 700 °C by Park et.al. [1.73] show the H_2 uptake of 0.81 wt.% (at 298 K and 100 bar). Chen et al. [1.74] reported that the activated polyaniline-based carbon tube with SSA ~ 2415 m^2/g and pore volume of ~ 1.55 cm^3/g can store 0.62 wt.% of H_2 at 293 K and 75 bars. The adsorption capacity hydrogen of activated carbons was suppressed when significant amounts acidic groups on the carbon surface was detected [1.75].

These results show that to achieve high storage of hydrogen by physisorption in carbon materials at ambient temperature, the energy of hydrogen binding to the carbon surface have to be increased. We describe the already explored possibilities of the surface modification aiming at the increase of the H_2-surface interaction in the following chapter.

1.2.2. Carbon structures decoration

Incorporating functional groups or dopants into carbon nanostructures changes materials' properties. In particular, it may increase the binding energy between hydrogen and carbon surface, thus enhance hydrogen sorption capacity. For that, a given surface modification

(doping or substitution) should induce electron deficit at the surface, increase the polarity of carbon surface resulting in improve molecular hydrogen interaction [1.76].

Structural modification of carbon nanostructures reported in the literature concern mainly the structures decorated with lightweight heteroatoms such as lithium (or other alkaline metals), fluorine and boron. According to the first principle calculations (Du et. al [1.77]), up to 12 hydrogen molecules can adsorb on each graphene fragment decorated with 4 Li atoms. The energy of hydrogen binding to the decorated surface was estimated to be ~24.3 kJ/mol (versus 4.5 kJ/mol for pure graphene), and to change proportionally to the Li concentration on the surface. The corresponding gravimetric storage capacity was close to 12 wt.%. This theoretical result stimulated many experimental works. Chen et al. [1.78] produced CNT by catalytic decomposition of CH_4, doped them by Li- or K-containing carbonates or nitrates (solid-state reactions), and show that the H_2 uptake in such CNTs can reach the value as high as 20 wt.% (for Li-doped CNT at 653 K), or 14 wt.% (for K-doped CNT, at room temperature). These values correspond to respectively $\sim$160 kg/L and 112 kg of H_2/L of volumetric storage and suggest that alkali metal-doped carbon nanotubes can operate as hydrogen sorbents at ambient temperature and moderate pressure. Wang et. al [1.79] doped multi-wall CNTs with lithium in solution, using a tetrahydrofuran (THF) solvated naphthalene anion radical salt ($Li^+C_{10}H_8^-$)as a dopant. The mixture was stirred for several days to allow thorough penetration of Li ions into the CNT network; then THF was allowed to evaporate at room temperature. Sample with 1.2 wt.% Li content showed a reversible hydrogen storage capacity of 3.9 wt.%. However, when the Li content was increased, hydrogen storage capacity gradually decreased. The authors concluded that the excessive carbon surface decoration with Li may lead to a decrease of the charge isolation, a decrease of specific surface area, a decrease of pore volume, and, in consequence, reduces hydrogen storage capacity. In fact, many authors [1.79, 1.80, 1.81], underline that ions have tendency to agglomerate or form complexes with other atoms, and the access of hydrogen molecules to them is limited; it causes the observed decrease the adsorbed hydrogen amount.

Modification of carbon materials by lightweight heteroatoms is an experimental challenge due to their poor dispersion in carbon materials. Thus, transition metal decoration has been suggested as an available way to increase the reversible hydrogen storage at room temperature by spillover [1.80]. Schematic representation of hydrogen spillover on Pd-decorated surface is shown on Fig. 1.11. Close to Pd nanoparticle (acting as catalyst) the hydrogen molecule undergoes dissociative chemisorption. The resulting hydrogen atoms

migrate on the Pd surface towards graphene, and subsequently diffuse on carbon surface away from the metal site. The detailed description of the process may be found in theoretical and experimental works of Parambhath et al. [1.82].
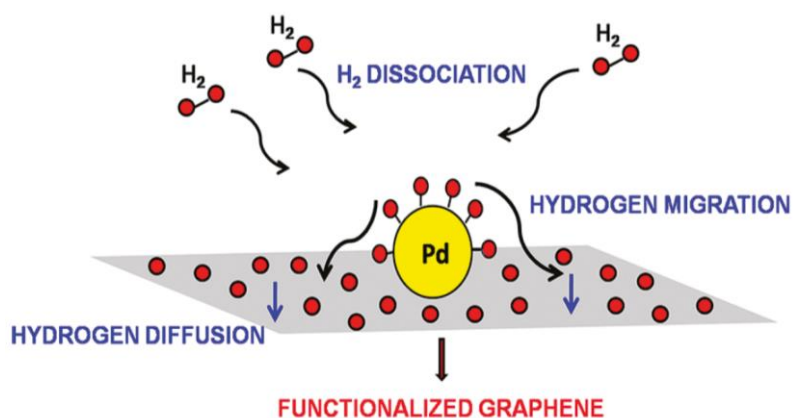
Figure 1.11. Schematic diagram of the spillover mechanism in Pd/graphene [1.82].

To obtain a uniform distribution of palladium atoms on graphene surface, the authors used a modified polyol method. The graphene fragments were dispersed in the solution of ethyl glycol (reducing, stabilizing and dispersing agent) with water. After 12 h of stirring, 1% aqueous solution of $PdCl_2$ was added by droplets, and the preparation has been stirred for another 24 h. Solution was adjusted to pH = 11 by adding NaOH 2.5 M and filtered. According to X-Ray diffractograms of the material, the obtained Pd particles were nanostructured (of the size of ~6.6 nm) and occupied ~20 wt.% of the sample surface. Unfortunately, the measured isosteric heat of adsorption was only of 7 kJ /mol, and hydrogen uptake at 25 ^{0}C and hydrogen pressure of 2 MPa did not exceeded 1.75 wt. % (0.5 wt.% for graphene).

To improve hydrogen adsorption in MWCNT at ambient pressure and temperature, functionalization with other metals (including Ca, Co, Fe, Ni, and Pd) was carried out by Reyhani et al. [1.83]. MWCNT were synthetized by chemical vapour deposition using Fe/Ni/MgO catalyst. Chemical modifications were carried out using Ca, Co, Fe, Ni, and Pd nitrates dissolved in water. The mixture was stirred for 1 h, then, the ion-adsorbed MWCNTs were filtered out from the metal salt solutions and annealed at 200 $^{\circ}$C for 24 h. The resulting material contained MWCNTs with particular forms of defects, containing oxygen functional groups. The authors suggested that these defects are necessary to prevents clustering of metals atoms. Hydrogen storage capacity of both: purified and metal-doped MWCNTs was then

evaluated at ambient temperature by volumetric method; it remains low for all samples, except for Pd-doped MWCNTs. The hydrogen storage capacity of the metal-MWCNTs were determined to be 0.3 wt.% (pure MWCNTs), 1.05 wt.% (Ca-MWCNTs), 1.5 wt.% (Co-MWCNTs), 0.75 wt.% (Fe- MWCNTs), 0.4 wt.% (Ni-MWCNTs), and 7 wt.% (Pd-MWCNTs) respectively. The significant difference between gravimetric storage capacity of Pd-MWCNTs and other doped MWCNTs is a consequence of chemisorption (via spillover) of H_2 on Pd-doped tubes. The difference between storage capacity of Pd–doped tubes prepared by Reyani et.al. [1.83] and those obtained by Parambhaths' group [1.82] was attributed to structural differences and uniformity of Pd distribution on the surfaces of both materials. Furthermore, adsorption of hydrogen on transition metals may also involve Kubas-type interactions. Kubas interaction is a 'non-classical' form of binding where molecular hydrogen creates *sigma complex,* wherein a σ-bonding electron pair (H:H) binds a ligand to a metal [1.84]. The detailed description of hydrogen adsorption via Kubas interaction can be found in [1.83 - 1.85]. Here we retain only that a single metal atom can bind multiple H_2 molecules via the Kubas interaction.

Carbon functionalization with other metals (Sc, V and Ti) were also studied. Sun et al. [1.86] analysed clustering of Ti on a C_{60} surface and its effect on hydrogen storage. Four specific sites of Ti distribution on the fullerene surface were considered: (i) the hexagonal sites (on top of any of the 20 hexagons), (ii) the pentagonal sites (on top of any of the 12 pentagons), and the bridge sites corresponding to (iii) any of the 30 carbon double bonds or (iv) any of the 60 single bonds. It was found that the preferred location for Ti atoms is the hexagonal site, with a binding energy of 2.35 eV. If Ti atoms are uniformly distributed on the fullerene' surface, hydrogen molecules may dissociate on the each Ti atom and the gravimetric storage capacity of 7.5 wt.% can be reached. However, as the structures containing Ti clusters are more stable, in practice the Ti-decorated C_{60} material can adsorb no more than 2.85 wt.% of hydrogen.

Decoration of carbon structures with alkali or transition metals have many shortcuts from the point of view of potential applications. First, clustering of metal atoms, very common for both light and transition group of metals, leads to low storage. The light alkali metals are known to be flammable and it is too dangerous to use them massively in the hydrogen storage systems, especially when they are in direct contact with gaseous oxygen. Transition metals (like platinum or palladium) are heavy and expensive, what makes them unsuitable as adsorbent components that should be commercialized at the large scale at moderated cost. Moreover, the chemisorption of atomic hydrogen initiated by the spillover of hydrogen molecules on metal particles is hardly reversible.

1.2.3. Hybrid carbon nanostructures

Nowadays, computer simulations can significantly accelerate the process of development of new materials, by rapid screening for desired properties of potential new structures, before they are physically prepared in the material research laboratories. Over the past few years, a considerable numerical effort allowed first to conceive, then to fabricate hybrid carbon materials for different optical, electronic or storage applications.

Most of the numerical projects focused on the possibility of introduction of molecular separators between graphene sheets to increase the interlayer distance and the volume accessible for adsorption. Dimitrakakis et al. [1.87] proposed an all carbon 3-D nanostructure consisting in parallel graphene layers located at a variable distance and stabilized by CNTs pillars, perpendicular to the graphene planes (Fig. 1.12a). Unfortunately, Grand Canonical Monte Carlo (GCMC) simulations of hydrogen adsorption in such structure gave the gravimetric and volumetric hydrogen uptakes very similar (and low) to those of simple CNTs or graphene materials: 1.5 wt.% and 6 g/L respectively (at 300K and 100 bar of hydrogen pressure). The storage capacity was improved when the structure was decorated with lithium cations (Fig. 1.12b). Li ions were placed above the centres of the carbon rings next to CNT. In such material the average hydrogen binding energy per H_2 per ring increased to be around 3.5 kcal/mol (14.6 kJ/mol). The gravimetric adsorption was enhanced by 76% at ambient, and by 88% at cryogenic temperature (T = 77K). Additionally, the volumetric adsorption also increased, by 30% and 38%, respectively.

A very similar structure was proposed by Wu et al. [1.88]; it is called periodic graphene nanobuds (PGNBs). The material consists in graphene monolayers separated by C_{60} fullerenes covalently attached to graphene via the cycloaddition reaction (Fig. 1.13). The structure is periodic, with the interlayer distance of 12.5 Å. The structure is stabilized by the same van der Waals interactions as in graphite. The estimated surface area of this porous network is ~2346 m^2/g, (close to that of graphene sheet), which makes the structure potentially suitable for hydrogen storage. Similar structures of sandwiched graphene-fullerene composites were studied by Ozturk et al. [1.89]. When doped by lithium, they may theoretically store up to 5 wt. % of hydrogen at 77 K and 1 bar.
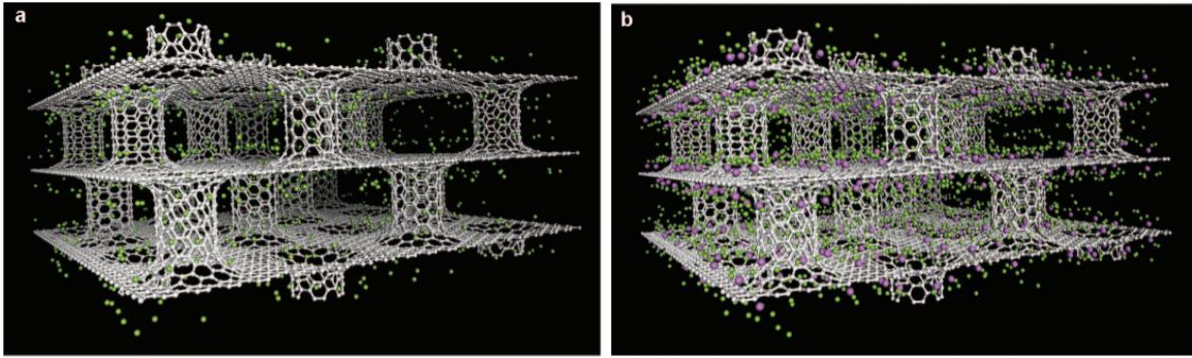
Figure 1.12. Simulation snapshots of (a) 3-D network nanostructure and (b) 3-D network lithium doped nanostructure; Hydrogen molecules are represented in green while lithium atoms are in purple. [1.87].
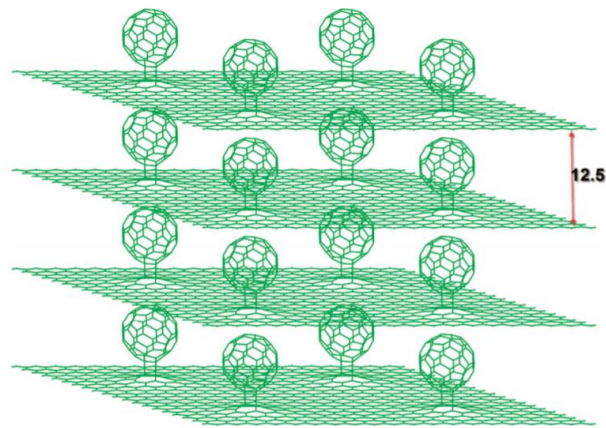
Figure 1.13. Periodic graphene nanobuds (PGNBs) model [1.88].

It has been shown experimentally that fullerenes or endohedral metalofullerenes such as $Gd@C_{82}$ (Gd encapsulated inside C_{82}, GdMF) can be inserted into single-wall nanotubes (SWNTs), and form carbon nanopeapod structures [1.90 - 1.92]. Fig. 1.14 shows HRTEM image of such structures. C_{60} are maintained separated from each other and from walls of nanotube by Van der Waals forces. It has been suggested that such structures may be applied in one-dimensional electronic devices or quantum computers. The analysis of influence of Gd and other metals encapsulated in fullerenes on the binding hydrogen on the nanotube surface has not been performed yet.
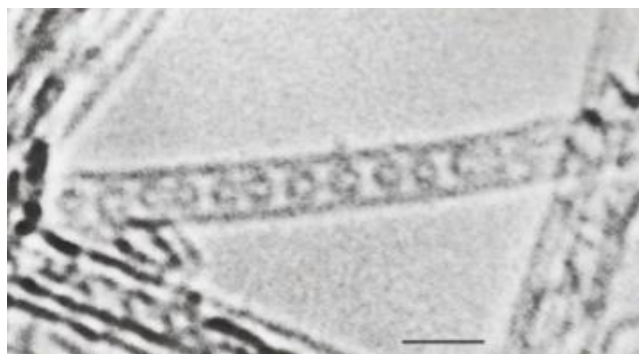
Figure 1.14. A single-walled carbon nanotube containing a row of closed carbon shells concentric with the tubule axis. The diameter and centre-to-centre spacing of the internal shells are consistent with a chain of C_{60} molecules. The nanotube is surrounded by a vacuum. Scale bar, 2.0 nanometres [1.90].

1.2.4. Conclusion

The existing pure carbon materials show relatively low energy of hydrogen binding to their surfaces, of the order of 4–6 kJ/mol. Higher binding energy can be obtained in nanoporous carbons, when the cumulative effect of interaction with confining walls is observed, or by adequate doping of carbon network by alkali or transition metals. However, these structures usually show low specific surface area and small microporous volume. This leads to small storage capacities of such materials, far from the applications' requirements. Simultaneous increase of material specific surface and micropore volume is a key issue for enhancing H_2 storage capacity. Although each of the parameters can be optimized separately, until now an efficient hydrogen adsorbent that could be produced at the large scale and efficiently operate at ambient temperature and moderate pressure has been not synthetized. The question "*Is it possible to theoretically predict and experimentally synthetize carbon based nanoporous structure that would fulfil the applicative requirements defined by US DOE?*" remains open.

1.2.5. Hydrogen storage in nanoporous carbons: is it possible?

Despite more than 20 years of research, no material yet possesses the adsorbing properties required for adequate hydrogen storage. All potential porous structures that were considered as hydrogen sorbents are far from optimal in any perspective for mobile applications. It is well established today that it will be difficult to reach the high H_2 storage in conventional high surface area adsorbents, because of their low average adsorption energy, heterogeneity of surfaces, poor volumetric packing or structural instability.

In the category of carbon-based sorbents of H_2, substitution with boron has been promoted as the most promising. Early theoretical calculations suggested a non-dissociative adsorption of H_2 on B and Be-doped fullerenes. The coupling between an empty, localized p_z orbital of the dopant and the H_2 orbital was shown to be essential for the enhanced H_2-sorbent interaction. According to Zhao et. Al [1.54], B-doping increases H_2 binding energy to 15-35 kJ/mol, making B-doped carbon an outstanding candidate for high capacity H_2 storage. Grand Canonical Monte Carlo simulations based on ab initio interaction model report an enhanced H_2 uptake in graphene slit pores with walls containing boron atoms [1.93,1.94]. The high capacity is not related to any particular crystallographic structure but depends only on B:C substitution ratio; 10 % substitution is necessary to rise the average binding energy to 10 kJ/mol, and to approach both gravimetric and volumetric directives of DOE for 2020 (Fig. 1.15). Further increase of this limit could be achieved with a higher substitution ratio or in structures showing higher specific surfaces.
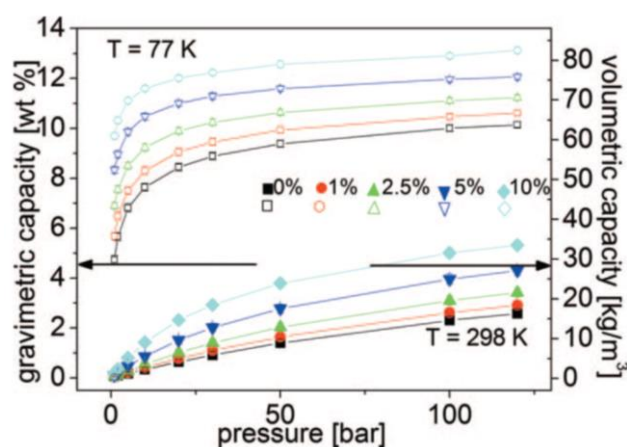
Figure 1.15. Gravimetric (left axis) and volumetric (right axis) adsorption of H_2 in B-substituted graphene slit pores of width d = 1.2 nm and the surface of 2600 m^2/g, as a function of pressure and the B:C substitution ratio, for T = 77 K and 298 K. For B:C = 10%, the system reaches the 2020 targets [1.94].

Obviously, experimental confirmation of the calculations is needed for validation of theoretical analysis. For that, substituted porous carbons have to be synthesized. First boron-carbon structures (BC_n) were already synthesized almost 30 years ago by the chemical reaction of benzene and boron trichloride at 800 °C [1.95]. However, the reaction product was s not porous. On the other hand, solid-solution techniques to prepare BC_n compounds require heat treatment at temperatures close to carbon graphitization and lead to a relatively low substitution

ratio [1.96-1.98]. For example, B-substituted graphene has been prepared by annealing highly oriented pyrolitic graphite (HOPG) in the presence of boron carbide BC_4 at T~2500 °C [1.99]. A carbonization of B-containing polymeric precursors has been also developed. The synthetized materials show high boron content (7.2 %) and enhanced binding energy (~11 kJ/mol), twice as much as the pure carbon; however, material specific area is relatively small (780 m^2/g). The chemical vapor deposition (CVD) is being frequently used, as it operates at lower temperatures (700-900 °C) and leads to higher boron uptake [1.100, 1.101]. Usually, C_6H_6 or C_2H_2 and BCl_3 are used as BC_n precursors. Due to interlayer intercalation of boron precursor at high boron concentrations, this method leads to non-porous thin films of poor crystallinity.

Another way to produce substituted nanoporous carbons consists in building them around appropriate templates using CVD [1.102]. Two procedures have been described in the literature: carbonization of hydroborane formed during the polymerization of divinyl benzene and BH_3 in alumina matrix [1.103] and carbonization of acetylene in the presence of borane gas in NaY zeolite [1.104]. The presence of B-C bonds was confirmed by ^{11}B MAS solid state NMR; however, B-content and effective sample porosities have been not determined.

Recently, it has been demonstrated that arc discharge between graphite electrodes, a technique used to prepare macroscopic quantities of fullerenes and carbon nanotubes, can be also optimized to synthesize graphene fragments composed of two to three layers [1.105]. The method makes use of the fact that in the presence of hydrogen in the discharge apparatus graphene sheets do not roll to form cage-like structures [1.105]. Boron-contained electrodes or B_2H_6-containing discharge atmosphere has been used to prepare boron-doped graphene fragments of the lateral size of 20 to 60 nm. The presence of substitutional boron in the sp^2 carbon structure has been confirmed by using electron energy loss spectroscopy (EELS), atomic force microscope (AFM) and Raman characterization methods. Similarly, nitrogen atoms have been successfully introduced to graphene sheets by arc discharge in the presence of pyridine or ammonia [1.106]. Although the resulting substitution ratio was not high (up to 3% for boron substitution and 1.4% for nitrogen), these preliminary results are promising as the arc discharge procedure could be easily optimized. The additional advantage of arc discharge technique is its ability to produce graphene fragments of nanometric size.

Fragmentation of the infinite pore walls into small patches creates an additional adsorption surface, at the patches' edges and can substantially increases hydrogen gravimetric storage capacity, by a factor of two [1.37]. The contribution of adsorption on the fragment edges

to the total amount stored is independent on the fragment shape and increases when the fragment lateral size decreases. However, simultaneously, the energy of adsorption at the edges rapidly decreases with the fragment size. Therefore, the final hydrogen uptake in pores of final lateral dimensions will result from a competition between two factors: larger adsorption surface introduced by the pore edges and lower average adsorption energy and heterogeneity (structural and energetic) of the system.

According to the mentioned results, it can be suggested that nanoporous carbons built up from interconnected fragments of graphene can show high hydrogen storage, if the fragment size and system topology can be optimized. Nanoporous carbons for hydrogen storage should: (i) have open geometry with considerable contribution of edge surface of the building units (fragments of graphene sheets); (ii) size of fragments wisely optimized; not too small because it leads to low energy of adsorption and decreasing uptake, and not too large to still take the advantage of an important contribution from the fragments edges; (iii) the density of the structures cannot be too low because of the volumetric storage capacity requirements.

The work presented in the following chapters constitutes a new contribution to the research of such material. The main goal of the project is to synthetize a new class of carbon-based, porous, high surface structures, which could extend the current limits of hydrogen storage by physisorption at room temperature. The ultimate goal is to reach hydrogen storage capacity approaching DOE targets and allowing practical application of the material as hydrogen adsorbent in the transportation sector.

1.3. Bibliography

[1.1] http://www.rmi.org; published by Chelsea Green in *Reinventing fire*, 2011; last access: 03/08/2018

[1.2] https://climate.nasa.gov/vital-signs/global-temperature/; global climate change official website of NASA; last access: 03/08/2018

[1.3] https://www.planete-energies.com; an initiative by Total S.A.; last access: 08/08/2018

[1.4] N. N. Smirnov, V. B. Betelin, R. M. Shagaliev, V. F. Nikitin, I. M. Belyakov, Y. N. Deryuguin, S. V. Aksenov, D. A. Korchazhkin, *Hydrogen fuel rocket engines simulation using LOGOS code*, International Journal of Hydrogen Energy XXX (2014) 1-9

[1.5] https://www.energy.gov; last access: 08/08/2018

[1.6] F. Zhang, P. Zhao, M. Niu, J. Maddy, *The survey of key technologies in hydrogen energy storage*, Internations Journal of Hydrogen Energy 41 (2016) 14535-14552

[1.7] S. Niaz, T. Manzoor, A. H. Panadith, *Hydrogen storage: Materials, methods and perspectives*, Renewable and Sustainable Energy Reviews 50 (2015) 457-469

[1.8] L. Zhou, *Progress and problems in hydrogen storage*, Renewable and Sustainable Energy Reviews 9 (2005) 395–408

[1.9] M. Hirscher, *Handbook of hydrogen storage: new materials for future energy storage*, 2010 WILEY-VCH Verlag GmbH & Co. KGaA, Wienheim, ISBN: 978-3-527-32273-2

[1.10] D. Mori, K. Hirose, *Recent challenges of hydrogen storage technologies for fuel cell vehicles*, Vol. 34, Issue 10, 2009, 4569-4574

[1.11] P. Bénard, R. Chahine, *Storage of hydrogen by physisorption on carbon and nanostructured materials*, Scripta Materialia 56 (2007) 803–808

[1.12] S. K. Bhatia, A. L. Myers, *Optimum conditions for adsorptive storage*, Langmuir 2006, 22, 1688-1700

[1.13] P. Benard, R. Chahine, *Modeling of adsorption storage of hydrogen on activated* carbons, Int. J. Hydrogen Energy 26 (2001) 849–855

[1.14] B. Panella, M. Hirscher, S. Roth, *Hydrogen adsorption in different carbon nanostruct*ures, Carbon 43 (2005) 2209–2214

[1.15] H. K. Chae, D. Y. Siberio-Perez, J. Kim, Y. B. Go, M. Eddaoudi, A. J. Matzger, M. O'Keeffe, O. M. Yaghi, *A route to high surface area, porosity and inclusion of large molecules in crystals*, Nature 427 (2004) 523–527

[1.16] G. E. Froudakis, *Hydrogen storage in nanotubes & nanostructures*, Mat.Today 14 (2011) 324-328

[1.17] U. Stoeck, S. Krause, V. Bon, I. Senkovska, S. Kaskel, *A highly porous metal-organic framework, constructed from a cuboctahedral super-molecular building block, with exceptionally high methane uptake*, ChemComm, The Royal Society of Chemistry 2012

[1.18] N. L. Rosi, J. Eckert, M. Eddaoudi, D. T. Vodak, J. Kim, M. O'Keefee and O. M. Yaghi, *Hydrogen storage in microporous metal–organic frameworks*, Science 300 (2003) 1127–1129

[1.19] J. L. C. Rowsell and O. M. Yaghi, *Strategies for hydrogen storage in metal–organic frameworks*, Angew. Chem., Int. Ed.44, (2005) 4670– 4679

[1.20] H. M. El-Kaderi, J. R. Hunt, J. L. Mendoza-Cortes, A. P. Cote, R. E. Taylor, M. O'Keeffe and O. M. Yaghi, *Designed synthesis of 3D covalent organic frameworks*, Science 316 (2007) 268–272

[1.21] B. Sakintuna, F. Lamari-Darkrim, M. Hirscher, International Journal of Hydrogen Energy 32 (2007) 1121-1140

[1.22] L. Schlapbach, A. Züttel, *Hydrogen-storage materials for mobile applications*, Nature, Vol. 414, 265-270, 2001

[1.23] J. Li, T. Furuta, H. Goto, T. Ohashi, Y. Fujiwara, *Theoretical evaluation of hydrogen storage capacity in pure carbon nanostructures*, J. Chem. Phys., Vol. 119, No. 4, 2003

[1.24] A. Touzik, H. Hermann, *Theoretical study of hydrogen adsorption on graphitic materials*, Chemical Physics Letters 416 (2005) 137–141

[1.25] S. Patchkovskii, J. S. Tse, S. N. Yurchenko, L. Zhechkov, T. Heine, G. Seifert, Graphene nanostructures as tunable storage media for molecular hydrogen, *PNAS*, **102**, 10439 (2005)

[1.26] A. G. Klechikov, G. Mercier, P. Merino, S. Blanco, C. Merino, A. V. Talyzin, Hydrogen storage in bulk graphene-related materials, Microporous and Mesoporous Materials 210 (2015) 46-51

[1.27] V. Tozzini, V. Pellegrini, *Prospects for hydrogen storage in graphene*, Phys. Chem. Chem. Phys. 2013, 15, 80-89

[1.28] A. Züttel, P. Sudana, Ph. Maurona, T. Kiyobayashib, Ch. Emmeneggera, L. Schlapbacha, *Hydrogen storage in carbon nanostructures*, International Journal of Hydrogen Energy 27 (2002) 203–212

[1.29] J. O. Sofo, A. S. Chaudhari, G. D. Barber, *Graphane: A two-dimensional hydrocarbon,* Phys. Rev. B 75, 153401 (2007)

[1.30] D. W. Boukhvalov, M. I. Katsnelson, A. I. Lichtenstein, Phys. Rev. B 77, 035427 (2008)

[1.31] D. C. Elias, R. R. Nair, T. M. G. Mohiuddin, S. V. Morozov, P. Blake, M. P. Halsall, A. C. Ferrari, D. W. Boukhvalov, M. I. Katsnelson, A. K. Geim, K. S. Novoselov, *Control of Graphene's Properties by Reversible Hydrogenation: Evidence for Graphane*, Science, Vol 323, 2009, 610-613

[1.32] J. Ma, D. Alfè, A. Michaelides, E. Wang, *Stone-Wales defects in graphene and other sp^2-bonded materials*, Phys. Rev. B, 80, 033407 (2009)

[1.33] M. Terrones, A. R. Botello-Méndez, J. Campos-Delgadoc, F. López-Urías, Y. I. Vega-Cantúd, F. J. Rodríguez-Macías, A. L. Elías, E. Munoz-Sandoval, A. G. Cano-Márquez, J.-C. Charlier, H. Terrones, *Graphene and graphite nanoribbons: Morphology, properties, synthesis, defects and applications*, Nano Today (2010) 5, 351—372

[1.34] P. S. Branicio, M. H. Jhon, C. K. Gan, D. J. Srolovitz, *Properties on the edge: graphene edge energies, edge stresses, edge warping, and the Wulff shape of graphene flakes*, Modelling Simul. Mater. Sci. Eng. 19 (2011) 054002

[1.35] Ç. Ö. Girit, J. C. Meyer, R. Erni, M. D. Rossell, C. Kisielowski, L. Yang, C.-H. Park, M. F. Crommie, M. L. Cohen, S. G. Louie, A. Zettl, *Graphene at the edge: stability and dynamics*, Science 323, 1705 -1708 (2009)

[1.36] K. He, G.-D. Lee, A. W. Robertson, E. Yoon, J. H. Warner, *Hydrogen-free graphene edges*, Nature Comm. Jan 2014

[1.37] L. Firlej, B. Kuchta, A. Lazarewicz and P. Pfeifer, *Increased H2 gravimetric storage capacity in truncated carbon slit pores modelled by Grand Canonical Monte Carlo*, Carbon 53 (2013) 208-215

[1.38] A. Hirsch, M. Brettreich, *Fullerenes*, Wiley-VCH, 2005

[1.39] A. K. Geim, K. S. Novoselov, *The rise of graphene*, Nature Materials, Vol. 6, 2007, 183-191

[1.40] S. Iijima, *Helical microtubules of graphitic carbon*, Nature 1991, 354, 56–58

[1.41] H. Dai, A. G. Rinzler, P. Nikolaev, A. Thess, D. T. Colbert, R. E. Smalley, *Single-wall nanotubes produced by metal-catalysed disproportionation of carbon monoxide*, Chem. Phys. Lett. 1996, 260, 471–475

[1.42] J. *Yacaman*, M. Miki-Yoshida, L. Rendon, and *J. G.* Santiesteban, *Catalytic growth of carbon microtubules with fullerene structure*, *Appl Phys. Lett. 62*, (*1993*), *202-204*

[1.43] E. Katz, I. Willner, *Biomolecule-functionalized carbon nanotubes: applications in nanobioelectronics*, Chem. Phys. Chem. 2004, 5, 1084-1104

[1.44] E. T. Thostensona, Z. Renb, T.-W. Chou, *Advances in the science and technology of carbon nanotubes and their composites: a review*, Composites Science and Technology 61 (2001) 1899–1912

[1.45] A. M. K. Esawi, K. Morsi, A. Sayed, M. Taher, S. Lanka, Effect of carbon nanotube (CNT) content on the mechanical properties of CNT-reinforced aluminium composites, Composites Science and Technology 70 (2010) 2237–2241

[1.46] A. Allaouia, S. Baia, H.M. Cheng, J.B. Bai, *Mechanical and electrical properties of a MWNT/epoxy composite*, Composites Science and Technology 62 (2002) 1993–1998

[1.47] H. Dai, E. W. Wong, C. M. Lieber, *Probing Electrical Transport in Nanomaterials: Conductivity of Individual Carbon Nanotubes*, Science Vol. 272, 1996, 523-526

[1.48] T. W. Ebbesen, H. J. Lezec, H. Hiura, J. W. Bennett, H. F. Ghaemi, T. Thio, Electrical conductivity of individual carbon nanotubes, Nature 382, 54-56 (1996)

[1.49] F. Darkrim, D. Levesque, Monte Carlo simulations of hydrogen adsorption in single-walled carbon nanotubes, J. Chem. Phys., Vol. 109, No. 12, 1998

[1.50] C. Liu, Y. Y. Fan, M. Liu, H. T. Cong, H. M. Cheng, M. S. Dresselhaus, Hydrogen Storage in Single-Walled Carbon Nanotubes at Room Temperature, Science Vol 286, 1999, 1127-1129

[1.51] Q. Wang, J. Karl Johnson, Optimization of Carbon Nanotube Arrays for Hydrogen Adsorption, J. Phys. Chem. B 1999, 103, 4809-4813

[1.52] K.A. Williams, P.C. Eklund, *Monte Carlo simulations of H_2 physisorption in finite-diameter carbon nanotube rope*, Chemical Physics Letters 320 2000 352–358

[1.53] C. M. Lieber, C.-C. Chen, *Preparation of fullerenes and fullerene-based materials*, Solid State Physics, Volume 48, 1994, 109-148

[1.54] Kim, Y.-H., Zhao, Y., Williamson, A., Heben, M.J., Zhang, S.B., *Nondissociative adsorption of H_2 molecules in light-element doped fullerenes*, Phys. Rev. Lett. 96, (2006) 016102

[1.55] H. Cheng, G. P. Pez, A. C. Cooper, *Mechanism of hydrogen sorption in single-walled carbon nanotubes*, J. Am. Chem. Soc., Vol. 123, No. 24, 2001

[1.56] N. S. Venkataramanan, H. Mizuseki, Y. Kawazoe, *Hydrogen storage on nanofullerene cages*, NANO: Brief Reports and Reviews Vol. 4, No. 5 (2009) 253–263

[1.57] O. V. Pupysheva, A. A. Farajian, B. I. Yakobson, *Fullerene nanocage capacity for hydrogen storage*, Nano Lett., Vol. 8, No. 3, 2008, 767-774

[1.58] J.-C. Charlier, G.-M. Rignanese, *Electronic structure of carbon nanocones*, Physical Review Letters Vol. 86, No. 26, 2001, 5970-5973

[1.59] A. S. Shalabi, H. O. Taha, K. A. Soliman, S. A. Aal, *Hydrogen storage reactions on titanium decorated carbon nanocones theoretical study*, Journal of Power Sources, 271, 2014, 32–41

[1.60] A. Krishnan, E. Dujardin, M.M. J. Treacy, J. Hugdahl, S. Lynum, T. W. Ebbesen, *Graphitic cones and the nucleation of curved carbon surfaces*, Nature, Vol. 388, 1997, 451-454

[1.61] A. Lua, T. Yang, *Effect of activation temperature on the textural and chemical properties of potassium hydroxide activated carbon prepared from pistachio-nut shell*, Journal of Colloid and Interface Science 274 (2004) 594–601

[1.62] J. Romanos, M. Beckner, T. Rash, L. Firlej, B. Kuchta, P. Yu, G. Suppes, C. Wexler, P. Pfeifer, *Nanospace engineering of KOH activated carbon*, Nanotechnology 23 (2012) 015401

[1.63] N. Bagheri, J. Abedi, *Adsorption of methane on corn cobs based activated carbon*, Chemical Engineering Research and Design 89 (2011) 2038–2043

[1.64] F.-C. Wu, R.-L. Tseng, R.-S. Juang, *Preparation of highly microporous carbons from fir wood by KOH activation for adsorption of dyes and phenols from water, Separation and Purification,* Technology 47 (2005) 10–19

[1.65] D. Lozano-Castello, J.M. Calo, D. Cazorla-Amoros, A. Linares-Solano, *Carbon activation with KOH as explored by temperature programmed techniques, and the effects of hydrogen*, Carbon 45 (2007) 2529–2536

[1.66] T. Kyotani, *Control of pore structure in carbon*, Carbon 38 (2000) 269–286

[1.67] J. Wang, S. Kaskel, *KOH activation of carbon-based materials for energy storage*, J. Mater. Chem., 2012, 22, 23710

[1.68] T. Otowa, Y. Nojima, T. Miyazaki, *Development of KOH activated high surface area carbon and its application to drinking water purification*, Carbon Vol. 35, Issue 9, 1997, Pages 1315-1319

[1.69] M. A. Lillo-Ro´denas, D. Cazorla-Amoro´s, A. Linares-Solano, *Understanding chemical reactions between carbons and NaOH and KOH An insight into the chemical activation mechanism*, *Carbon* 41 (2003) 267–275

[1.70] H.Z. Geng, X.B. Zhang, S.H. Mao, A. Kleinhammes, H. Shimoda, Y. Wu, O. Zhou, *Opening and closing of single-wall carbon nanotubes*, Chemical Physics Letters 399 (2004) 109–113

[1.71] Y. Sun, P. A. Webley, *Preparation of activated carbons from corncob with large specific surface area by a variety of chemical activators and their application in gas storage*, Chemical Engineering Journal 162 (2010) 883–892

[1.72] P. Pfeifer, J. W. Burress, M. B. Wood, C. M. Lapilli, S. A. Barker, J. S. Pobst, R. J. Cepel, C. Wexler, P. S. Shah, M. J. Gordon, G. J. Suppes, S. P. Buckley, D. J. Radke, J. Ilavsky, A. C. Dillon, P. A. Parilla, M. Benham, M. W. Roth, *High-surface-area biocarbons for reversible on-board storage of natural gas and hydrogen*, Mater. Res. Soc. Symp. Proc. Vol. 1041, 2008 Materials Research Society

[1.73] B.-J. Kim, Y.-S. Lee, S.-J. Park, *Novel porous carbons synthesized from polymeric precursors for hydrogen storage*, Int. J. Hydrogen Energy, 2008, 33, 2254

[1.74] Y. Chen, H. Zhu, Y. Liu, *Preparation of activated rectangular polyaniline-based carbon tubes and their application in hydrogen adsorption*, Int. J. Hydrogen Energy, 2011, 36, 11738

[1.75] *C.-C. Huang, H.-M. Chen, C.-H. Chen, J.-C. Huang, Effect of surface oxides on hydrogen storage of activated carbon*, Sep. Purif. Technol., 2010, 70, 291

[1.76] M. Barbatti, G. Jalbert, M. A. C. Nascimento, *The effects of the presence of an alkaline atomic cation in a molecular hydrogen environment*, J. Chem. Phys. Vol. 114, No. 5, 2001, 2213-2218

[1.77] A. Du, Z. Zhu, S. C. Smith, *Multifunctional porous graphene for nanoelectronics and hydrogen storage: new properties revealed by first principle calculations*, J. Am. Chem. Soc. 2010, 132, 2876–2877

[1.78] P. Chen, X. Wu, J. Lin, K. L. Tan, *High H, uptake by alkali-doped carbon nanotubes under ambient pressure and moderate temperatures*, Science, Vol. 285, 1999, 91-93

[1.79] Y. Wang, A. Li, K. Wang, C. Guan, W. Deng, C. Lia, X. Wang, *Reversible hydrogen storage of multi-wall carbon nanotubes doped with atomically dispersed lithium*, J. Mater. Chem., 2010, 20, 6490–6494

[1.80] X. Yu, Z. Tang, D. Sun, L. Ouyang, M. Zhu, *Recent advances and remaining challenges of nanostructured materials for hydrogen storage applications*, Progress in Materials Science 88 (2017) 1-48

[1.81] Q. Sun, P. Jena, Q. Wang, M. Marquez, *First-principles study of hydrogen storage on $Li_{12}C_{60}$,* J. Am. Chem. Soc. 2006, 128, 9741-9745

[1.82] V. B. Parambhath, R. Nagar, K. Sethupathi, S. Ramaprabhu, *Investigation of spillover mechanism in palladium decorated hydrogen exfoliated functionalized graphene*, J. Phys. Chem. C 2011, 115, 15679-15685

[1.83] A. Reyhani, S. Z. Mortazavi, S. Mirershadi, A. Z. Moshfegh, P. Parvin, A. N. Golikand, *Hydrogen storage in decorated multiwalled carbon nanotubes by Ca, Co, Fe, Ni, and Pd nanoparticles under ambient conditions*, J. Phys. Chem. C 2011, 115, 6994–7001

[1.84] G. J. Kubas, *Metal–dihydrogen and σ-bond coordination: the consummate extension of the Dewar–Chatt–Duncanson model for metal–olefin π bonding*, Journal of Organometallic Chemistry 635 (2001) 37–68

[1.85] A. K. Singh, A. Sadrzadeh, B. I. Yakobson, *Metallacarboranes: toward promising hydrogen storage Metal Organic Frameworks*, J. Am. Chem. Soc. 2010, 132, 14126–14129

[1.86] *Q. Sun,* Q. Wang, P. Jena, Y. Kawazoe, *Clustering of Ti on a C_{60} surface and its effect on hydrogen storage*, J. Am. Chem. Soc. 2005, 127, 14582-14583

[1.87] G. K. Dimitrakakis, E. Tylianakis, G. E. Froudakis, *Pillared graphene: a new 3-D network nanostructure for enhanced hydrogen storage*, Nano Lett., 8, 3166-3170 (2008)

[1.88] X. Wu, X. C. Zeng, Periodic Graphene Nanobuds, Nano Lett. 2009 Vol. 9, No. 1, 250-256

[1.89] Z. Ozturk, C. Baykasoglu, M. Kirca, *Sandwiched graphene-fullerene composite: a novel 3-D nanostructured material for hydrogen storage*, Int. J. Hydrogen Energy 41 (2016) 6403-6411

[1.90] B. W. Smith, M. Monthioux, D. E. Luzzi, Encapsulated C60 in carbon nanotubes, Nature, Vol. 396, 1998, 323-324

[1.91] K. Suenaga, S. Iijima, Fine-structure analysis of Gd M45 near-edge EELS on the valence state of Gd@C82 microcrystals, Phys. Rev. B Vol. 62, No. 3, 2000, 1627-1630

[1.92] J. Lee, H. Kim, S.-J. Kahng, G. Kim, Y.-W. Son, J. Ihm, H. Kato, Z. W. Wang, T. Okazaki, H. Shinohara, Young Kuk, *Bandgap modulation of carbon nanotubes by encapsulated metallofullerenes*, Nature, Vol. 415, 2002, 1005-1008

[1.93] B. Kuchta, L. Firlej, Sz. Roszak, P. Pfeifer, *A review of boron enhanced nano-porous carbons forhydrogen adsorption: numerical perspective.* Adsorption 16 (2010) 413-421

[1.94] L. Firlej, Sz. Roszak, B. Kuchta. P. Pfeifer and C. Wexler, *Enhanced hydrogen adsorption in boron substituted carbon nanospaces* . J.Chem.Phys. 131 (2009) 164702

[1.95] J. Kouvetakis, R. B. Kaner, M. L. Sattler, N. Bartlett: A novel graphite-like material of composition BC$_3$, and nitrogen–carbon graphites. J. Chem. Soc., Chem Commun. (1986), 1758

[1.96] C. E. Lowell, *Solid solution of boron in graphite*. J.Am.Ceram.Soc.50 (1966) 142–144

[1.97] Y. Lee, D.-Y. Han, D. Lee, A. J. Woo, S. H. Lee, D. Lee, Y. K. Kim, *11B NMR of boron-doped graphite as the negative electrode of a lithium secondary battery*, Carbon 40 (2002) 403–408

[1.98] L. R. Radovic, M. Karra, K. Skokova, P. Thrower, *The role of substitutional boron in carbon oxidation*, Carbon 36 (1998) 1841–1854

[1.99] M. Endo, T. Hayashi, S. H. Hong, J. T. Enoki, M. S. Dresselhaus, *Scanning tunnelling microscope study of boron-doped highly oriented pyrolytic graphite*. J. Appl. Phys. 90 (2001) 5670–5674

[1.100] C. T. Hach, L. E. Jones, C. Crossland, P. A. Thrower, *An investigation of vapor deposited boron rich carbon—a novel graphite-like material—part I: the structure of BC$_x$ (C$_6$B) thin films*, Carbon 37 (1999) 221–230

[1.101] T. Shirasaki, A. Derre, M. Menetrier, A. Tressaud, S. Flandrois, *Synthesis and characterization of boron-substituted carbons*, Carbon 38 (2000) 1461–1467

[1.102] C. R. Martin, *Nanomaterials: a membrane-based synthetic approach*, Science 266 (1994)1961– 1966

[1.103] H. J. Ceragioli, C. Peterlevitz, J. C. R. Quispe, A. Larena, M. P. Pasquetto, M.P. Sampaio, V. Baranauskas, *Synthesis and characterization of boron-doped carbon nanotubes*. J. Phys. 100, (2008) 052029

[1.104] M. Sankaran, B. Viswanathan, *Hydrogen storage in boron substituted carbon nanotube*s. Carbon 45(2007) 1628–1635

[1.105] K. S. Subramanyan, L. S. Panchacarla, A. Govindaraj, C.N.R. Rao, *Simple method of preparing graphene flakes by an arc-discharge method*, J. Phys. Chem. C 113 (2009) 4257-4259

[1.106] L. S. Panchacarla, K. S. Subramanyam, S. K. Saha, A. Govindaraj, H. R. Krishnamurthy, U. V. Waghmare, C.N.R. Rao, *Synthesis, structure and properties of boron and nitrogen-doped graphite*, Adv. Mat. 21 (2009) 4726-4730

CHAPTER 2

Physical synthesis of nanoporous carbons by electric arc discharge technique and description of characterization methods

The first observation of an electric arc between two well-burned charcoal electrodes was made by Sir Humphry Davy in 1800 [2.1]. Today this method is successfully used to synthesise a large variety of carbon nanostructures like fullerenes [2.3, 2.4], nanotubes [2.2, 2.3], graphene flakes [2.5] or carbon nanostructures substituted by other atoms [2.6].

2.1. Electric arc discharge reactor

We have used the original reactor built in the laboratory in 1991 to synthetize fullerenes C_{60} and C_{70} [2.4]. It consists in cylindrical chamber, closed on both sides by two steel discs (Fig. 2.1). The atmosphere and the pressure inside the reactor can be controlled through two apertures, allowing the connection of a pump and the bottle of an inert gas (usually argon or helium). The reactor construction requires that the pressure inside it during the synthesis does not exceed ambient pressure. A second double wall cylinder, concentric with the reactor walls and cooled by a water circuit, allows a cooling down and condensation of carbon plasma created by arc discharge. Two water cooled copper electrodes are placed on the discs closing the reactor. Their dimensions were set to produce an electric arc in the reactor center. The position of the cathode is fixed. This electrode does not consume during the discharge, but a hard deposit grows onto it. The anode progressively evaporates during the synthesis. It is connected to a manually-operated translation mechanism that pushes it towards cathode, to keep the appropriate distance between the electrodes and maintain the arc discharge. A glass window built into the reactor door enables the observation of the reactor interior during the initial stages of the reaction: as the sublimation progresses, the carbon soot deposits on the reactor walls and obstructs the window.

The cooper electrodes are prepared to hold graphite rods of 6 mm of diameter. To prepare all samples we have used graphite of 99.99% purity.
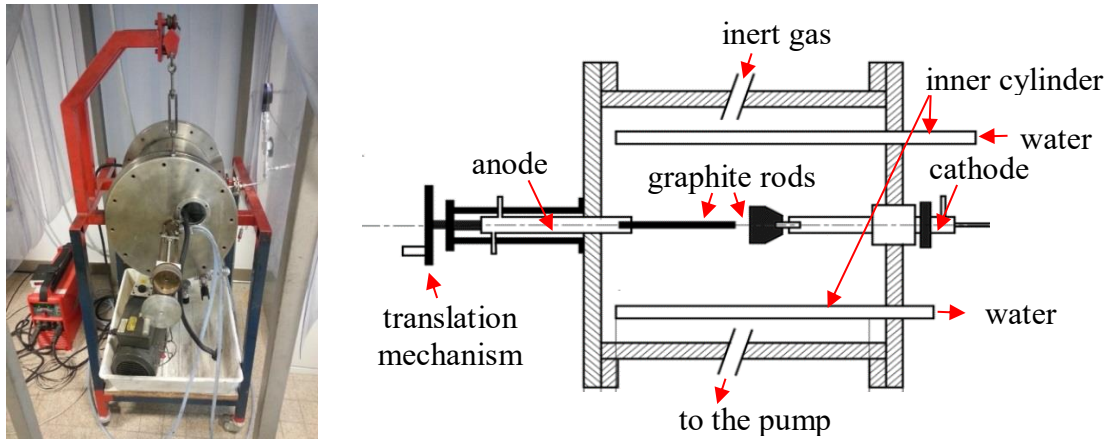
Figure 2.1. The electric arc discharge reactor for synthesis of carbon nanostructures: a) general view of the reactor; b) schematic representation of the reactor cross-section.

2.2. Introduction of heteroatoms into carbon nanostructures

If a part of the graphite electrode is replaced by another material, the plasma created by the electric discharge will contain heteroatoms. We can expect that during condensation of such heterogeneous plasma the heteroatoms will be incorporated into carbon nanostructures. This idea is the basis of our project to prepare heterogeneous nanostructure for efficient storage of hydrogen.

To replace a part of graphite electrode by another material, a cylindrical hole of 3.5 mm of diameter and of the depth of 35 mm was first drilled along the graphite rod axis (Fig. 2.2). The hole was than filled with a powder of the desired material.
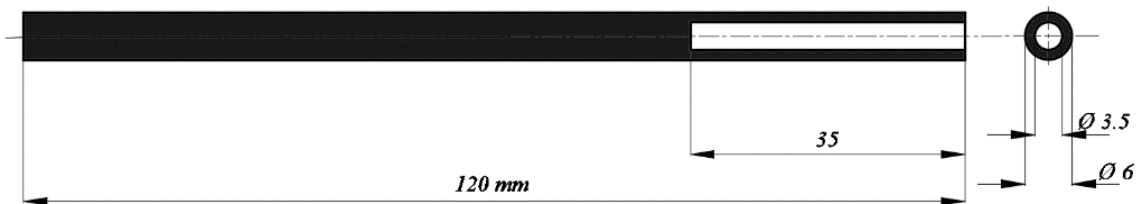

Figure 2.2. Graphite rod prepared to serve as anode containing a powder of non-carbon material to synthetize substituted nanoporous carbons.

Our goal consists in preparing two types of samples: pure nanoporous carbons with high specific surface area and the nanoporous carbons containing various amount of boron atoms incorporated into graphite structure. We prepared the mix of carbon and boron powders to fill the hole in the following (C:B)volume proportions: (1:0), (0.75:0.25), (0.5:0.5), (0.25:0.75) and (0:1). The electrodes filled only with carbon powder were prepared to obtain pure carbon

samples; those filled only with boron powder (100% of filling) were used to obtain samples with the highest boron concentration. The final boron concentration in the samples was estimated assuming that only anode has sublimated during the synthesis. The mass densities d of carbon and boron used to prepare stoichiometric B:C mixtures were $d_C = 1{,}67$ m^3/g and $d_B = 1{,}47$ m^3/g, respectively. The boron concentration after synthesis was estimated according to the formula:

$$B(\%) = \frac{m_{ra} - m_{rb}}{m_{ra} - m_{rest}} \cdot 100\%$$

where m_{rb} is a mass of the rod before filling, m_{ra} is a mass of the rod after filling and m_{rest} is a mass of not sublimated anode, weighted after synthesis. The final values of estimated boron concentrations in prepared samples are given in Table 2.1.

Table 2.1. Estimated boron content in powder filling the electrode and resulting boron concentration in prepared samples.

SAMPLE	Filling concentration of B	Sample concentration of B
1B	100%	23.3%
2B	75%	19.9%
3B	50%	11.3%
4B	25%	5.3%

2.3. Experimental procedure

Before each synthesis the reactor's interior was cleaned with ethanol and the graphite-based rods were installed inside the copper electrodes. The reactor was closed and evacuated until 0.1 mbar, then filled with the inert gas up to 1 atm. The pumping/filling procedure was repeated few times to evacuate all traces of undesirable gases inside the reactor.

The sublimation of graphite in the electric arc can be carried out under dynamic or static atmosphere. Dynamic process involves a constant pumping during the arc discharge and simultaneous refilling of the reactor with the inert gas, to maintain constant pressure inside the reactor. The static procedure consists in filling the purged reactor with the inert gas up to desired pressure and isolating the system. The pressure inside the reactor is monitored; when it is stable, the cooling system is switched on, and the arc discharge can be started.

We have used a standard voltage generator (TransTig 2200 G/F Générateur Inverter TIG DC) to power the arc discharge. Its negative clamp was connected to the cathode and the mass and positive clamp - to the anode. The current/voltage parameters of generator were set to 100 A and 50 V, respectively. The anode was then moved to a distance of ~ 3 mm from the cathode to initiate the arc discharge. When the arc discharge between electrodes appeared, the difference of potential between electrodes dropped to 30 V; the intensity of dc current remained almost constant, ~100 A. These conditions were maintained during the whole synthesis.

The sublimation of the anode in the arc causes the increase of its distance from the cathode. Therefore, to maintain the discharge at the current/voltage parameters given above, the anode was manually moved towards the cathode during the synthesis. The synthesis stopped when there was no more possibility to approach the anode.; it corresponds to a sublimation of ~ 7 cm of graphite rod.

The resulting carbon sample was then collected, respecting the place of its deposition: on the reactor walls - (we call these samples 'soot'), on the top of the cathode (we call them 'deposit'), and around the cathode (we call them 'collar') (Fig. 2.3).
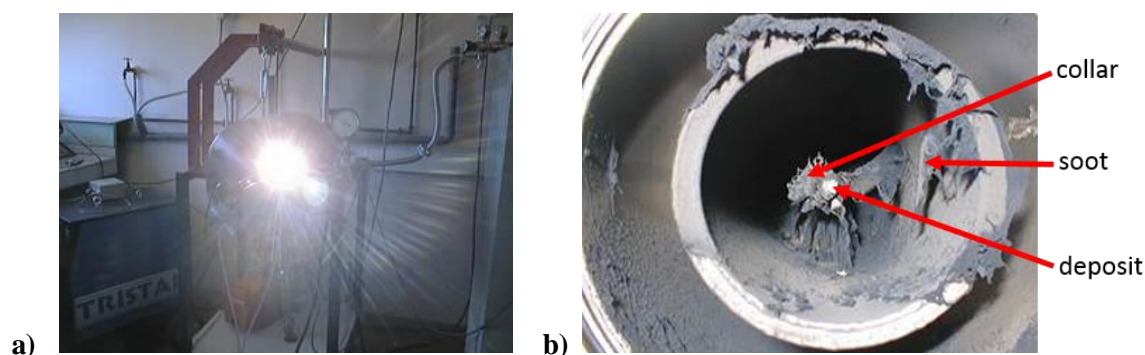

Figure 2.3. a) The reactor during the synthesis: the white light of the discharge is coming out through the glass window in the reactor door; b) the reactor open after the synthesis: the cathode with a deposit is located in the center of the inner cylinder, the webs of soot cover the whole reactor's interior.

The samples synthetized by electric arc discharge technique were characterized using a variety of microscopic and spectroscopic techniques, to obtain information about their morphology, surface topography, and atomic composition. In the following paragraphs we provide a short description of these methods. The obtained results will be described and analysed in chapters 3 and 4.

2.4. Scanning Electron Microscopy (SEM)

Scanning Electron Microscopy (SEM) uses a beam of high energy electrons (with the energy ranging from 0.2 to 40 keV) as a probing tool [2.8]. This electron beam, focused on a sample surface as a spot of about 0.4 nm to 5 nm of diameter, penetrates into the sample at the distance of ~ 100 nm to 5 µm [2.7]. The interaction with the sample leads to a loss of beam energy, mainly by random scattering and absorption. The secondary electrons emitted by the atoms excited by the beam are captured by detectors and used to create sample images. The high-resolution images produced by SEM can reveal the details of sample surface, smaller than 1 nm in diameter.

Samples analysed by SEM should be electrically conductive to prevent the accumulation of electrostatic charge and avoid the scanning faults and artefacts in imaging. Materials with insulating properties are usually coated with thin layer of metal or conductive polymer. As our samples consist in graphitized carbon fragments that are conductive, no pre-coating of sample surface was necessary prior to images collection [2.9].

2.5. High Resolution Transmission Electron Microscopy (HRTEM)

High Resolution Transmission Electron Microscopy (HRTEM) uses electron beam of lower energy than SEM (from 0.1 eV to 3 eV). In HRTEM the beam of electrons is transmitted through a thin sample, interacting with the positive cores of samples atoms, and being diffracted by the atoms' crystallographic planes. Both transmitted and diffracted components of electron waves in outgoing signal interfere to form an image. The resolution obtained using HRTEM can reach 0.5 Å [2.10]. At this scale, individual atoms of a sample can be distinguished. Therefore, HRTEM technique is useful for crystallographic sample characterization, and detection of crystals defects (dislocations, vacancies etc.). At lower magnifications the TEM image contrast results from variation of electrons' absorption by fragments of sample having locally different chemical composition or different thickness. For high magnifications, to avoid an excessive absorption of the beam, usually the sample is prepared in a form of an ultrathin film (less than 100 nm), or as diluted solution deposed on the conducting grid. In our case prior to measurements the carbon-based powder samples were first dispersed in a small amount of methanol, suspended on HOPG supports and positioned inside the FEI Titan 80-300 Cs microscope.

2.6. Electron Energy Loss Spectroscopy (EELS)

In Electron Energy Loss Spectroscopy (EELS) the sample is exposed to a beam of electrons with known and very narrow range of kinetic energies. Passing through the sample, the electrons lose their energy in inelastic processes (phonons and plasmon excitations, inter- and intra-band transitions, ionization of atoms' inner shell, and Cherenkov radiation). The loss of electrons' energy is usually detected by the electron spectrometer of HRTEM microscope. The spectrum consists in electron counts in function of electron energy loss (given in eV). This information allows one to determine the amount and the type of atoms being struck by the electron beam, thus, to determine chemical composition of the sample [2.11]. As our samples contain nominally the carbon and boron atoms only, we used the beam of electrons having the kinetic energy from the range of 100 – 300 eV: the carbon and boron signals should appear around 285 eV and 200 eV, respectively.

2.7. X-Ray Diffraction (XRD) and powder X-Ray Diffraction (PXRD)

X-Ray Diffraction (XRD) is used to analyze fully (or at least partially) crystallized materials. The measurements consist in irradiation of the sample with monochromatic X-rays (their wavelength λ is comparable to the distance d between crystallographic planes, from 1 to 100 Å) and recording of waves scattered by sample atoms. The constructive interference of output waves occurs in specific directions determined by Bragg's law [2.12]:

$$2d sin\theta = n\lambda$$

where θ is an incident angle of the beam. These interferences form sample diffraction pattern. In the case of powdered samples, when every crystalline orientations of powder grains with respect to the incident X-ray beam is possible, the Debye-Sherrer powder XRD diffraction method (PXRD) should be used to collect the diffraction pattern. The method consists in rotation of the sample during its exposure to X- ray radiation, to average out the effect of random distribution of crystallites. Scattered radiation (Debye-Sherrer cones, Fig. 2.4) is collected on a detector plate in form of smooth diffraction rings surrounding the spot of incident radiation beam [2.12].

We used this technique to study the powdered samples prepared in the present work. The samples were loaded inside the 0.7 mm capillary and exposed to X-rays during 720 s (step-time 3.5°/min). We used a diffractometer with copper rode as a source of X-ray radiation (λ = 1.5418Å, beam size of 0.5 mm^2). The configuration of image plate detector (Mar345) allowed

the observation of diffraction rings up to $2\Theta = 65°$, with the resolution of $\sim 0.3°$. The maximum 2Θ value is limited by both: the detector size, and the minimum possible distance between sample and detector. The observed diffractograms were compared with the database included in the equipment software.
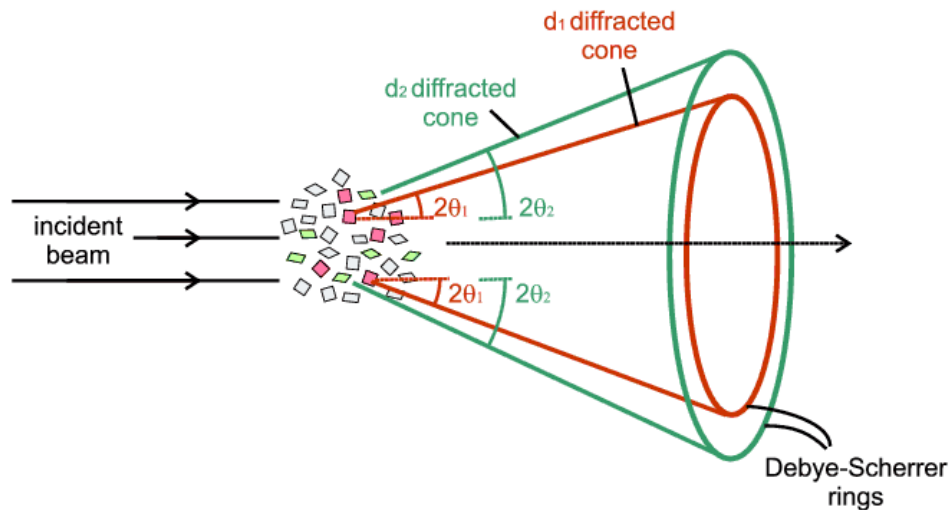

Figure 2.4. Debye Sherrer powder diffraction method [2.13].

2.8. Energy Dispersive X-ray Spectroscopy (EDS)

EDS microanalysis technique is used for elemental analysis (volumetric and areal) of atomic composition of materials. The sample is exposed to an incident beam of high energy electrons that, passing through the sample, excite the electrons from the outer shell of the atom, eject them and create the holes in the atoms' electronic shells. These holes can be filled by the electrons from higher-energy shell of the same atom. During this process the electron's energy excess is released the in form of X-ray radiation. Its energy and intensity are measured by energy-dispersive spectrometer. As radiation energy is characteristic for each element, its analysis allows the determination of sample atomic composition [2.14]. Theoretically, this technique can detect all elements with atomic number Z higher than 3. The results of analysis are presented in form of spectrum giving radiation intensity in a function of radiation energy. Since EDS is a part of the microscope, the atomic composition of a chosen sample fragment can be obtained in form of colour map, each colour corresponding to different element.

2.9. ^{13}C and ^{11}B MAS Nuclear Magnetic Resonance spectroscopy (NMR)

Nuclear Magnetic Resonance (NMR) spectroscopy can be used to study any sample containing nuclei with magnetic momentum (non-zero spin). This condition is fulfilled in isotopes that have different numbers of neutrons and protons; it is also the case of ^{13}C and ^{11}B isotopes. In the external static magnetic field (usually from 1 to 21 Tesla) the magnetic moments orient along the field direction. The detection of the NMR signal consists in reorientation of the sample magnetization by the radiofrequency (60-1000 MHz) pulse and observation of (i) the frequency of the signal emitted by the excited sample, and (ii) the time of the magnetization return to the initial value and orientation. The shift between the frequency of the impact signal (resonance frequency for a given nucleus) and the signal emitted by the sample is called the chemical shift δ. It is a small relative value, established with respect to the signal of reference material (different for each nuclei), and is expressed in ppm [2.15].

As the frequency and the intensity of the emitted signal depends on the nature and the local environment of a given nuclei, the value of chemical shifts and the intensity of the NMR resonances provide information about the intramolecular electronic structure of the material. Therefore, this technique is widely used by chemists, to determine chemical composition of the samples and to identify the reactions' products and yields. In organic chemistry, the liquid state NMR is mostly used, as all direction-dependent components of interaction between nuclear spins are averaged out because of the rapid, isotropic reorientations of molecules [2.16].

When the molecular motion is slow, in viscous fluids, gels, and solid samples (crystalline or not), the anisotropy of intramolecular interactions (J-coupling, dipolar, quadrupolar etc.) and of the internal magnetic field (causing the anisotropy of chemical shift) lead to significant broadening of the NMR resonances. In such cases, to detect sample NMR signal, Magic Angle Spinning (MAS) procedure has to be used. It consists in fast spinning of the sample around the axis forming an angle of 54.74^0 ('magic angle') with respect to direction of external magnetic field, to average all angle-dependent components of intermolecular interactions and increase the resolution of NMR spectrum [2.12].

In conducting samples, the position of NMR resonance results not only from the non-zero spin density of electrons localized at the atomic orbitals (and responsible for chemical shift), but also from the density of delocalized (conduction) electrons, inducing an additional paramagnetic shift (so called Knight shift) of resonances [2.17]. In organic conductors (as our samples) the density of the π electrons that are responsible for electric conduction is zero at the

atomic nuclei. In such cases the interpretation of NMR spectra is difficult. The Knight shift, if it exists, is an indirect effect, resulting from polarization of inner electronic orbitals of atoms by the electrons localized on neighbouring atoms.

In the present work both: the ^{13}C and ^{11}B high resolution (HR) MAS NMR experiments were carried out using solid state Bruker Avance IIHD-400 MHz NMR spectrometer, operating at 9.4 T. The carbon (or carbon-boron) powders were loaded inside a cylindrical ZrO_2 tube (rotor), 4 mm in diameter, 2.5 cm of length, capped with a Kel-F turbine-like cap. To ensure high resolution, the samples were rotated at the MAS frequency of 10 kHz. In these conditions the resonance frequencies for ^{13}C and ^{11}B nuclei are 101.6 MHz and 128.4 MHz, respectively. The ^{13}C chemical shifts were referenced to tetramethylsilane (TMS) and calibrated with glycine carbonyl signal (set at 176.03 ppm). The ^{11}B chemical shifts were referenced to H_3BO_3 0.1 M solution, which resonance was set to 0 ppm. The spectra were analyzed using Bruker TopSpin software.

2.10. Characterization of porous structure using gas adsorption measurements

The adsorption is an isothermal process where fluid (gas or liquid) called *adsorptive*, interacts with surface of solid or liquid (*adsorbent*). The process is a consequence of the differences between surface and adsorbent energies.

Two types of adsorption can be distinguished: chemisorption and physisorption. In the chemisorption, chemical bond is formed between adsorbent and adsorptive. The adsorption energy depends on chemical nature of both components, and ranges from 30 to 70 kJ/mol for molecules' adsorption, and from 100 to 400 kJ/mol for atoms. Chemisorption causes structural modifications of interacting species. The process is irreversible without external energy input (f.ex. in a form of thermal treatment [2.23]). In physisorption, weak van der Waals forces, resulting from fluctuating polarizations, are responsible for interactions between adsorbent and adsorbate. The physical sorption involves lower adsorption energies (up to 40 kJ/mol [2.24]), therefore it is reversible, contrary to chemisorption. As in most of materials the process occurs without any structural changes of the adsorbent, the measurements of adsorption allow to recover information about sample morphology: its specific surface area and distribution of pore sizes (if the adsorbent is porous).

2.10.1. Theoretical background

The relation between adsorbent surface and adsorbed layer is presented on Fig. 2.5. The local concentration ($c = dn/dV$) of adsorbed phase is assumed to decrease with increasing distance (z) from the surface until bulk fluid phase concentration c^f is reached at certain distance (r), where the fluid is no more interacting with adsorbing surface. The region between surface and bulk phase delimits an adsorbed layer; the adsorbed amount is defined as n^a.
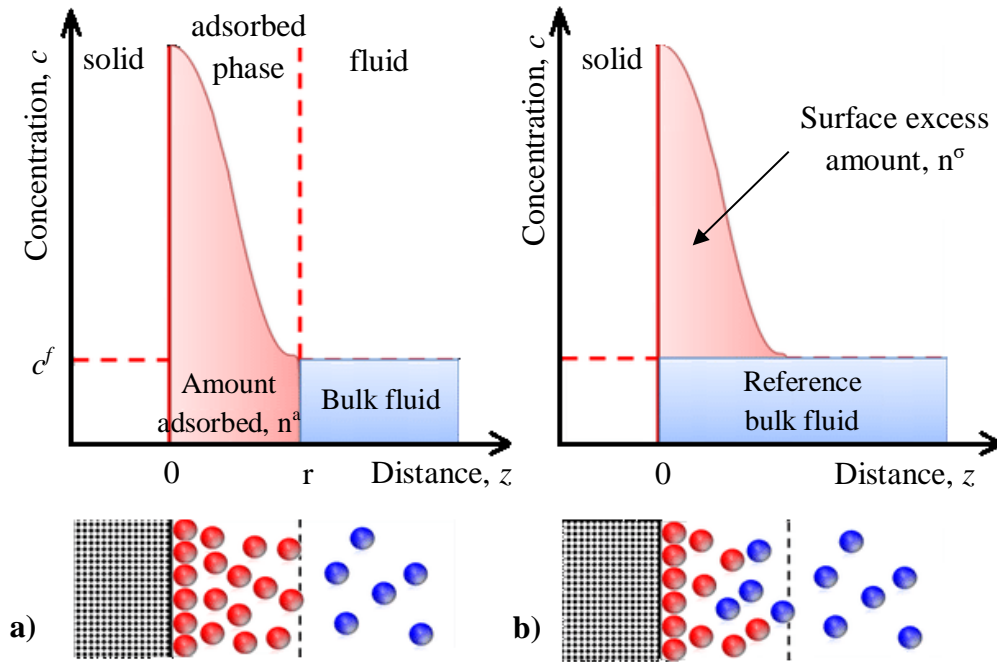

Figure 2.5. Schematic representation of adsorption phenomenon by a) layer model and b) the Gibbs representation.

According to layer model, the adsorbed amount (red area, Fig. 2.5a) can be calculated from the formula:

$$n^a = A \int_0^r c \, dz \qquad \text{(Eq. 2.1)}$$

where A is the surface area of adsorbent on which adsorption can occur. The amount adsorbed is referred to total amount adsorbed (n):

$$n^a = n - c^f \cdot V^f \qquad \text{(Eq. 2.2)}$$

where V^f is the volume occupied by bulk fluid phase when adsorption equilibrium is reached. The product of $c^f \cdot V^f$ represents the amount of fluid which is not adsorbed – bulk fluid region.

In practice, the concentration profile or volume of the bulk fluid V^f are difficult to estimate. To overcome this problem, Gibbs proposed a slightly different representation of adsorption (Fig. 2.5b). Gibbs concept introduces excess amount adsorbed (or surface excess amount) n^σ, defined as a difference between total amount of the adsorptive in the volume $V^{f,0}$ and the amount of bulk fluid which would be present in this volume in the absence of adsorbent. The n^σ can be thus calculated from the equation:

$$n^\sigma = n - c^f \cdot V^{f,0} \qquad (Eq.\ 2.3)$$

The reference volume $V^{f,0}$ contains the volume of adsorbed phase V^a and the volume of remaining bulk fluid V^f:

$$V^{f,0} = V^a + V^f \qquad (Eq.\ 2.4)$$

Excess amount adsorbed is then expressed as a function:

$$n^\sigma = n - c^f \cdot V^a - c^f \cdot V^f \qquad (Eq.\ 2.5)$$

The relation between amount adsorbed and the excess amount is derived as follows:

$$n^a = n^\sigma + c^f \cdot V^a \qquad (Eq.\ 2.6)$$

Usually, the excess amount is measured in the adsorption experiments. The volume of reference system can be determined from total free volume of the measurement cell and the volume of the adsorbent, or from inert gas adsorption experiment. For that, helium is the most frequently used, as it is considered as a non-adsorbing gas.

When the adsorption experiment is carried out at low pressures, the values of adsorbed amount n^a and excess amount n^σ are comparable, and the term $c^f \cdot V^a$ is negligible.

In the case of porous materials, the adsorbed volume V^a, is considered as a total porous volume V^p; the amount of liquid adsorbed on the external surface of the adsorbent is assumed negligible with comparison to the one adsorbed in pores. The adsorbed amount is expressed in mols per gram unit of adsorbent, for each equilibrium pressure. Such representation of the gas-solid equilibrium in constant temperature is called adsorption/desorption isotherm:

$$n^a / m^s = f(p)_T \qquad (Eq.\ 2.7)$$

where m_s is the mass of adsorbent; the pressure is usually expressed as a fraction of fluid saturation pressure p^0.

2.10.2. Classification of gas physisorption isotherms

The analysis of adsorption isotherm allows to retrieve valuable information about the adsorptive (f.ex. its specific surface area or distribution of pore sizes). For porous materials the adequate choice of testing fluid (that can access all sample pores) influences the quality of this information. For microporous solids (with pore sizes smaller than 2 nm) the probing gases of small effective diameter (helium, argon, nitrogen, carbon dioxide) should be used. For characterization of mesoporous and macroporous solids (pore sizes of 2-50 nm and larger than 50 nm, respectively), nitrogen, argon, carbon monoxide and methane can be used [2.18].

International Union of Pure and Applied Chemistry (IUPAC) proposed classification of adsorption isotherms into six main types (Fig. 2.6).

The type I isotherms are reversible. They are characterized by sharp rise at low relative pressures followed by the nearly horizontal plateau extending over a wide range of pressures. Such characteristics indicate that the distribution of pore sizes in the material is narrow. Type Ia isotherm is characteristic to materials with narrow micropores, whereas Type I(b) isotherm indicates the presence of wider micropores [2.18].

The type II isotherm has concave shape for low relative pressures and becomes convex close to saturation pressure. This isotherm is characteristic for non-porous or microporous adsorbents. When the equilibrium pressure equals the saturation vapour pressure, the adsorbed layer becomes a bulk liquid or solid [2.18]. Type IIa isotherm is reversible, the isotherm type IIb is not; the narrow hysteresis loop is a result of inter-particular capillary condensation.

The isotherm type III is convex at all relative pressures and characterizes macro- or non-porous solids [2.18].

The type IV isotherm is similar to type II isotherm at low pressures. Type IVa isotherm is more commonly observed than type IVb isotherm. The presence of hysteresis between adsorption and desorption branch is a result of filling/emptying of mesopores by capillary condensation. Type IVb isotherm is reversible and has been observed for example for mesoporous silicas like MCM-41 [2.18].

The type V isotherm is convex at low pressures. It is characteristic for micro- and mesoporous solids with weak adsorbent-adsorbate interactions. It usually exhibits an adsorption/desorption hysteresis loop [2.18].

The type VI isotherm is associated with layer-by-layer adsorption on a highly uniform surface. They are frequently observed in graphitised carbon. The shape and length of the steps depends on the system geometry and the temperature [2.18].
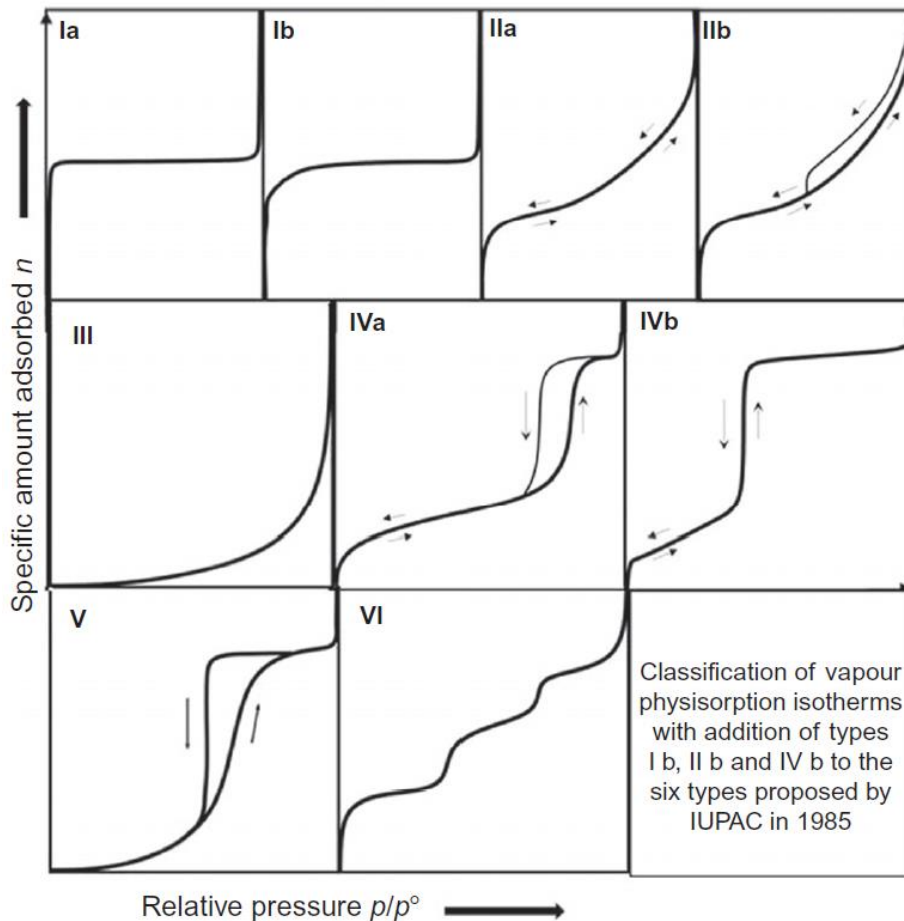

Figure 2.6. Classification of vapour adsorption isotherms combining proposals from IUPAC [2.18].

2.10.3. Brunauer-Emmett-Teller (BET) method

The surface area and adsorption capacity of porous powders can be calculated from adsorption isotherms using BET procedure. The theoretical background of the method was set by Brunauer, Emmett and Teller who described multilayer adsorption of the single fluid adsorbate in the solid adsorbent by following equation:

$$\frac{p/p^0}{n(1-p/p^0)} = \frac{1}{n_m^a C} + \frac{C-1}{n_m^a C}\left(\frac{p}{p^0}\right)$$

(Eq. 2.8)

where n is the amount of gas adsorbed at the relative pressure p/p^0 and n_m^a is the monolayer capacity (the quantity of fluid that can be adsorbed in the first (contact) layer). Parameter C in BET theory is a coefficient related to energy of the adsorption of fluid molecules in the contact layer. It depends on chemical nature of both adsorbent and adsorbate, and on temperature [2.18].

If the BET relation is plotted in the restricted range of pressures (generally $0.05 < p/p^0 < 0.35$), the capacity and the volume of the monolayer (V_m and n_m^a, respectively), and C constant can be calculated from the slope s and y-intercept i of the curve:

$$n_m^a = \frac{1}{s+i} \tag{Eq. 2.9}$$

and

$$C = \frac{s}{i} + 1 \tag{Eq. 2.10}$$

Using the value of n_m^a or V_m calculated from (Eq. 2.9), the specific surface area (SSA, in m^2/g) can be obtained from the formula

$$SSA = n_m \cdot N_A \cdot \sigma \tag{Eq. 2.11}$$

where N_A is the Avogadro number, and σ is a surface of molecule/atom of fluid. To characterize microporous materials, usually the measurements of nitrogen adsorption at 77 K are carried out. The surface σ of nitrogen molecule is equal $0{,}162 \cdot 10^{-18} \ nm^2$.

2.10.4. Barrett-Joyner-Halenda (BJH) method

BJH method is based on the concept of capillary condensation and evaporation. Capillary condensation consists in gas condensation at pressure lower then saturation vapour pressure p^0. It begins by the formations of a meniscus of fluid close to the pore wall. The relative pressure at which condensation takes place depends on pore diameter. The relation between these two parameters is provided by Kelvin equation:

$$r_K = \frac{-2 \cdot \gamma \cdot V_M}{R \cdot T \cdot ln\left(p/p^0\right)} \tag{Eq. 2.12}$$

where r_K is a Kelvin radius of the pore where condensation occurs, γ is the surface tension, V_M is the molar volume of liquid adsorptive, R is the ideal gas constant, T is the temperature of the boiling point of adsorptive (for N_2, T=77 K) and p/p^0 is the relative pressure. The relation between Kelvin radius (r_K) and pore radius (r_p)

$$r_p = r_K + t \qquad \qquad \text{(Eq. 2.13)}$$

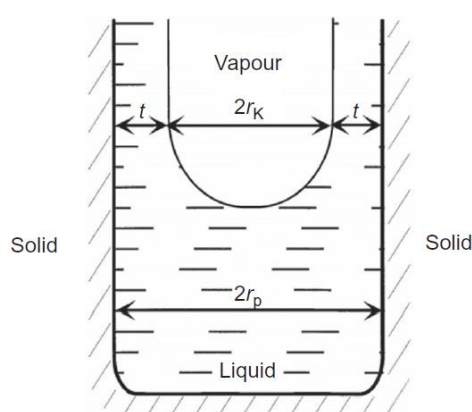where t is the thickness of the adsorbed layer, is illustrated on Fig (2.7).

Figure 2.7. Relation between the Kelvin radius r_K and the pore radius r_p in a cylindrical mesopore [2.18].

2.10.5. de Boer method (t-plot)

External sample surface and micropore volume are usually evaluated using de Boer method, commonly called t-plot method. It assumes the model adsorption isotherm of probing gas (nitrogen) on a flat surface S. By assuming that the gas average density is equal to bulk liquid density ρ_0, the number of adsorbed molecules ($N_{ads}^0(P)$) can be converted into the average thickness of the film adsorbed on the surface: $t(P) = N_{ads}^0(P)/\rho_0 S$. The function $t(P)$ is called a t-curve [2.18, 2.19]. The t-plot is obtained by plotting (for each pressure) the adsorbed amount $N_{ads}(P)$ as a function of $t(P)$. The linear regime of the t-curve is considered as corresponding to the adsorption on flat surface: the slope of the line gives then the value of adsorption area in that pressure regime. In the case of microporous solids, none of the linear regimes are getting through the origin of the t-plot, and the intercept of the linear fit in the low-pressure range is usually taken as the microporous volume of the solid [2.19].

For carbon samples the distribution of pore sizes is usually calculated using Horvath-Kawazoe (HK) model of nitrogen adsorption in microporous solids. HK method was originally conceived for determination of pores sizes in graphitic materials. The method assumes slit-like shape of pores and compares the relative pressure required for the filling pores of a given size and shape with the experimental isotherm (supposed to result from combination of adsorption in individual slits) [2.18]. The methods of determination of distribution of sizes of cylindrical and spherical pores are also described in the literature [2.20, 2.21].

2.10.6. Experimental setup description

Porosity measurements were carried out using ASAP 2010 Micromeritics apparatus (Fig. 2.8) with 5% of accuracy. The analyzer was equipped in two independent vacuum systems – one for sample degassing, and the other for sample analysis with saturation pressure tube. Two cold trap tubes are located inside the cold trap Dewar between the vacuum pomp and the manifold in both systems.

For each measurement 50 to 100 mg of the sample was placed inside the glass bulb cell with a filler glass rod (to reduce the free-space volume) and closed by seal frit (Fig. 2.9). The cell was first placed in the degassing circuit and evacuated to the pressure of 1 mbar. Then the sample was heated to 250 $^{\circ}$C and degassed during ~ 12 h, until the pressure of ~ 0.01 mbar has been reached. A heating mantle has been used to maintain the temperature constant during thermal treatment. Then the cell was cooled down to the ambient temperature with the probing gas (nitrogen) and atmospheric pressure. This procedure is supposed to remove adsorbed water and other volatile contaminants from the sample. The degassing procedure completed, the sample was placed inside the isothermal jacket and installed in the analysis port of the apparatus, above the elevator containing analysis Dewar filled with liquid nitrogen.
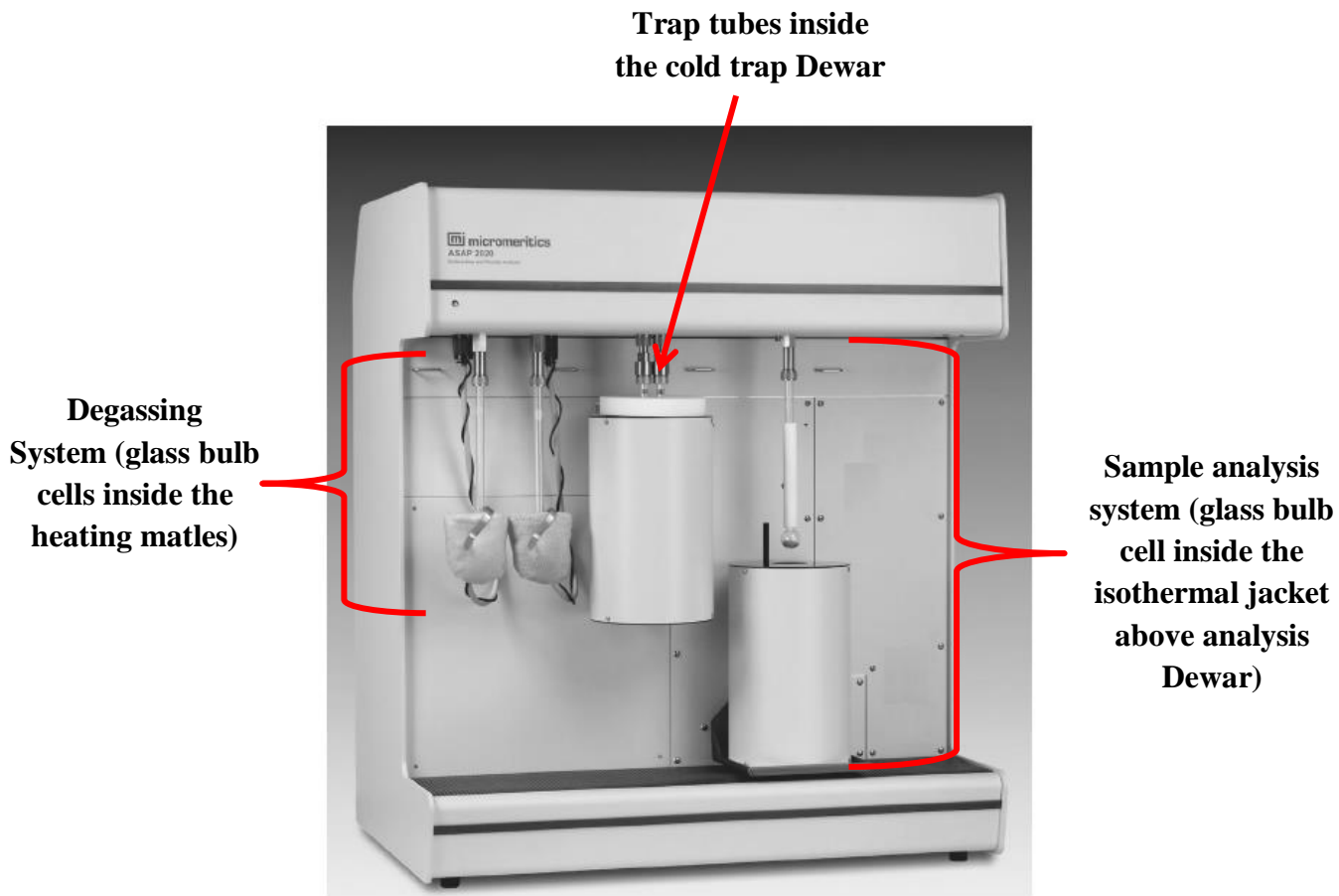
Trap tubes inside the cold trap Dewar

Degassing System (glass bulb cells inside the heating matles)

Sample analysis system (glass bulb cell inside the isothermal jacket above analysis Dewar)
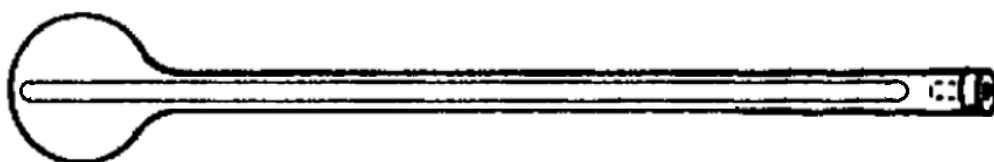
Figure 2.8. ASAP 2020 apparatus [2.22].

Figure 2.9. Glass bulb cell used for measurement with filler glass rode and seal frit.

In the first state of analysis the sample containing glass tube is degassed again and filled with helium to get information about the free (dead) volume in the tube at both: room temperature (~298 K) and analysis bath temperature (77 K). This information is required to evaluate correctly the number of molecules of nitrogen that will be adsorbed by the sample during the experiment carried out at 77 K.

2.11. Bibliography

[2.1] H. M. Ayrton, *Electric arc*, New York, USA, 1980

[2.2] C. Journet, P. Bernier, *Production of carbon nanotubes*, Appl. Phys. A 67, 1-9 (1998)

[2.3] Y. Su, Y. Zhang, *Carbon nanomaterials synthetized by arc discharge hot plasma*, Carbon Vol. 83, 90-99 (2015)

[2.4] A.-A. Zahab, *Synthese, carcterization et etude physique des fullerenes C60 et C70 et de leurs derives*, PhD thesis, Montpellier, France, 1992

[2.5] K. Subrahmanyam, L. Panchakarla, A. Givindaraj, *Simple method of preparing graphene flakes by an arc-discharge method*, Society Vol. 113, 4257-4259, 2009

[2.6] D. Gourari, M. Razafinimanana, M. Monthioux et al., *Synthesis of (B-C-N) nanomaterials by arc discharge using heterogeneous anodes*, Plasma Science and Technology Vol. 18, No. 5 465-468 (2016)

[2.7] R. W. Kelsall, I. W. Hamley, M. Geoghegan: *Nanotechnologie*. Warszawa: Wydawnictwo Naukowe PWN, 2008, p. 77

[2.8] G. Dehm, J. M. Howe, J. Zweck, In-situ Electron Microscopy: Applications in Physics, Chemistry and Material Science, Germany: WILEY-VCH, 2012, p. 6

[2.9] G. Dehm, J. M. Howe, J. Zweck, In-situ Electron Microscopy: Applications in Physics, Chemistry and Material Science, Germany: WILEY-VCH, 2012, p. 30

[2.10] C. Kisielowski, B. Freitag, M. Bischoff, H. van Lin, S. Lazar, G. Knippels, P. Tiemeijer, M. van der Stam, S. von Harrach, M. Stekelenburg, M. Haider, S. Uhlemann, H. Müller, P. Hartel, B. Kabius, D. Miller, I. Petrov, E.A. Olson, T. Donchev, E.A. Kenik, A.R. Lupini, J. Bentley, S.J. Pennycook, I.M. Anderson, A.M. Minor, A.K. Schmid, T. Duden, V. Radmilovic, Q.M. Ramasse, M. Watanabe, R. Erni, E.A. Stach, P. Denes, and U. Dahmen, *Detection of single atoms and buried defects in three dimensions by aberration-corrected electron microscope with 0.5-Å information limit*, Microsc. Microanal. 14, 469-477, 2008

[2.11] R. F. Egerton, *Electron energy-loss spectroscopy in TEM*, Rep. Prog. Phys. 72 (2009) 016502

[2.12] A. K. Cheetham, P. Day, *Solid state chemistry techniques*, Oxford Science Publications, Oxford University Press, New York 1987, ISBN 0-19-855165-7

[2.13] http://pd.chem.ucl.ac.uk/pdnn/diff2/kinemat2.htm last access: 05/02/2018

[2.14] J. I. Goldstein, D. E. Newbury, J. R. Michael, N. W. M. Ritchie, J. H. J. Scott, D. C. Joy, *Scanning Electron Microscopy and X-Ray Microanalysis*, Springer-Verlag New York, 2018

[2.15] F. A. Bovey, *Nuclear Magnetic Resonance Spectroscopy*, Second Edition, 1988 California, USA, ISBN 0-12-119752-2

[2.16] M. Rückert, G. Otting, *Alignment of biological marcomolecules in novel non-ionic liquid crystalline media for NMR experiments*, J. Am. Chem. Soc. 2000, 122, 7793-7797

[2.17] W. D. Knight, *Nuclear Magnetic Resonance shift in metals*, Phys. Rev. 76, 1259-1260, 1949

[2.18] F. Rouquerol, J. Rouquerol, K.S.W. Sing, P. Llewellyn, G. Maurin, *Adsorption by Powders and Porous Solids – Principles, Methodology and Applications*, 2nd edition 2014, Elsevier, ISBN: 978-0-08-097035-6

[2.19] A. Galarneau, F. Villemot, J. Rodriguez, F. Fajula, B. Coasne, *Validity of the t-plot Method to Assess Microporosity in Hierarchical Micro/Mesoporous Materials*, Langmuir 2014, 30, 13266−13274

[2.20] L. S. Cheng, R. T. Yang, *Improved Horvath-Kawazoe equations including spherical pore models for calculating micropore size distribution*, Chemical Engineering Science, Vol. 49, No. 16, 2599-2609, 1994

[2.21] L. S. Cheng, R. T. Yang, *Predicting isotherms in micropores for different molecules and temperatures from a known Isotherm by improved Horvath-Kawazoe equations*, Adsorption, 1, 187-196 (1995)

[2.22] ASAP 2020, Accelerated Surface Area and Porosimetry System, Operator's Manual V4.01, Micromeritics 2011

[2.23] D. S. Ballantine, Jr., Robert M. White, S. J. Martin, Antonio J. Ricco, E. T. Zellers, G. C. Frye, H. Wohltjen, *Acoustic Wave Sensors: Theory, Design and Physico-Chemical Applications*, Academic Press, USA 1997, ISBN 0-12-077460-7

[2.24] I. Johansson, P. Somasundaran, *Handbook for cleaning/decontamination of surfaces*, Elsevier 2007, ISBN 978-0-444-51664-0

CHAPTER 3

Characterisation of adsorptive properties of nanoporous carbons prepared by arc discharge procedure

To determine whether it is possible to prepare nanoporous carbons by electric arc discharge technique (described in chapter 2.1), pure carbon samples were first synthetized and analysed. We will consider them as a reference material for boron-substituted carbons. It will allow the optimisation of the synthesis and activation procedure on samples that are non-expensive. Moreover, their analysis will serve to determine the relations between the conditions of the sample preparation and post-synthesis treatment, and the sample morphology.

3.1. Synthesis of the carbon samples

The optimal conditions of graphite sublimation in controlled, inert gas atmosphere that are necessary to produce closed carbon structures (fullerenes and carbon nanotubes) were determined by Zahab [3.1] and Journet [3.2]. The same electrical parameters of synthesis were used in the present study. The voltage between graphite electrodes was set to 50 V. The intensity of the electric current between electrodes was maintained constant and equal 100 A during the sublimation process. That was achieved by regulating the distance between the stationary cathode and the anode that consumes itself during sublimation. We focused only on the optimization of the inert gas pressure in the reactor. The gas acts as a mass/charge/heat carrier in plasma produced in the electric arc. Its pressure influences the mechanism of carbon nanostructures growth and determine which type of structures will be formed [3.3]. The electric arc discharge method was used in the past to prepare in the selective way closed carbons structures (fullerenes C_{60}, C_{70}, and higher, single-, double- or multi-wall nanotubes etc.). On the contrary the goal of present work is to prepare very disordered, open carbon structures build from small graphene fragments and highly nanoporous. The influence of inert gas (helium) pressure in the reactor on the type and properties of the prepared carbons was then examined, in the pressure range between 660 and 1100 mbar. We recall that the reactor was conceived to operate under pressures lower that ambient pressure (1 bar) and 1100 mbar is the highest-pressure value that we could use during synthesis without overpassing the security limits. On the other hand, 650 mbar is the minimum pressure that allows the sublimation (and not melting) of graphite electrodes in the reactor.

3.2. Morphology of as-prepared carbon powders

The morphology of the obtained carbon soot was analysed using electron microscopies (SEM and HRTEM). Sample specific surface and porosity were determined from N_2 adsorption measurements.

3.2.1. Electron microscopy measurements (SEM and HRTEM)

Fig 3.1 shows the SEM images for two carbon samples synthetized using the smallest (660 mbar) and one of the largest (960 mbar) helium pressure in the reactor. In both cases the sample morphology is very similar. The sample surface is irregular and spongy, with many pores of nanometric size. However, the SEM resolution does not allow for identification of differences between samples. Therefore, we continued our analysis using HRTEM technique.
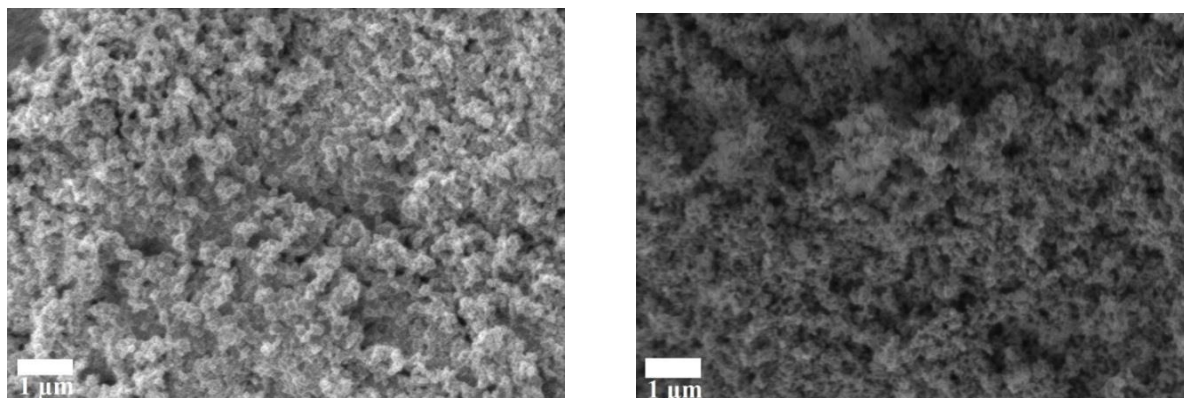
Figure 3.1. SEM images of carbons synthetized using (left) 660 mbar and (right) 960 mbar helium pressure in the reactor.

Figure 3.2 compares the HRTEM images of samples synthesized using 660 mbar (left panel) and 1100 (right panel) helium pressure. Samples prepared at low helium pressure consist in amorphous agglomerates. Any specific graphene-based structure (onions, tubes) is observed even at higher magnification (Fig. 3.2c). The agglomerated structure is homogeneous across the whole sample. It consists in entangled graphene fragments (Fig. 3.3). The structure is porous, and the average pore diameter is of the order of the 5.6 Å. The pore of this size, if they are open (accessible for the adsorbate) are suitable for hydrogen storage. As the structure is built from graphene fragments that present a lot of edges, this additional edge surface can constitute a suitable adsorption surface that will add to the pore surface.
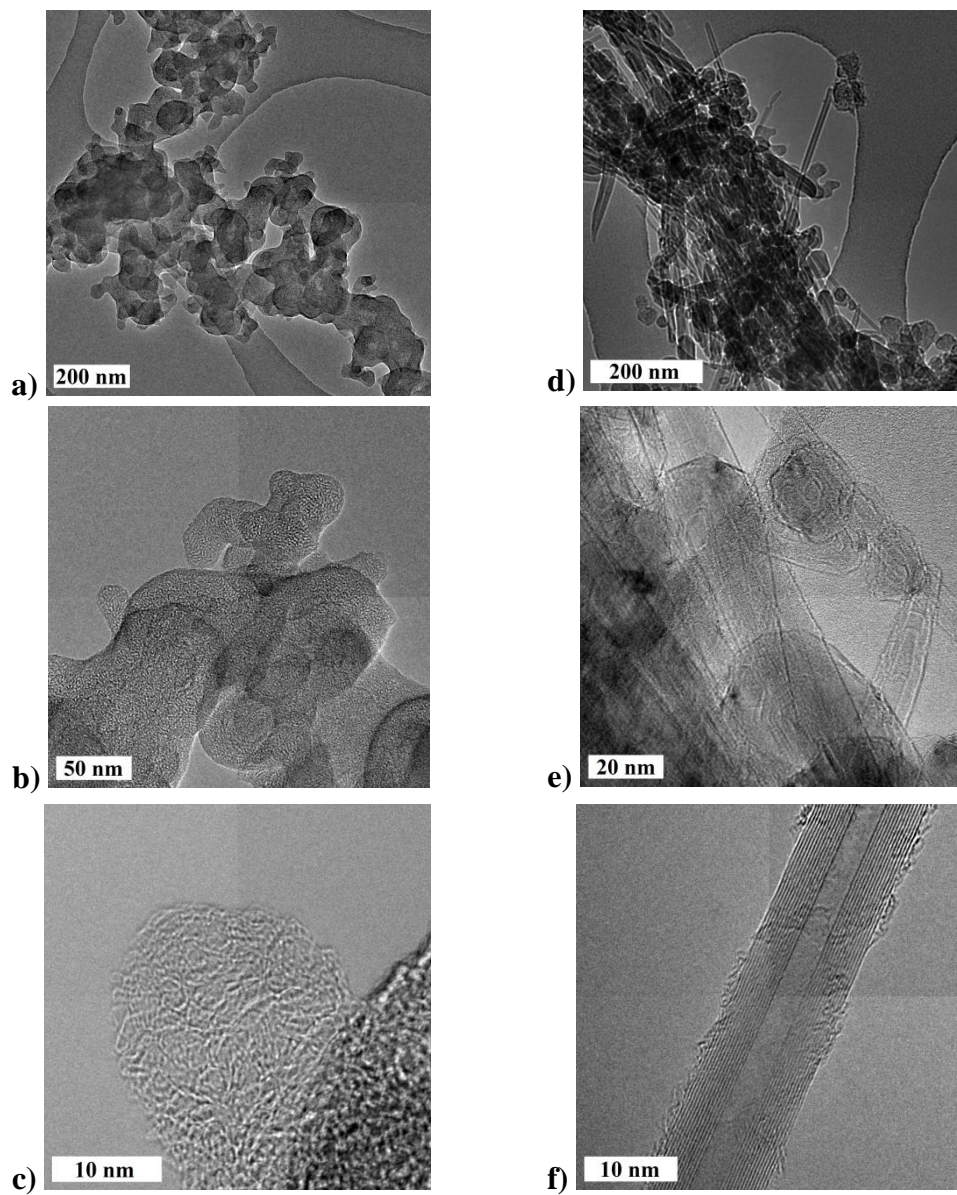
54

Figure 3.2. HRTEM images of carbon sample synthetized in 660 mbar (left pannel) and 1100 mbar (right panel) helium pressure.
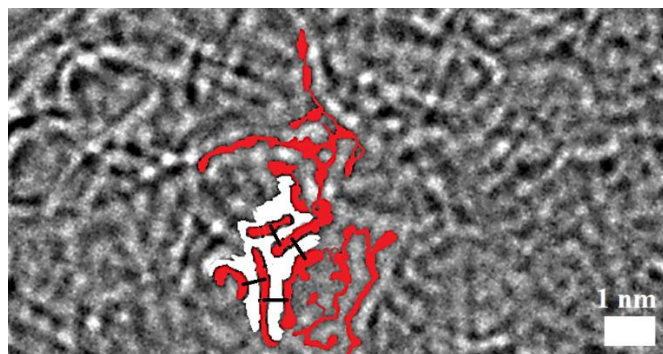
Figure 3.3. HRTEM images of carbon sample synthetized at 660 mbar of helium pressure. Withe (grey) regions are the pores; red (dark) lines correspond to carbon skeleton. Black thin illustrate the pore width. The average distance measured between the pore walls is 5.6 Å.

In samples obtained at the highest helium pressure the images show the presence of organized structures, partially surrounded by amorphous carbon (Fig. 3.2d). These structures are closed (Fig. 3.2e) and form the nano-onions and multiwall nanotubes (Fig. 3.2f). The average distances between successive nanotube walls is 3.4 Å, characteristic for the distance between graphene planes in graphite. The closed structures and small intergraphene distance make the samples not suitable for direct use as hydrogen sorbent. However, this structure appears very often in preparation of carbons precursors used to prepare activated carbons. We expect that these structures can be open, and the graphite layers expanded or exfoliated using an appropriate activation procedure. Therefore, we will not exclude them from the further study.

3.2.2. Adsorption measurements of specific surface area and porosity of as-prepared carbon samples

The initial screening of specific surface area and porosity of carbon samples prepared at different helium pressures was performed using BEL mini apparatus. It allows to measure nitrogen adsorption in the samples at T = 77 K. Isotherms of nitrogen adsorption in two carbon samples, synthetized at 660 and 1100 mbar of helium pressure, are presented on Fig. 3.4. Both isotherms correspond to Ia type isotherm according to IUPAC classification. It means that both samples are mainly microporous.

Table 3.1 summarizes the obtained results. Unfortunately, the specific surface of all samples is low, around 200 m^2/g or below this value. Although the samples' surface monotonically increases when the helium pressure in the reactor is increasing (Fig. 3.5), its value is more than one order of magnitude lower that our target (3000 m^2/g). It is a consequence of presence of many closed structures, not accessible for testing gas.
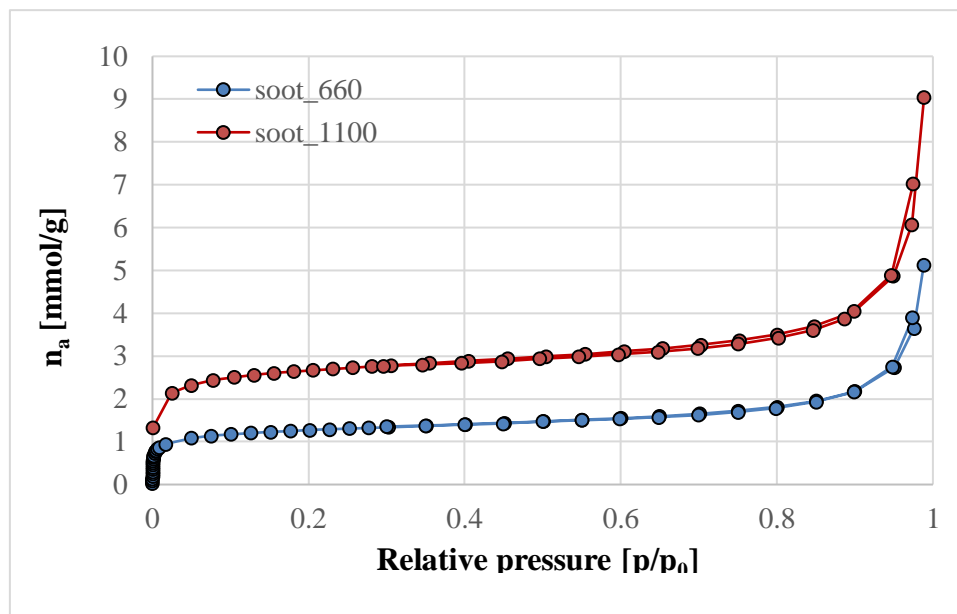
Figure 3.4. Nitrogen adsorption isotherms for two carbon samples, synthetized at 660 and 1100 mbar of helium pressure.

Table 3.1. Specific surface area (SSA), total pore volume V_p (determined at relative pressure $P/P_0 = 0.985$), and micropores' volume (V_{micro}) of carbon samples prepared at different helium pressures. The saturation pressure of nitrogen at $T = 77$ K is equal $P_0 = 0.76$ bar.

pressure [mbar]	SSA [m^2/g]	V_p [cm^3/g]	V_{micro} [cm^3/g]
660	103	0.17	0.03
720	171	0.21	0.06
760	207	0.30	0.07
810	141	0.19	0.04
860	189	0.26	0.07
910	188	0.27	0.06
960	213	0.27	0.08
1030	210	0.31	0.11
1100	221	0.31	0.13

The same conclusion comes from the analysis of samples' pore volumes. The microporous volume was calculated using t-plot method described in Chapter 2. It slightly increases with applied helium pressure (Table 3.1). Microporosity constitutes 1/3 of the total pore volume. Since carbon powder is not mesoporous, we attribute the remaining 2/3 of porosity to the voids between powder agglomerates. However, the hysteresis between adsorption-desorption cycles that is characteristic for isotherms of samples with interparticular porosity (type IIb isotherm according to IUPAC classification) is not very pronounced (Fig. 3.3).

As the sample are strongly heterogeneous (see Fig. 3.3), the average radius of the pores is difficult to determine. On the sample fragment presented on Fig. 3.3 the averaged pore width is equal ~ 5.6 Å. When the helium pressure increases, the specific surface area of the samples monotonically increases (by a factor of 2 between 660 and 1100 mbar). Therefore, for the syntheses of boron-substituted carbon samples we have chosen to operate at the higher experimentally possible helium pressure (slightly over 1 bar), to maximize the initial sample surface and its microporous volume.
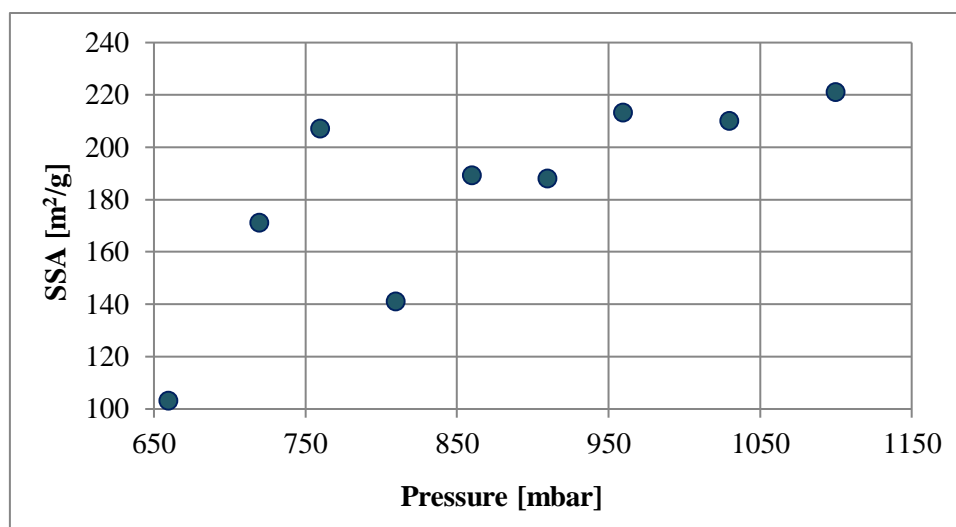
Figure 3.5. Specific surface area SSA of carbon samples in a function of helium pressure maintained in the reactor during the synthesis.

3.3. Activation of carbon samples

Microporosity of carbon samples could be increased by either physical (thermal) or chemical activation.

During physical activation a part of carbon atoms is removed from the structure by gasifying agents such as carbon dioxide, water steam or oxygen. Partial gasification of carbons precursors is usually carried out at 800-1000 $^\circ$C. The activation of samples with CO_2 or H_2O must be carried out in oxygen-free atmosphere: the reaction of O_2 with carbon is highly exothermic and that can prevent the combustion reaction with gasifing medium. On the other hand, controlled carbon oxidation at low oxygen partial pressures and at temperatures up to 600 $^\circ$C leads to the formation of carbon dioxide and removal of available carbon atoms.

Chemical activation is usually conducted in three steps. First, the raw carbon material is impregnated with chemical reactants, basic or acid (H_3PO_4 [3.4], $ZnCl_2$ [3.5], KOH or K_2CO_3 [3.6]), then the sample carbonization is carried out under a flow of inert gas (usually nitrogen). In the case of activation with KOH (the most frequently used), the activation process consists in the reduction of the potassium hydroxide to free potassium metal, penetration of metal atoms into the carbon graphite-like structure, its expansion by the intercalated potassium, and the rapid removal of the intercalate from the carbon matrix. The resulting carbon sample is finally carefully washed to eliminate the remaining activation chemical and the unwanted activation reaction products.

3.3.1. Physical activation of carbons prepared in electric arc discharge

Thermal activation of carbon samples has been carried out in the ambient atmosphere for variable annealing time and temperature. All presented measurements have been performed on samples from the same batch. Their initial specific surface was low, of the order of 270 m^2/g. The initial mass of sample submitted to activation procedure was 200 mg. The activation temperatures have been chosen following the conclusions of the paper by Geng et al. [3.7], where thermal treatment under air atmosphere in 400 °C has been found to be optimal to open closed single-wall carbon nanotubes.

Two activation protocols have been tested. In the first one the sample has been progressively heated to 400 °C (with a temperature ramp 120 °C/hour), annealed at 400 °C for 1 hour, and then cooled down to room temperature. The specific surface area of the activated samples was then measured. This activation procedure was repeated 3 times. In such way the final samples were annealed at 400 °C for 4 hours in total. The second protocol consisted in heating of the sample to the temperature of 300, 350, 400, 450 and 500 °C (with the same temperature ramp of 120 °C/hour), and then annealing the sample at these temperatures for 4 hours.

Fig. 4.6a shows the relative mass loss of sample activated at T = 400 °C using the first activation protocol. The mass of sample was measured after each annealing step and plotted in a function of annealing time. The loss of mass, of the order of 25 % after the first hour of annealing, progressively decreases and become negligible (at the level of experimental error) after 4 hours of annealing. Therefore, we consider that the sample thermal activation at T= 400 °C due to carbon erosion by oxygen is completed after 4 hours.

The specific surface (Fig. 3.6b) increases exponentially with heating time and reaches the maximum (total SSA = 986 m^2/g, where micropore area occupies 890.2 m^2/g and 0.40 cm^3/g of volume) after 3 hours of annealing. Further annealing causes a slight decrease of the surface. This effect can be a result of a partial oxidation and formation of carbonyl and lactone groups on the carbon surface. These reactions are in competition with graphene layers consumption and production of CO and CO_2 gases. If the oxygen complexes' concentration is too high, the graphene combustion slows down and eventually stops [3.15].
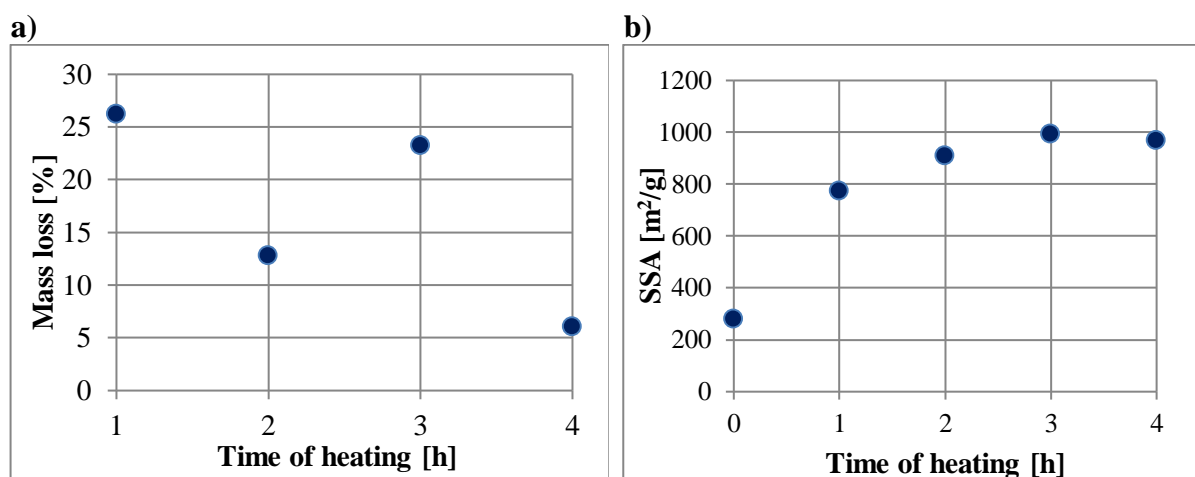
Figure 3.6. a) relative change of mass and b) evolution of specific surface (SSA) of sample annealed at T = 400 °C, as a function of annealing time.

Fig. 3.7 shows the relative mass loss and evolution of specific surface of samples activated using the second activation protocol, and the activation temperatures of 300, 350, 400, 450, and 500 °C. The loss of sample mass increases almost linearly with the annealing temperature. This result agrees also with previous study of Balden et al., carried out on different carbon materials but also finely grained graphite [3.14]. When the samples are annealed at temperatures different than 400 °C (lower or higher), the final specific surface is always lower than that reached at 400 °C (Fig. 3.7b). As it was stated above, this can be due to partial oxidation of carbon surfaces, the reaction that occurs faster at higher temperatures. In fact, the presence of a certain amount of CO bonds on the carbon surface is necessary for combustion reaction and CO and CO_2 gas production to occur [3.15]. However, according to Walker [3.15] and our results presented above, sufficient number of the chemisorbed species appears already at 400°C, which results in the highest SSA (Fig. 3.7b dashed red line). In temperatures close to 600 °C, spontaneous ignition of soot can have place, and this can result in structural changes and successive decrease of SSA for temperatures higher than 400 °C.

Fig. 3.8 summarizes the results obtained using different thermal activation protocols. The highest specific surface was obtained by heating samples during 4 hours in 400 °C at the ambient atmosphere.
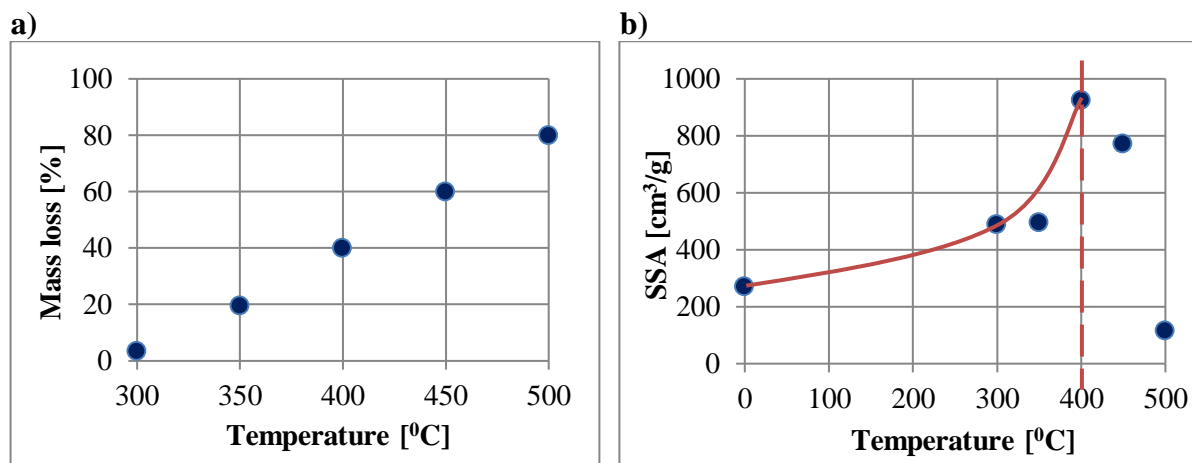
a)

b)

Figure 3.7. (a) the relative mass loss and (b) evolution of specific surface of samples activated for 4 hours at the activation temperatures of 300, 350, 400, 450, and 500 °C. On the Fig. 3.7b, solid red line shows the increase of SSA and dashed line shows the highest SSA obtained for 400 °C.
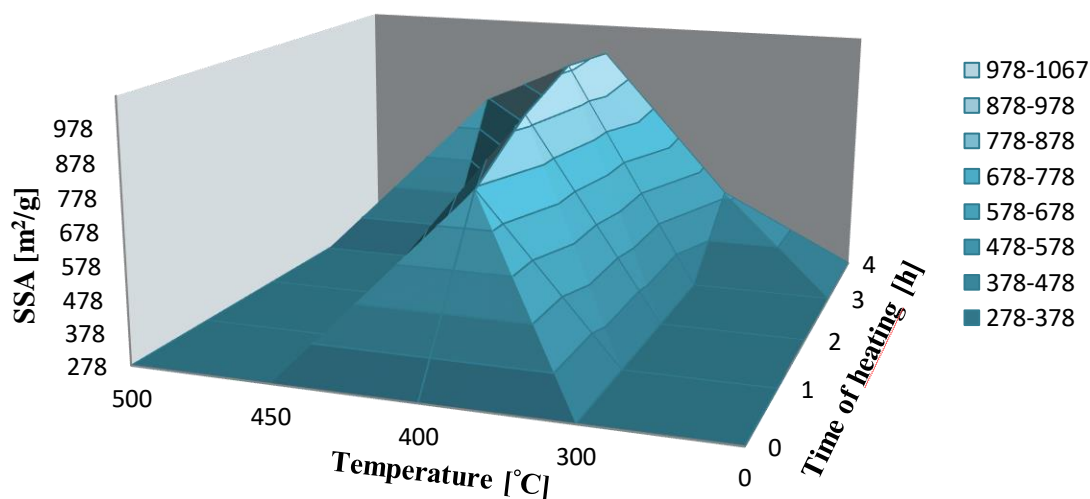
Figure 3.8. The evolution of sample specific surface during thermal activation.

The morphology of the sample showing the highest specific surface area was further analysed using HRTEM and EELS methods. Fig. 3.9 compares the HRTEM images of carbon sample before and after activation. The as-prepared carbons consist in interconnected agglomerated of various shapes, whereas the annealed carbon structures are almost spherical

and well separated. We anticipate that this feature will lead to the increase of sample porosity, at least of its interparticle part.
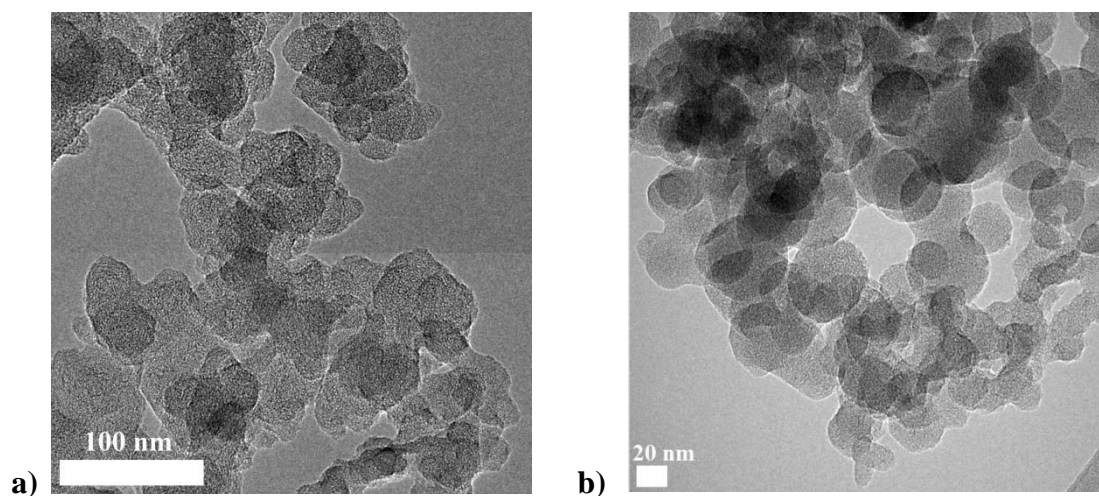
Figure 3.9. HRTEM images of carbon sample a) before and b) after thermal activation at 400 $^\circ$C during 4 hours.

Fig. 3.10 compares the K-edge EELS spectra of the thermally activated sample with the highest SSA and the litterature results of Chen et al. [3.8], observed for some of typical carbonaceous materials.

The peaks, located around in the 280-285 eV and 290-295 eV correspond to electron transitions from the 1s orbital to antibonding π^* and σ^* states, respectively. The peaks are broad, especially the one related to the $1s \rightarrow \sigma^*$ transition. It confirms that the major part of the sample is amorphous. However, the appearance of a relatively narrow π^* peak confirms the presence of sp^2 hybridized carbons, then, crystaline graphitic layers. Our spectra agree with litterature data published by Chen, and confirm our conclusion that thermally activated carbon powders prepared by electric arc discharge contain graphitic layers (brown signal on the left panelof Fig. 3.10, curves a,b, and c on the right panel) and amorphous carbon films (blue signal on the left panel, curve d on the right panel).
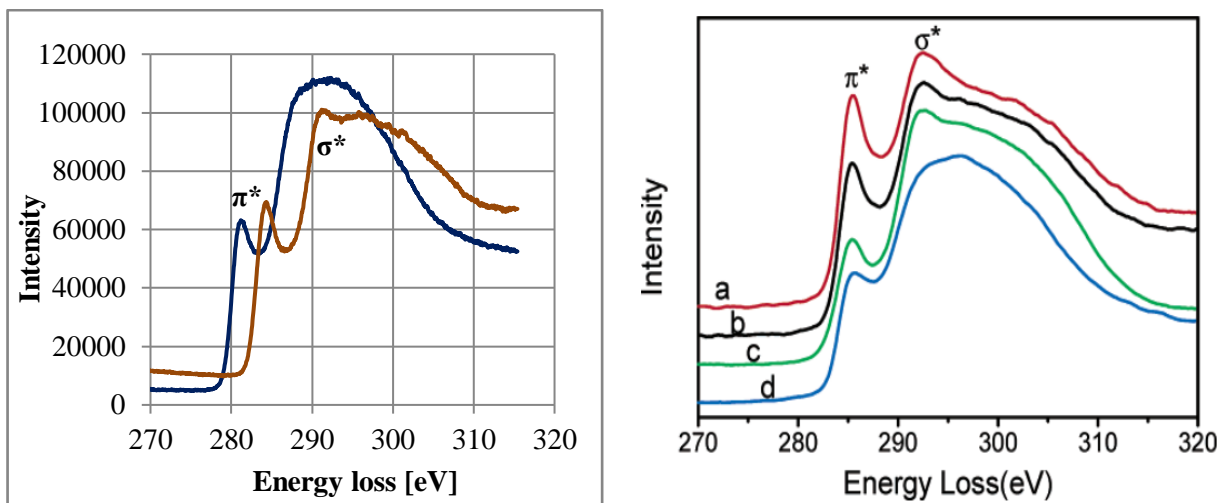
Figure 3.10. (left) K-edge EELS spectra of thermally activated carbon sample showing SSA=989 m^2/g. Blue and brown lines have been obtained on from different parts of the samples. (right) K-edge EELS spectra reported by Chen [3.8] for: a) char particles with graphitic layers mostly parallel to the electron beam, (b) carbon soot aggregates with randomly oriented graphitic layers, (c) char particles with graphitic layers mostly normal to the electron beam, and (d) TEM grid amorphous carbon films.

3.3.2. Chemical activation of carbons prepared in electric arc discharge

To further increase the specific surface, the annealed samples were additionally chemically activated using KOH as activation agent. We followed the activation procedure developed by Romanos et al. [3.6]. It allowed in the past the activation of corn cob derived carbons showing the specific surface of ~3000 m^2/g, higher than that of ideal infinite graphene layer (~2600 m^2/g) [3.9].

Two ways of chemical activation with KOH have been tested: using solid KOH mixed with carbon powder and using liquid KOH solution. In the first case, activated soot was mixed with KOH pellets at the weight ratio 1:3. For activation with liquid KOH, the carbon soot was also mixed with KOH pellets, but a small amount of water was added to create a suspension with high base concentration, and to insure more homogeneous KOH penetration into the sample. In both cases 200 mg of carbon powder was mixed with activation agent, putted into quartz crucible and annealed at 800 °C under nitrogen flow (500 ml/min) for 2 hours. After activation the sample was allowed to cool down, washed with distilled water until pH = 7 was reached, and the remaining material was dried at 120 °C in the oven to remove moisture.

During the activation with solid KOH the sample lost ~45 % of its initial mass. When activated with liquid KOH, the mass loss was slightly larger, ~57 % of initial value.

The chemical reactions occurring during activation below 700 °C consist in progressive oxidation of carbon materials to CO and CO_2, according to the following formulas:

$$2KOH \rightarrow K_2O + H_2O \qquad (1)$$
$$C + H_2O \rightarrow CO + H_2 \qquad (2)$$
$$CO + H_2O \rightarrow CO_2 + H_2 \qquad (3)$$
$$CO_2 + K_2O \rightarrow K_2CO_3 \qquad (4)$$
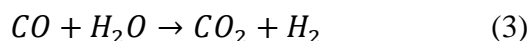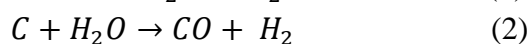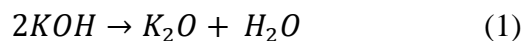
The main activation reactions products are potassium oxide, potassium carbonate, carbon oxides, hydrogen and water [3.10]. When the activation is conducted at temperatures above 700 °C, metallic potassium is formed by the reduction of K_2O by carbon or hydrogen:

$$K_2O + H_2 \rightarrow 2K + H_2O \qquad (5)$$
$$K_2O + C \rightarrow 2K + CO \qquad (6)$$
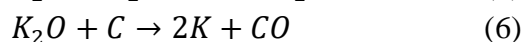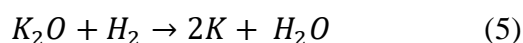
According to Otowa [3.10], at 700 °C the potassium atoms are mobile and can intercalate carbon matrix. It causes the expansion of graphite structure and formation of nanopores.

The porosity and specific surface of KOH-activated samples were determined using nitrogen adsorption measurements. The obtained results are presented in Table 3.2.

Table 3.2. Specific surface and micropore volume of chemically activated samples, determined from nitrogen adsorption isotherms. The data for the samples activated with solid and liquid KOH are compared.

	SSA [m^2/g]	External surface [m^2/g]	Micropore area [m^2/g]	Micropore volume [cm^3/g]
solid KOH activation	790	76	710	0.35
liquid KOH activation	695	106	590	0.25

For both activation procedures the final specific surface areas are small (700 - 800 m^2/g), of the same order of magnitude or smaller than the surfaces of thermally activated carbons. This result is disappointing, especially if compared with the activation results reported by Romanos [3.6]. Usually, the same activation lead to much higher specific surfaces (SSA = 1283 m^2/g for carbon spheres made of glucose [3.11], SSA =1500 m^2/g for biochar [3.12], SSA = 2500 m^2/g

for corncob derived carbons [3.6], or SSA = 2800 m^2/g for fire wood carbons [3.13]). According to Table 3.2, slightly better results were obtained for carbon activated by solid KOH than by liquid KOH, with 90% of porosity provided by system of micropores that occupies the volume of 0.35 cm^3/g. Activation reaction with liquid base is supposed to provide better distribution of the compound inside the carbon powder, however, the obtained porosity is low: 695 m^2/g of specific surface and 0.25 cm^3/g of micropore volume.

3.4. Bibliography

[3.1] Ahmed-Azmi Zahab, *Synthese, carcterization et etude physique des fullerenes C60 et C70 et de leurs derives*, PhD thesis, Montpellier, France, 1992

[3.2] C. Journet, P. Bernier, *Production of carbon nanotubes*, Appl. Phys. A 67, 1-9 (1998)

[3.3] A. B. Belgacem, I. Hinkov, S. B. Yahia, O. Brinza, S. Farhat, *Arc discharge boron nitrogen doping of carbon nanotubes*, Materials Today Communications 8 (2016) 183-195

[3.4] J. Hayashi, A. Kazehaya, K. Muroyama, A. P. Watkinson, *Preparation of activated carbon from lignin by chemical activation*, Carbon 38 (2000) 1873–1878

[3.5] M. Molina-Sabio, F. Rodrıguez-Reinoso, *Role of chemical activation in the development of carbon porosity*, Colloids and Surfaces A: Physicochem. Eng. Aspects 241 (2004) 15–25

[3.6] J. Romanos, M. Beckner, T. Rash, L. Firlej, B. Kuchta, P. Yu, G. Suppes, C. Wexler, P. Pfeifer, *Nanospace engineering of KOH activated carbon*, Nanotechnology 23 (2012) 015401

[3.7] H.Z. Geng, X.B. Zhang, S.H. Mao, A. Kleinhammes, H. Shimoda, Y. Wu, O. Zhou, *Opening and closing of single-wall carbon nanotubes*, Chemical Physics Letters 399 (2004) 109–113

[3.8] Y. Chen, N. Shah, F. E. Huggins, G. P. Huffman, *Investigation of the Microcharacteristics of PM2.5 in Residual Oil Fly Ash by Analytical Transmission Electron Microscopy*, Environ. Sci. Technol., 38 (24), 2004, 6553–6560

[3.9] M. A. Lillo-Ródenas, D. Cazorls-Amorós, A. Linares-Solano, *Understanding chemical reactions between carbons and NaOH and KOH. An insight into the chemical activation mechanism*, Carbon 41 (2003) 267-275

[3.10] T. Otowa, Y. Nojima, T. Miyazaki, *Development of KOH activated high surface area carbon and its application to drinking water purification*, Carbon 35 (1997) 1315-1319

[3.11] M. Li, W. Li, S. Liu, *Hydrothermal synthesis, characterization, and KOH activation of carbon spheres from glucose*, Carbohydrate Research 346 (2011) 999–1004

[3.12] R. Azargohar, A.K. Dalai, *Steam and KOH activation of biochar: Experimental and modeling studies*, Microporous and Mesoporous Materials 110 (2008) 413–421

[3.13] F. Wu, R. Tseng, R. Juang, *Preparation of highly microporous carbons from fir wood by KOH activation for adsorption of dyes and phenols from water*, Separation and Purification Technology 47 (2005) 10–19

[3.14] M. Balden, K.U. Klages, W. Jacob, J. Roth, *Oxidative erosion of graphite in air between 600 and 1000 K*, Journal of Nuclear Materials 341 (2005) 31–44

[3.15] P. L. Walker, R. L. Taylor, J. M. Ranish, *An update on the carbon-oxygen reaction*, Carbon Vol. 29. No. 3. pp. 411-421. 1991

CHAPTER 4

Characterisation of adsorptive properties of nanoporous boron-carbon samples prepared by arc discharge procedure

Perfect carbon material for hydrogen storage should exhibit both: high surface area and high adsorption energy. Although high surface can be obtained by samples' activation, the adsorption energy can be increased only by material's structural modification. Introduction of heteroatoms in carbon structures (by doping or substitution) results in structural and energetic heterogeneity and may create additional sites strongly attracting hydrogen. Grand Canonical Monte Carlo simulations [4.1] suggested that substitution of a part of carbon atoms in graphene honeycomb structure by boron can significantly increase the energy of hydrogen adsorption in infinite graphene slit pores. Fig. 4.1 shows the energy landscapes for H_2 adsorption on BC_n graphene-based surface. This landscape (and the resulting average adsorption energy) changes dramatically in a function of the ratio of boron substitution (Fig. 4.1). For 10 % substitution ratio the average adsorption energy of hydrogen reaches the value of 9.56 kJ/mol, very promising for potential hydrogen storage at room temperature and relatively low pressure.
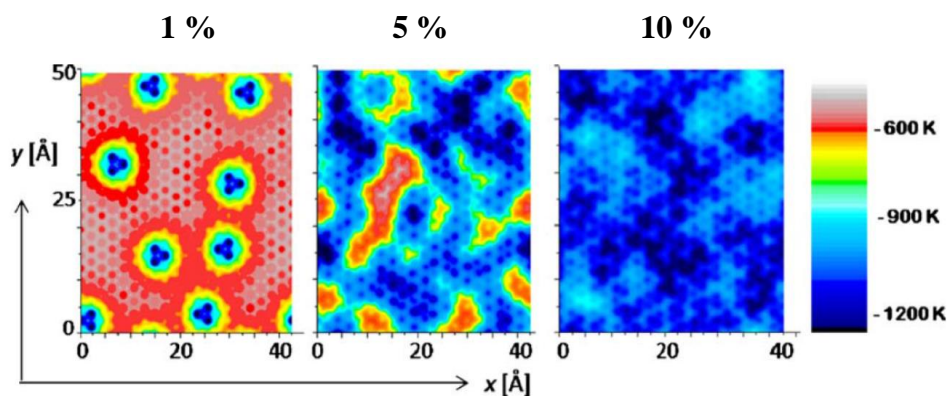
Figure 4.1. Heterogeneity of the energy landscape for H_2 adsorbed on a single graphene surface randomly substituted with 1% (E_{aver} = -650 K= -5.40 kJ/mol) (left), 5% (E_{aver} = -900 K= -7.48 kJ/mol) (centre) and 10% (E_{aver} = -1150 K= -9.56 kJ/mol) (right) boron atoms [4.1].

Therefore, to verify the theoretical calculations cited above, we prepared (using electric arc discharge technique) and analysed boron-substituted carbon structures with different boron concentrations.

4.1. Synthesis of boron-substituted carbon samples

To synthesize the boron-substituted carbons we have initially used the same electric arc discharge parameters (electric current, inert gas pressure) as those that we have already optimized for the synthesis of pure carbon samples (see chapter 3). However, as boron is an insulator, it was more difficult to create and maintain a continuous electric arc discharge between the graphitic cathode and boron-filled anode within these conditions. Therefore, we increased the pressure of helium inside the reactor from 600 mbar up to 800 mbar. It allowed to increase the number of charge carriers in the reactor and to maintain an electrical connection between electrodes (even if, simultaneously, the difference of potential between the electrodes dropped from 50 V to 30 V). We collected and analysed only the soot part of the material. In such a way four boron-substituted carbon samples with boron concentrations of 23.3 wt.% B, 19.9 wt.% B, 11.3 wt.% B, 5.3 wt.% B were synthetized and characterized. The boron content has been estimated according the procedure described in Chapter 2.2.

4.2. Characterization of boron-substituted carbons

4.2.1. Morphology of boron-substituted carbon powders

The morphology of boron containing carbon samples can be partially predicted by boron-carbon phase diagram (Fig. 4.2.). Thermodynamic conditions inside the reactor chamber during synthesis (T~4000 °C) can lead to creation of boron carbide/boron nanoparticles. Furthermore, Figure 4.2 shows, that for boron concentration lower than 25% does not guarantee the absence of such nanocrystals. According to this reference, we have probability to obtain locally both: (i) carbon doped boron regions and (ii) boron doped carbon regions.
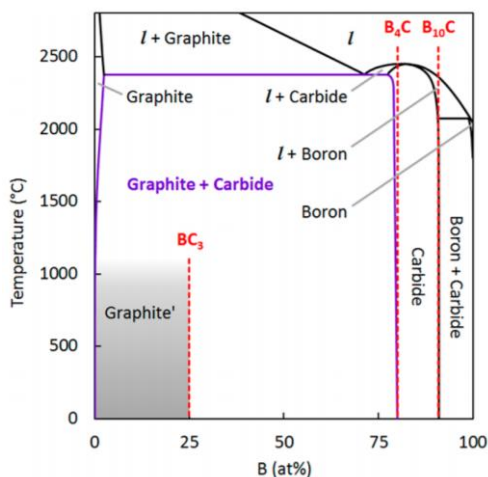

Figure 4.2. Boron−carbon binary phase diagram, at ambient pressure, comprising the following distinct phases: graphite (Graphite), boron carbide (Carbide), β-rhombohedral boron (Boron), and liquid (ι). Metastable, boron-doped graphitic carbon is also shown (Graphite) [4.2].

The morphology of as prepared boron containing carbon samples was first analysed using microscopic (SEM, HRTEM) and spectroscopic (EELS) methods.

4.2.1.1. Microscopic analysis of boron-substituted carbons

Fig. 4.3 shows the SEM images of the sample with the lowest boron concentration (5.3 wt.%). Different sample regions have similar, amorphous aspect with pronounced porosity of the nanometric size (Fig. 4.3 a,b). Some more organized, needle-like or tubular structures with the diameter of ~50 nm are also observed (Fig. 4.3 c,d). To get information about the atomic composition of the sample, we performed their EDS analysis. Fig. 4.4 and Fig. 4.5 show the relative concentration of different atoms in the samples, marked by different colours.
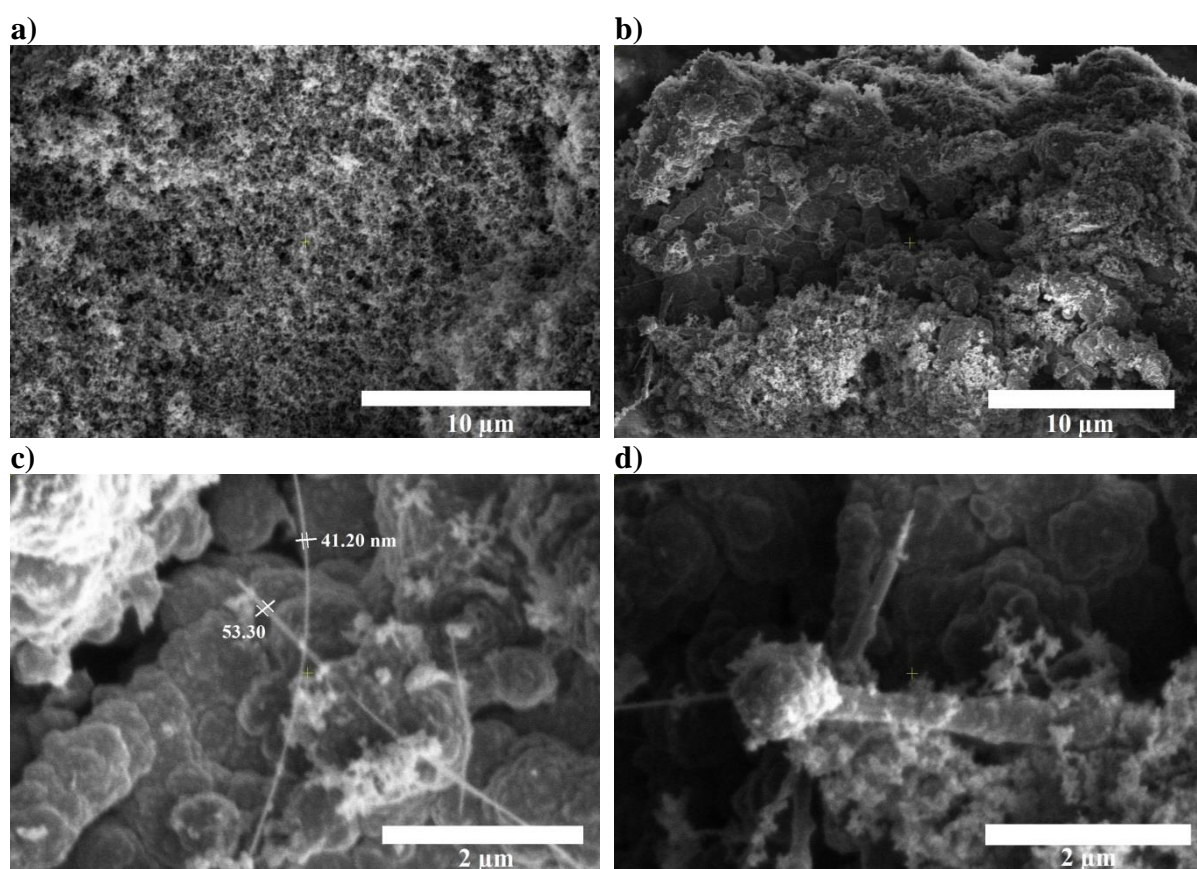
Figure 4.3. SEM images of the sample containing 5.3 wt.% of boron. a,b) representative views of two different regions of the sample, showing the amorphous character of the structure and the porosity on the sub-micrometric scale, c) tubular and d) needle-like structures of ~50 nm of diameter.
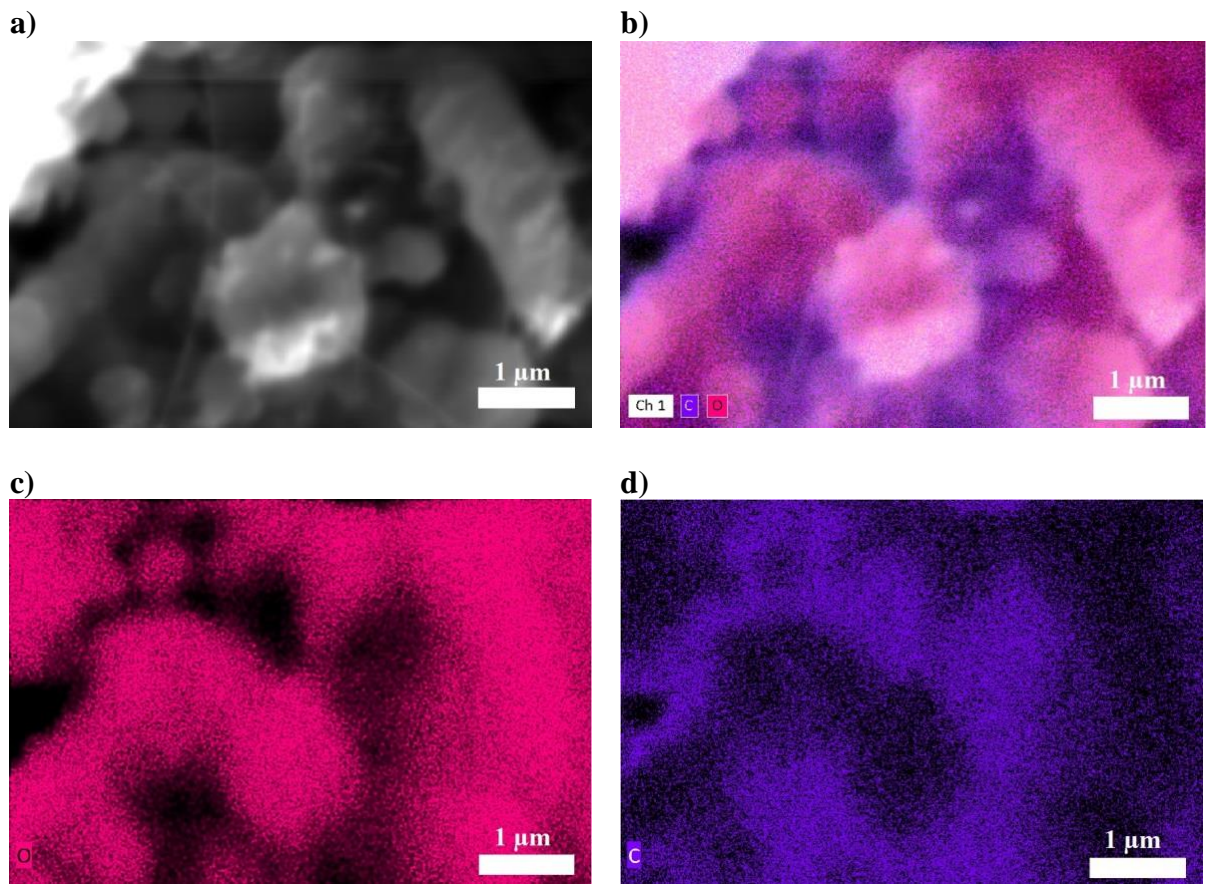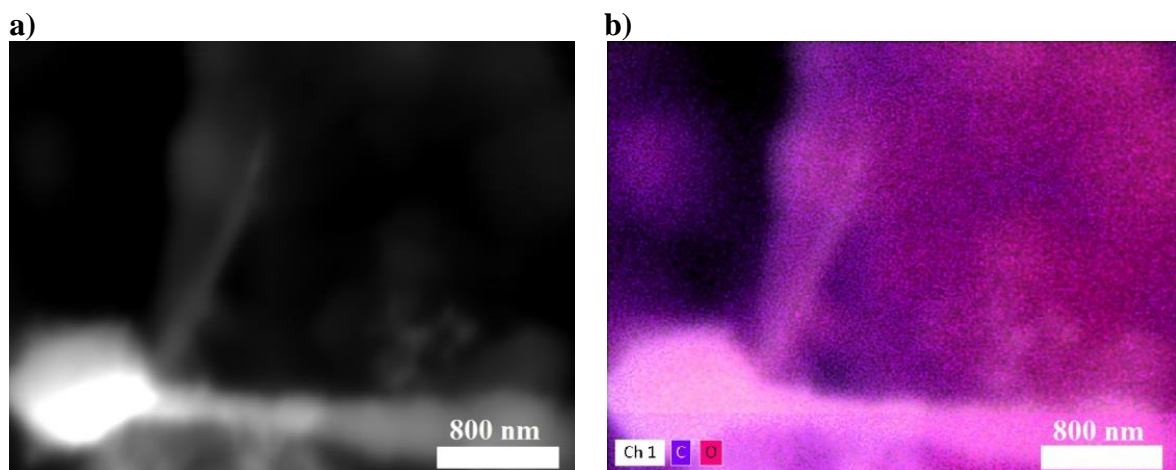
Figure 4.4. Atomic composition of sample containing 5.3 wt.% of boron. a) SEM image of the analysed sample fragment, b) atomic composition (C and O detected), c, d) separated signals from oxygen and carbon atoms, respectively.
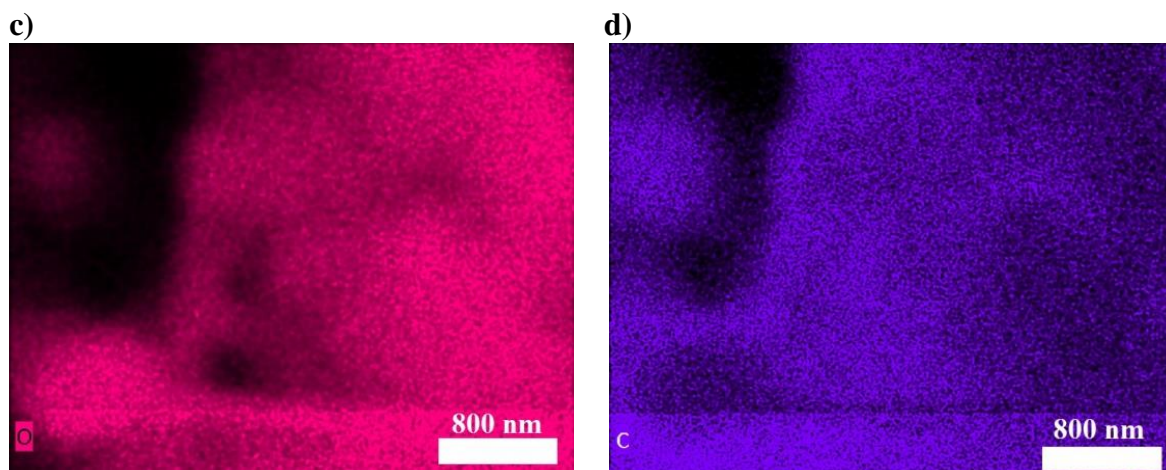
Figure 4.5. Atomic composition of sample containing 5.3 wt.% of boron. a) SEM image of the sample fragment from Fig. 4.3d containing needle-like structure, b) atomic composition (C and O detected), c, d) separated signals from oxygen and carbon atoms, respectively.

The analysed sample fragments contain mainly carbon and oxygen, in the relative proportion 65% of carbon atoms, and ~35% of oxygen atoms. The oxygen seems to be localized mostly on the edges of carbon structures, probably as a part of lactone and/or carbonyl groups. These groups are usually formed when the nanocarbons are exposed to air. In our case, as we stored the samples at ambient conditions, the amount of surface group is important.

It is difficult to distinguish by EDS the simultaneous presence of boron and carbon atoms. In fact, in both atoms the differences of energies between the higher-energy electron shells (L) and lower-energy electron shells (K) (called K_α transitions) are similar: 0.183 keV and 0.277 keV for boron and carbon, respectively. In addition, as the analysed sample contain a small amount (5.3 wt.%) of boron, the signal to be detected is supposed of low intensity. Therefore, to verify if the boron atoms are incorporated as expected into the carbon structures, we have used HRTEM and EELS spectroscopy methods.

The morphology of samples containing boron is different than that of pure carbon samples. Many well-ordered, closed structures are observed together with amorphous carbon: nano-onions, nanotubes, and nanocrystallites (Fig. 4.6 a,c). According to EELS spectroscpy (Fig. 4.6 b,d), boron forms nanoclusters with diameters up to 20 nm within carbon structures. We have noted that very often boron concentration is higher in the vicinity of structured carbon fragments (see for example Fig. 4.6 c,d where high boron concentration is observed close to the 'knee' of the folded natnotube). We suppose that it could result from a competition between
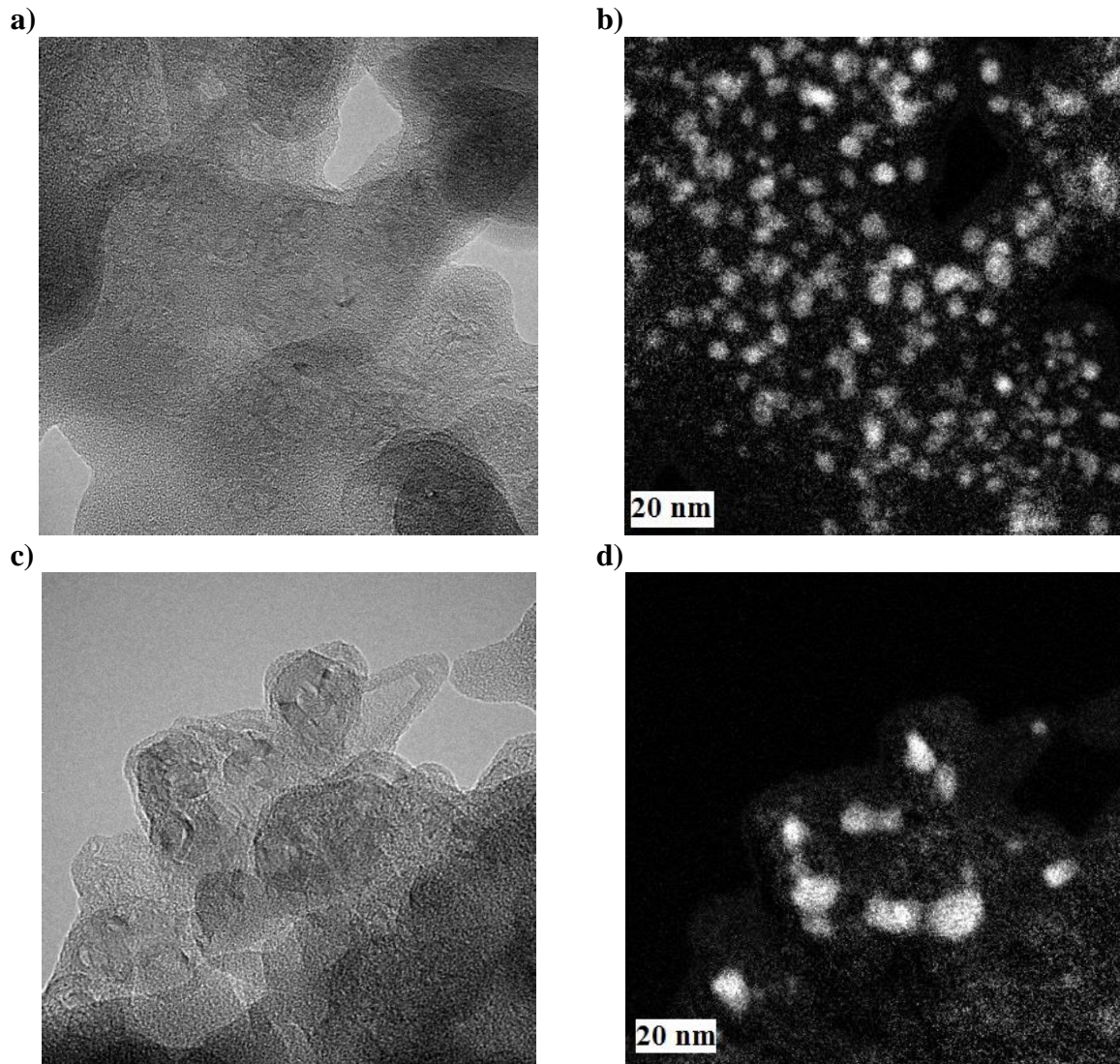
Figure 4.6. HRTEM and EELS spectroscopy images of sample with 5.3 wt.% of boron. We shows the HRTEM images (left column) of two different fragments of the same sample, and the corresponding EELS images (right column). The bright spots denote the presence of boron atoms.

carbon and boron to minimize the energy of formed structures. Accoridng to boron-carbon phase diagram (Fig. 4.2), both graphite and boron-carbide structure may be formed when the carbon concentration in the initial boron–carbon mixture is higher than 20%. As in our case the carbon content is higher than 70%, we should expect a large amount of graphite based structures in our samples. In fact, HRTEM pictures (Fig. 4.6 c,d) show both phases: boron-like domains and graphitized carbon, additionally sourounded by amorphous carbon.
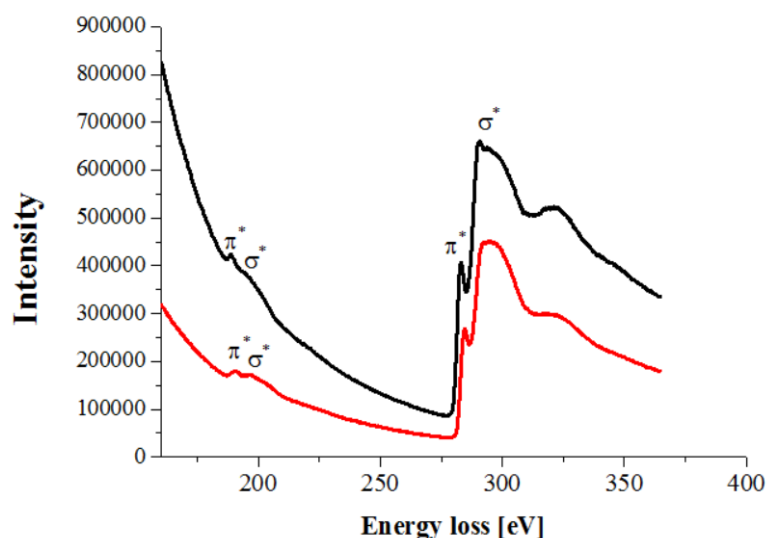
Figure 4.7. EELS spectrum of sample with 5.3 wt.% of boron for two different sample regions. The boron K-edge is located arround 190 eV; this of carbon arround 284 eV.

Figure 4.7 shows the EELS spectrum of a boron–containing sample with 5.3 wt.% of boron, in a function of energy loss. The EELS technique is sensitive to the local environment of the excited atoms, and in particular, to the projected density of unoccupied states close to Fermi level [4.3]. The peaks appearing around 290 eV correspond to $1s \rightarrow \pi^*$ and $1s \rightarrow \sigma^*$ transition within carbon and are characteristic for sp^2 and sp^3 hybridized carbon [4.4, 4.5]. The signals' relative intensity indicates that the sample contains more sp^3 hybridized carbons than sp^2 carbons, typical for graphitized structures. This result can have two different origins. First of all, it can indicate that the sample contains a large amount of non-graphitized (amorphous) structures and defects; the last ones are necessary to create closed structures (like nanotubes or nano-onions), actually observed in the sample. At the same time, as the atomic radius of boron is larger than that of carbon, its incorporation of graphitic honey comb arrangement causes distortion of the planar graphene layer [4.6] and may increase the part of sp^3 carbon hybridization in EELS spectrum.

Similarly, the two peaks appearing around 190 eV are attributed to $1s \rightarrow \pi^*$ and $1s \rightarrow \sigma^*$ transitions within boron. According to Arenal et al. [4.7], the spectrum of bulk boron consists of only one broad peak located around 200 eV. The appearance of fine structure of this peak suggests that local environment of boron atoms in the sample is not homogeneous.

4.2.1.2. Pore size distribution from nitrogen adsorption measurement

Porosity of all boron-containing carbon samples was determined from nitrogen adsorption measurements at 77 K. For all samples, the isotherms of N_2 adsorption (Fig. 4.8) are of type IIb according to IUPAC classification, and are characteristic for microporous solids. For all samples, a narrow hysteresis loops appear at high relative pressures ($p/p_0 > 0.8$). It is attributed to inter-particle capillary condensation.
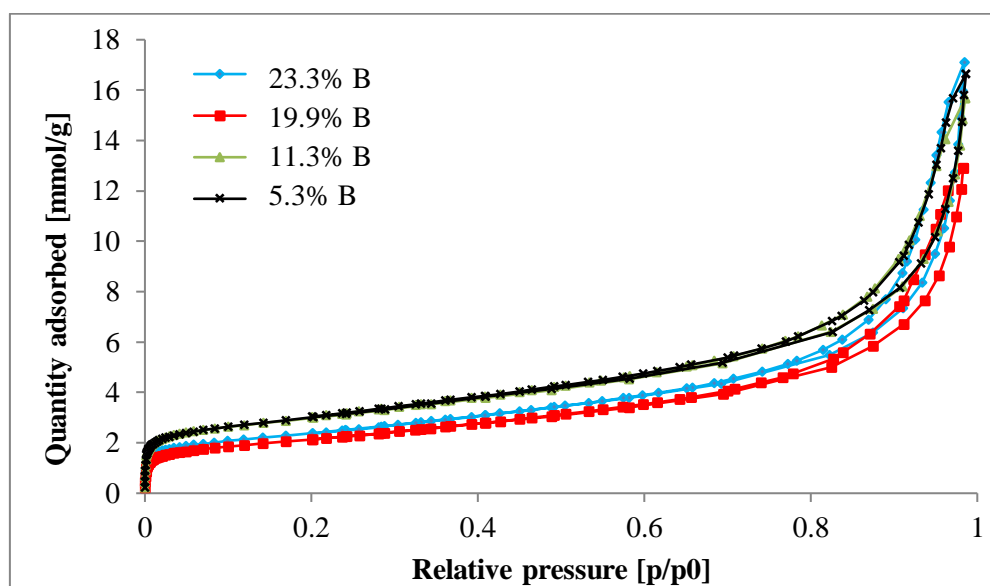

Figure 4.8. Isotherms of boron-carbon samples.

Table 4.1 gives the main characteristics of all samples, extracted from adsorption measurements. The total surface area of all samples is comparable and small, which can be due to morphological similarities of created boron-carbon material. The micropore surface area and micropore volume increase when boron concentration decreases. It is probably due to the presence of boron-like domains in the samples. Such structures are observed already for the sample with the lowest boron content (see Fig. 4.6, sample with 5.3 wt.% of B), and are expected to appear in higher concentration in samples with higher B:C ratio.

Table 4.1 Nitrogen adsorption results obtained in 77 K for boron-carbon samples synthetized in electric arc discharge with different boron concentrations.

Sample	SSA [m²/g]	Ext SA [m²/g]	Micropore area [m²/g]	Micropore volume [cm³/g]
23.3 wt.%B	185	180	5	0.005
19.9 wt.%B	167	160	7	0.005
11.3 wt.%B	217	178	39	0.019
5.3 wt.%B	237	195	42	0.020

74

Figure 4.9 presents pore size distribution for all samples in microporous region (up to 10 Å of the diameter). The estimation of the pore width was carried out using Horvath-Kawazoe method assuming slit-shaped pores' geometry. Sample contains 23.3 wt.% of B and 11.3 wt.% of B have comparable pore size distribution, located between 5 Å and 8 Å. The distributions of pore sizes in samples contain 19.9 wt.% of B and 5.3 wt.% of B are also comparable, located between 5 Å and 7 Å.
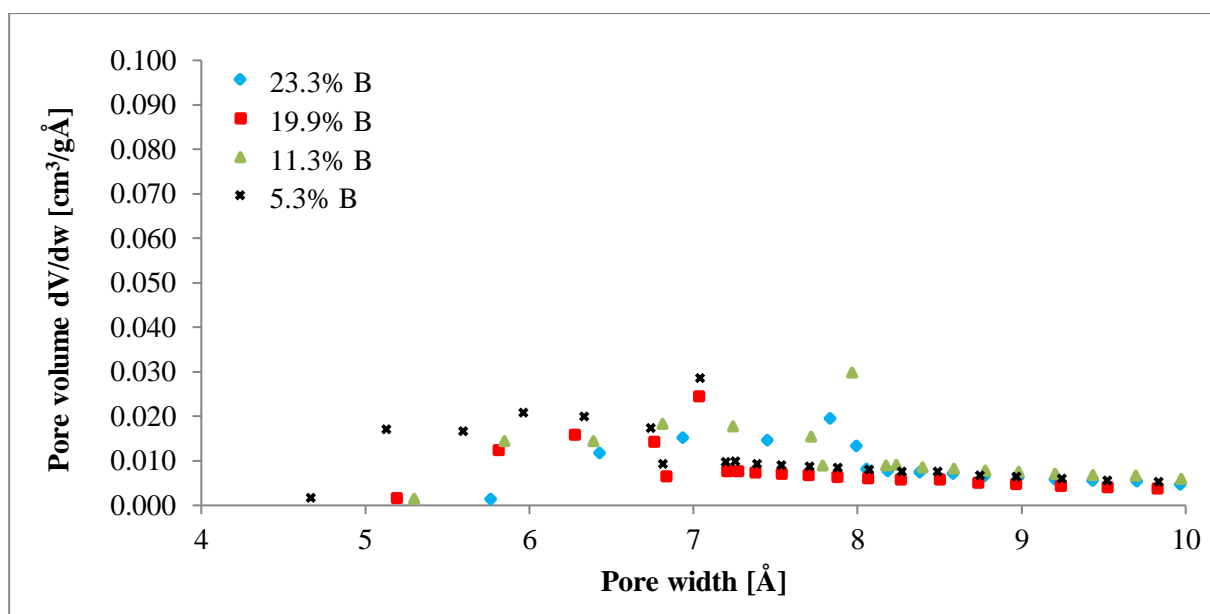

Figure 4.9. Pore volume in boron-carbon samples in a function of pore diameter (up to 10 Å), estimated using Horvath-Kawazoe method and assuming slit shape of pores.

More information about samples' morphology has been obtained from the analysis of NMR spectra.

4.2.1.3. ^{11}B MAS NMR analysis of boron-carbon samples

Boron-carbon samples were additionally analysed by ^{11}B MAS NMR. The goal of this study was to detect the presence of boron-carbon bonds and confirm the substitutional incorporation of boron into graphite structure during the sample synthesis.

Figure 4.10 compares the literature data obtained by Shirasaki et al. [4.4] on boron-substituted carbons containing made by CVD (Chemical Vapour Deposition, 25%, 23% and 13% of boron) with those obtained on boron-carbon samples synthetized by electric-arc discharge method in the present work (23.3 wt.%, 19.9 wt.%, 11.3 wt.% and 5.3 wt.% of boron). The main resonance, appearing at 0 ppm (with respect to bulk [11]B powder reference) can correspond to boron carbide. This signal is supposed to be a combination of homonuclear

boron-boron dipolar interactions (main peak) and chemical shift anisotropy [4.4]. The intensity of this signal corresponds to boron concentration inside the sample which is shown on Fig. 4.10 (left).
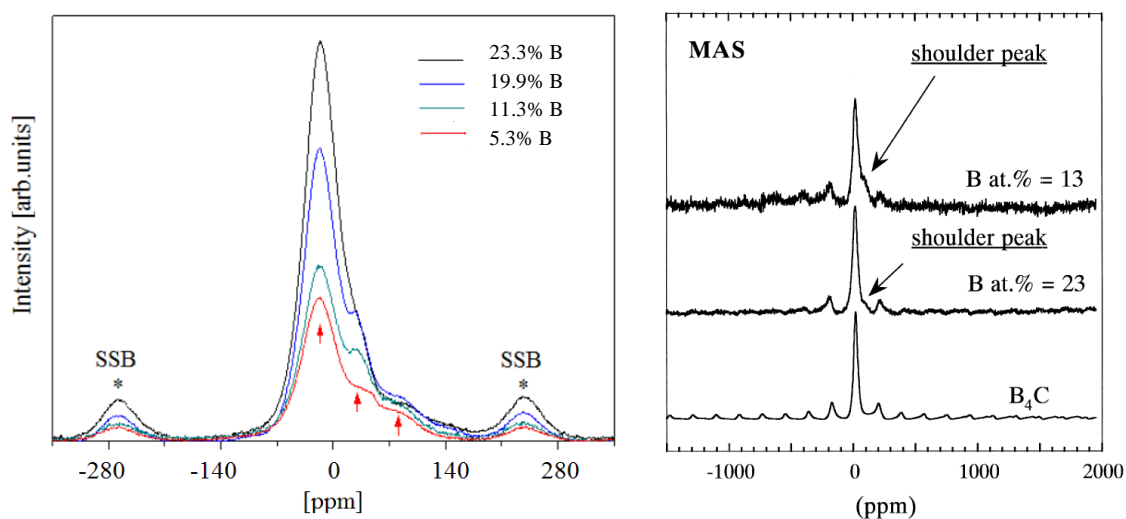

Figure 4.10. ^{11}B MAS NMR spectrum obtained for: (left) boron-carbon samples (23.3 wt.%, 19.9 wt.%, 11.3 wt.% and 5.3 wt.% of B) synthetized by electric arc discharge and (right) boron substituted carbons synthetized by chemical vapour depossition (CVD) [4.4].

According to Shirasaki et al. [4.4] the broadest peak appearing in both types of samples at the shoulder of the main resonance, at 32 ppm is characteristic for second-order carbon-boron quadropular interaction. It indicates the presence of boron atoms chemically bonded to carbons. When the concentration of boron increases, this signal progressively broadens and merge with the main, boron-boron signal disappears. An additional weak signal observed at higher frequency 86 ppm may result from B-B bond at certain local geometry. Similar results for rayon-based carbon fibers doped by boron were published by Wang et al. [4.16] (Figure 4.11). It was reported that according to this spectrum the boron atoms may exist in three different chemical environments including boron carbide, boron clusters and BC_3. Obtained chemical shifts can be correlated to doping or substitution of carbon by boron.

The peaks marked with asterisk * (Fig. 4.10, left) are spinning-side bands of the main resonance. They result from magnetic field modulation at the spinning frequency (f =20 kHz in our case), and always appear when the sample spinning rate is lower than the sample chemical shift anisotropy. The peaks separation is equal to the spinning rate [4.8].
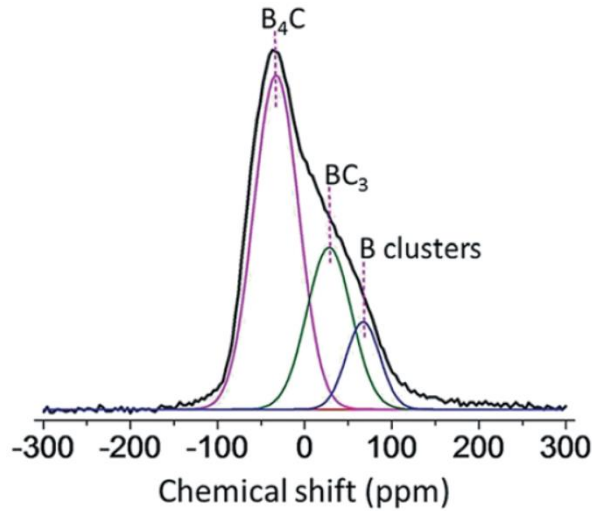
Figure 4.11. MAS 11B NMR spectra observed at 9.39 T for boron-doped RCFs Gaussian lineshapes used for fitting to estimate the intensities of the three signal components: B_4C, BC_3 and B clusters [4.16].

4.2.1.4. Isosteric heat of nitrogen adsorption in boron-carbon

The capacity of boron-containing samples to adsorb hydrogen was evaluated on the sample with the highest boron concentration (23.3 wt.% of B).

First, we have determined the isosteric heat of hydrogen adsorption ΔH at low temperature (77 K). For that, hydrogen adsorption was measured at two temperatures, 77 K and 87 K. The obtained adsorption isotherms for both temperatures have been converted to gravimetric absolute adsorption amount and are shown on Fig. 4.12a. The isosteric heat was then evaluated from the low-pressure part of isotherms, (described by Henry's law, Fig. 4.12b) using Clausius-Clapeyron relation:

$$\Delta H = R \cdot \frac{T_1 T_2}{(T_2 - T_1)} \cdot ln\left(\frac{p_2}{p_1}\right) = R \cdot \frac{T_1 T_2}{(T_2 - T_1)} \cdot ln\left(\frac{k_H(T_1)}{k_H(T_2)}\right) \tag{4.1}$$

where $T_1 = 77$ K, $T_2 = 87$ K. p_1 and p_2 correspond to the pressures at which the same amount of hydrogen is adsorbed at respectively $k_H(T_1)$ *and* $k_H(T_2)$ are the Henry's constants at T_1 and T_2. R is the gas constant (8.314 J/K· mol).
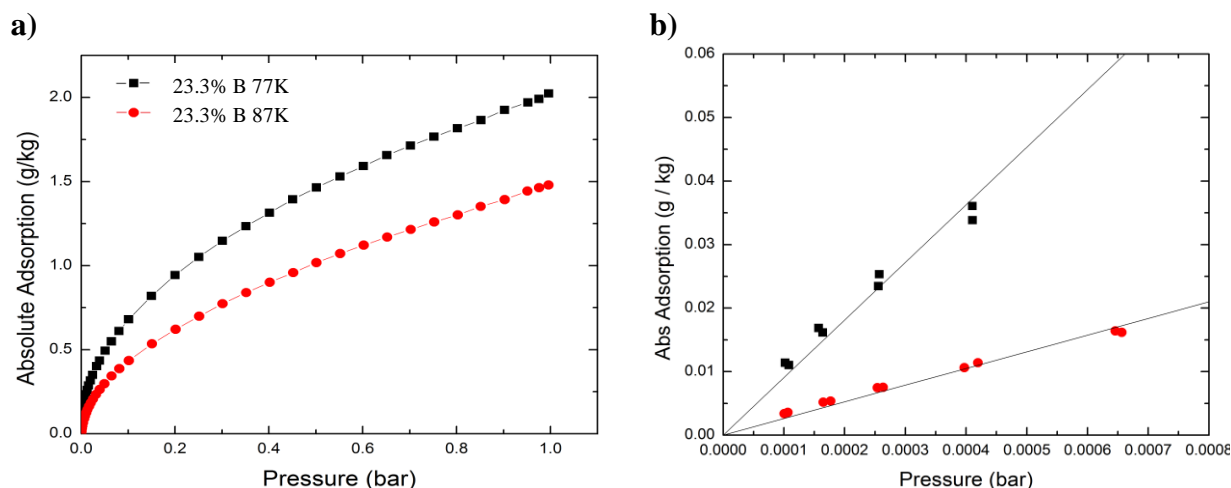
Figure 4.12. a) Isotherms of hydrogen adsorption in soot_1B sample (with the highest boron concentration) at T = 77 K and T = 87 K; b) zoom on the isotherms' low-pressure range. A linear increase of the adsorbed amount with increasing pressure (Henry law) is clearly observed.

The Henry's law constants were estimated from first five pressure points of the isotherms (Fig. 4.12b) according to the Henry's law equation:

$$G_{abs}(p,T) = k_H(T)p \qquad (4.2)$$

where G_{abs} is gravimetric (in g/kg) absolute adsorption at the given pressure and temperature. We found $k_H(77\ K) = 90.0$ g/kg·bar^{-1} and $k_H(87\ K) = 26.3$ g/kg·bar^{-1}. The evaluation of isosteric heat at zero coverage from equation (4.1) gives $\Delta H = 6.9$ kJ/mol. This value is subject to a large uncertainty, mainly because the arbitrary choice on number of pressures that are included into the evaluation of Henry constant. This is illustrated on Fig. 4.13 where the lines used to evaluate Henry constants (from Figure 4.12b) fall badly off the experimental data beyond the first initial pressures.
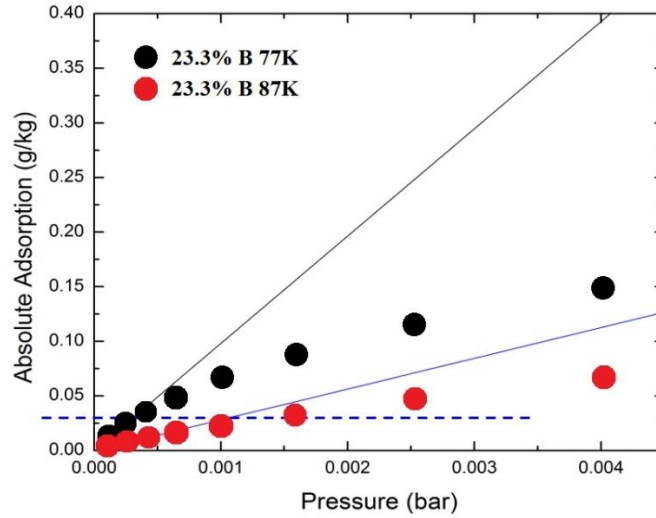
Figure 4.13. Isotherms (T = 77 K and T = 87 K) of hydrogen adsorption in sample with 23.3 wt.% of B. The slope of lines is the same as on Fig. 4.12. The dashed horizontal line corresponds to G_{abs} = 0.03 g/kg, for which isosteric heat of adsorption was determined using Clausius-Clapeyron relation (4.1).

To avoid such an arbitrary estimation of Henry constant, we decided to used virial expansion of Clausius-Clapeyron equation of adsorption isotherm in the limit of zero-coverage:

$$ln\left(\frac{G_{abs}}{p}\right) = K_1 + K_2(G_{abs}) + K_3(G_{abs})^2 + \cdots \qquad (4.3)$$

$$\frac{G_{abs}}{p} = e^{K_1}e^{K_2 G_{abs}} \ldots = e^{K_1} = k_H \quad \text{if} \qquad G_{abs} \to 0 \text{ as } p \to 0. \qquad (4.4)$$

Figure 4.14 presents the graph of $ln\left(\frac{G_{abs}}{p}\right)$ in a function of G_{abs}. The estimated values of virial coefficients K_1 (77 K) = 5.06 g/kg·bar and K_2 (87 K) = 3.65 g/kg·bar were then used to calculate Henry's constants according to formula (4.4): k_H(77 K) = 142 g/kg · bar^{-1} and k_H(87 K) = 28 g/kg · bar^{-1}. These values are larger than the ones determined previously from initial 5 points of the isotherms only. In consequence, the isosteric heat of adsorption at zero coverage, calculated using the new values of Henry's constants is also larger: ΔH = 9.06 kJ/mol. We consider that this value is more accurate than of isosteric heat calculated from Henry's law directly. This value is also the largest value of hydrogen isosteric heat in carbon-based adsorbents ever determined experimentally.
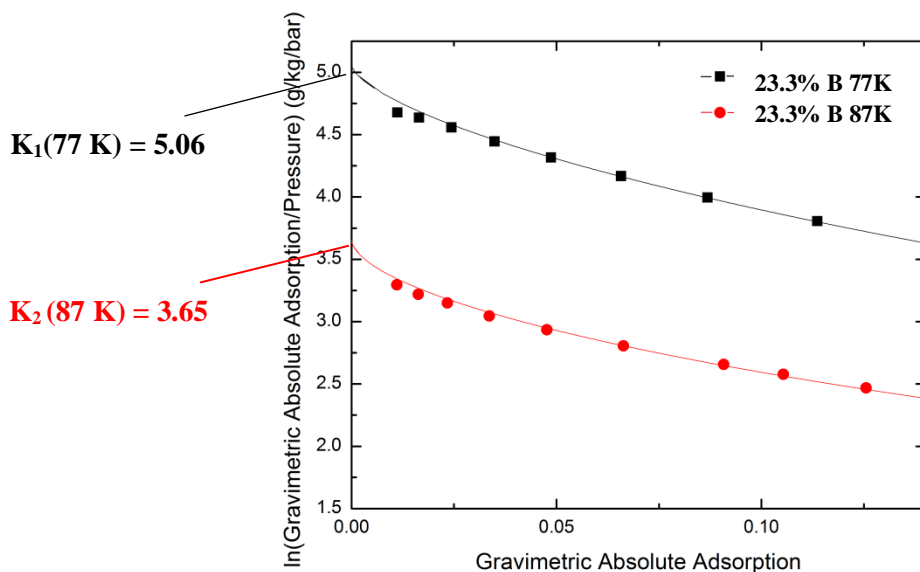
$K_1(77 \text{ K}) = 5.06$

$K_2(87 \text{ K}) = 3.65$

Figure 4.14. Virial expansion of adsorption isotherm for sample contains 23.3 wt.% of B and virial coefficients' determination.

4.3. Activation of boron-carbon samples

To be applicable as adsorbent in hydrogen tanks, boron- carbon material should exhibit high specific surface (~3000 m^2/g). In the case of purely carbon compounds the usual (and sufficient) method to reach such high values is an activation procedure. In the case of boron containing samples the activation procedure should be carried out with specific care. When boron is heated in air to ~700 $^\circ$C, a reaction with oxygen occurs and boron trioxide (III) is formed. Similarly, during chemical activation in ambient conditions boron reacts with KOH and KBO$_3$ is formed. Both reactions create undesirable species and have to be avoid by an adequate choice of activation protocol. Then, as the arc-prepared boron-carbon samples contain also well-ordered, highly stable boron nanostructures that block the pores' entrance (see chapter 4.2.1, Fig. 4.5), the activation procedure (optimized for carbon samples) can be less efficient.

4.3.1. Thermal activation of boron-carbon samples synthetized in electric arc discharge

In the first step we thermally activated boron containing carbon samples according to procedure optimized for purely carbon samples.

4.3.1.1. Procedure of thermal activation

Boron-carbon powders with different boron concentrations were heated inside an oven at ambient atmosphere. The influence of annealing time on the sample's characteristic was

evaluated using the procedure used previously for purely carbon samples (see chapter 3.3.1). Two activation protocols have been tested. The first one was carried out on the sample containing 19.9 wt.% of B and showing the initial specific surface area of 170 m^2/g. It consisted in annealing of 200 mg of the powder at 400 $^\circ$C for 1 hour (the temperature ramp of 120 $^\circ$C/hour was used) and cooling it down to ambient temperature. This procedure was repeated three times to get a cumulative annealing time of 4 hours. Porosity measurement were performed after each activation step.

The second procedure consisted in continuous annealing of the samples in air at 400 $^\circ$C for 4 hours, with the same temperature ramp. This procedure was applied to all remaining boron-substituted carbon samples: 23.3 wt.% of B, 11.3 wt.% of B, and 5.3 wt.% of B in raw.

4.3.1.2. Determination of porosity of thermally activated boron-containing carbon samples

Porosity of thermally activated boron-containing carbon samples was evaluated from nitrogen adsorption isotherm, measured at 77 K. Fig. 4.15 shows the isotherms obtained for all activated samples. All isotherms are of IIb type according to IUPAC classification, and are typical for microporous materials. They all exhibit type H3 hysteresis characteristic for inter-particle capillary condensation that usually occurs in granulated (agglomerated) materials. The onset and the width of the hysteresis loop slightly diminishes with activation time. It is probably related to increasing inter-particle spaces during activation.

Table 4.1 gives specific surface area (total, external, and microporous) and microporous volume of sample containing 11.3 wt.% of boron, thermally activated for 4 hours at 400 $^\circ$C, after each hour of sample annealing. For comparison, the sample characteristics before activation are also indicated. In contrast with purely carbon samples for which a monotonic increase of all parameters with annealing time was observed (Fig. 4.16), the parameters of annealed boron-carbon samples are fluctuating around constant (and very low) values. The specific surface area varies between 100 and 200 m^2/g (Fig. 4.16a). The highest microporous surface and volume were observed after 1 hour (34 m^2/g and 0.015 cm^3/g) and 4 hours (25 m^2/g and 0.013 cm^3/g) of samples annealing.
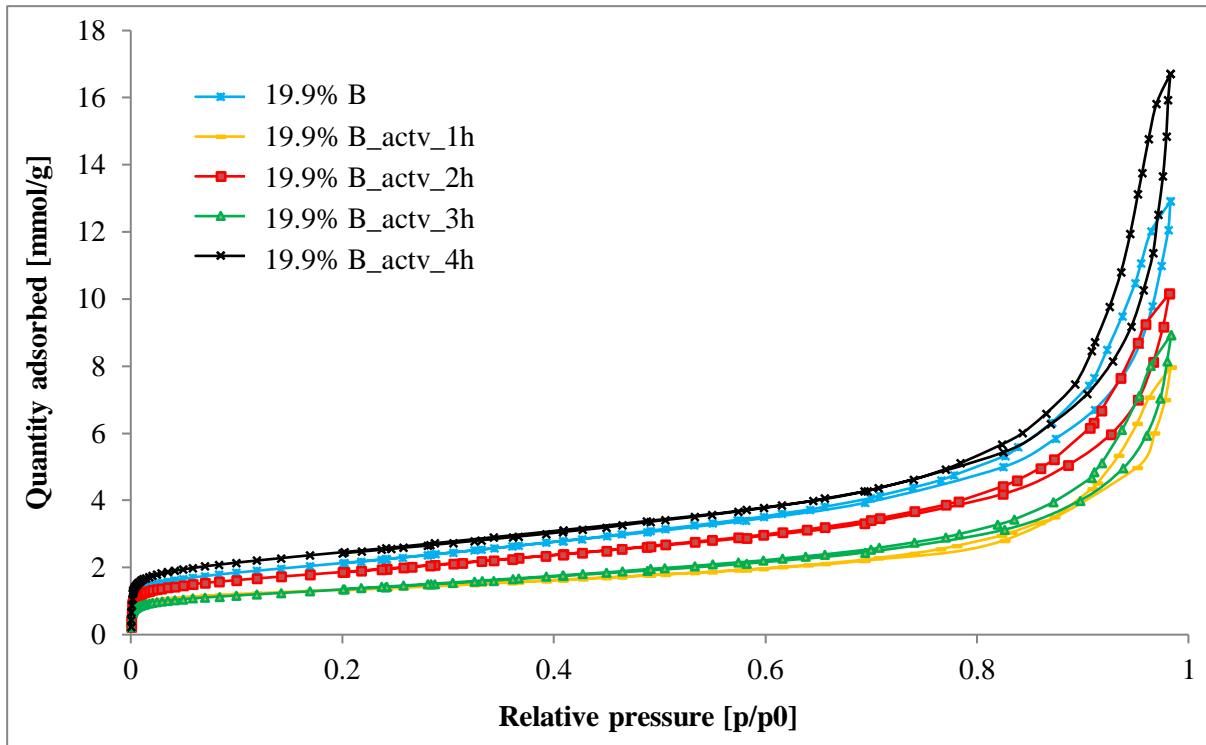
Figure 4.15. Nitrogen adsorption isotherms of sample with 19.9 wt.% of B before and after each step (1h, 2h, 3h, and 4h) of thermal activation.

Table 4.1. Specific surface area (SSA) and microporous volume of soot_2B sample after each step of thermal activation at 400 °C.

Sample	Total SSA [m²/g]	External surface area [m²/g]	Micropore area [m²/g]	Micropore volume [cm³/g]
19.9 wt.%B	168	164	4	0.004
19.9 wt.%B_actv_1h	107	73	34	0.015
19.9 wt.%B _actv_2h	146	128	18	0.010
19.9 wt.%B _actv_3h	105	96	9	0.005
19.9 wt.%B _actv_4h	193	168	25	0.013

There are several possible reasons why thermal activation of boron-containing samples is not efficient. The most plausible is that oxygen cannot access the sample interior, either because (i) the initial sample has too little open pores to efficiently initiate the activation, (ii) the sample heating causes structure modifications that prevent oxygen to penetrate into sample interior, or (iii) boron nanostructures, detected during microscopic analysis of samples' morphology block the oxygen access deep into the sample. This last hypothesis is supported by the quasi absence of the sample mass loss during activation (Fig. 4.16b). The initial mass loss of 2.5 %, observed after the first hour of annealing can be attributed to the activation of easily accessible external surface of the sample.
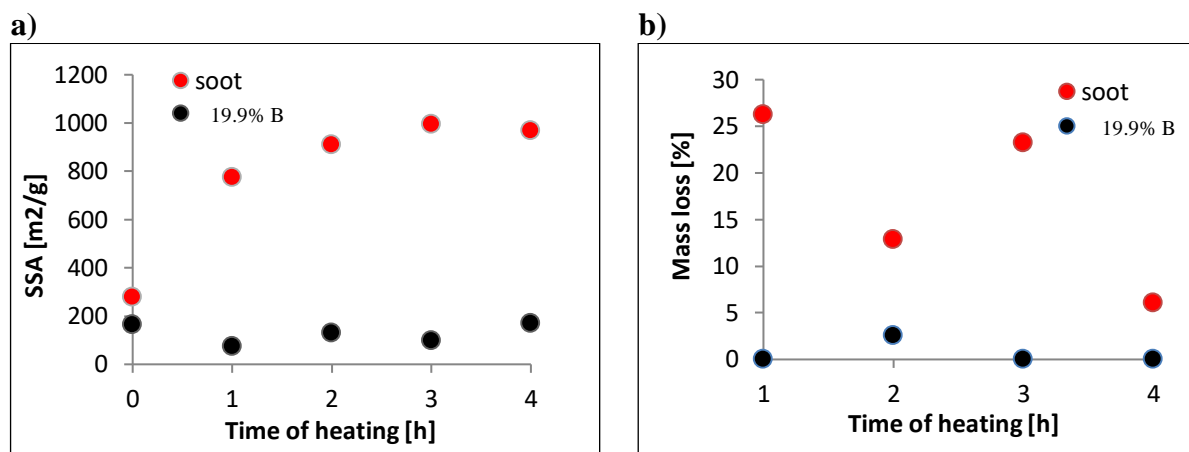
Figure 4.16. a) Specific surface area and b) mass loss for boron-carbon sample thermally activated at 400 $^\circ$C for four hours, with 1-hour time step. For comparison, the data for purely carbon samples are also shown.

Fig. 4.17 shows the distribution of pore sizes in gradually activated samples, measured after each annealing step. The porosity is almost independent on the annealing time, although some fluctuations of pore size distribution are observed: after the first hour of heating, the average pore width slightly increases (from 7 Å to 8 Å), then, after second and third hour of heating, all pore widths seem to appear with the same (low) frequency. After fourth hour of annealing the sample presents the same porosity as non-annealed sample. Therefore, we concluded that the thermal activation is not adapted to improve the porosity of boron containing carbons.

To verify if the presence of boron is the main reason of inefficacity of thermal activation, all remaining samples (with different boron content) were also thermally activated and their porosity analysed. Fig. 4.18 shows the nitrogen adsorption isotherms after four hours of activation. They are all of type IIb and present type H3 hysteresis. The hysteresis observed for sample containing the highest amount of boron (23.3 wt.%) is the widest. It indicates that this sample contains the large number of agglomerates, and that the adsorption occurs mainly in between the agglomerated particles.
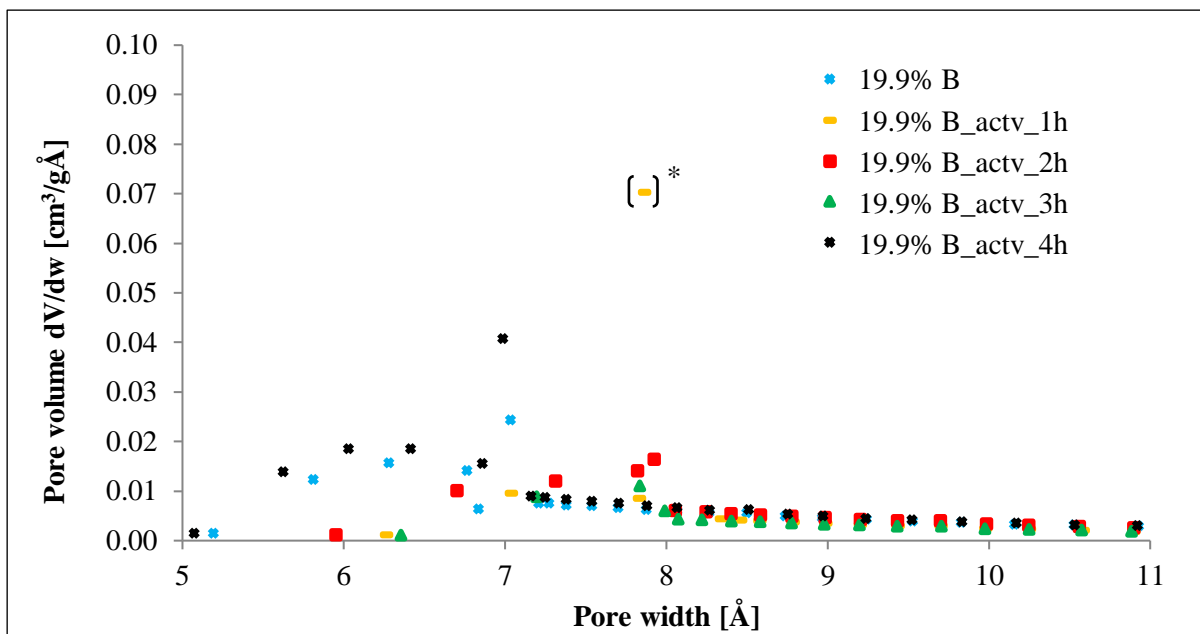
Figure 4.17. Pore volume in the function of pore size for thermally activated 19.9 wt.% of B sample after each 1-hour time step of annealing; point marked with asterisk * is an artefact.
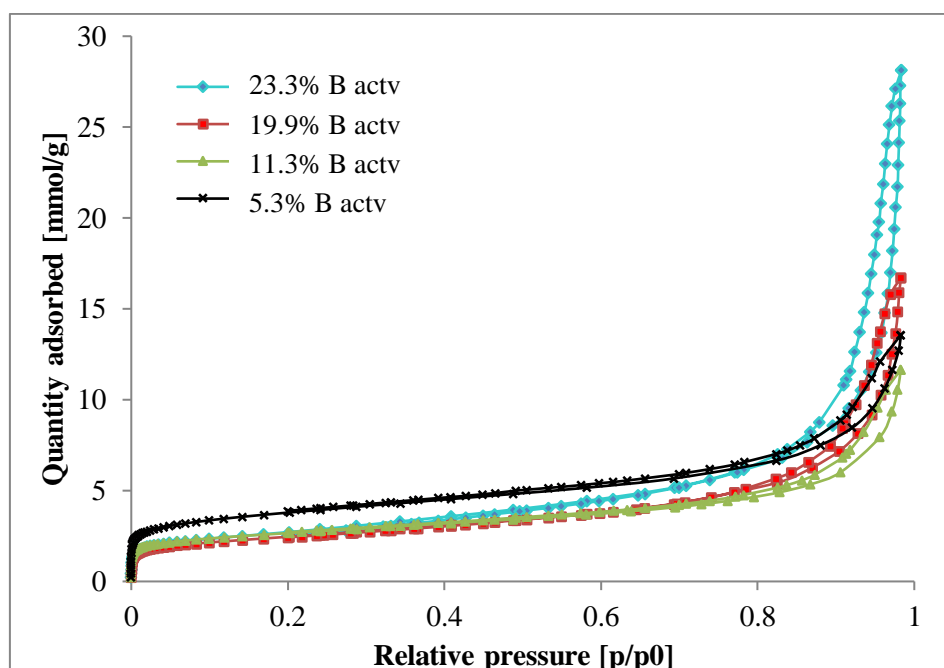

Figure 4.18. Nitrogen adsorption isotherms of activated boron-containing carbon samples after 4 hours of thermal activation at 400 $^{\circ}$C. The boron concentrations are: 23.3 wt.%, 19.9 wt.%, 11.3 wt.%, 5.3 wt.%.

Fig. 4.19 shows the pore size distribution for all samples, calculated using HK method and assuming slit shape of the pores. Within this approximation, all samples are almost non-porous. The highest pore volume appears in 23.3 wt.% and 11.3 wt.% of B samples, containing

pores between 6 Å and 8 Å of width. In the sample containing the lowest amount of boron (5.3 wt.%) the micropore volume is the highest, uniformly distributed between pore widths of 5 - 7 Å.
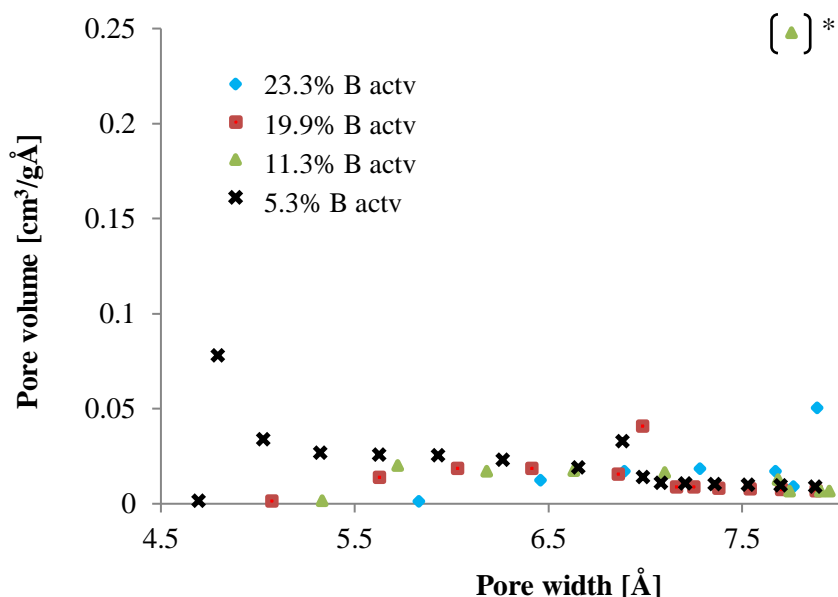

Figure 4.19. Pore volume in the function of pore size for thermally activated boron containing samples after 4 hours of annealing at 400 °C; point marked with asterisk * is an artefact.

Table 4.2 compares the specific surface area and microporous volume of the activated samples. Each parameter decreases with increasing boron concentration. To get more information about the origin of such behaviour we have carried out the analysis of samples' morphology, using microscopy and spectroscopy techniques.

Table 4.2. Specific surface area (SSA) and microporous volume of boron containing carbon samples after 4 hours of thermal activation at 400 °C.

Sample	Total SSA [m²/g]	External surface area [m²/g]	Micropore area [m²/g]	Microporous volume [cm³/g]
23.3% B actv	144	144	*	0.002
19.9% B actv	193	168	25	0.013
11.3% B actv	210	132	78	0.035
5.3% B actv	300	183	117	0.052

4.3.1.3. Morphology of boron containing activated samples

Fig. 4.20 shows the SEM images of four different regions of the sample containing 23.3 wt.% of boron, activated for 4 hours at 400 °C. The sample is strongly heterogeneous and

contains such formations as (i) carbon nanotubes (of the length of 6 µm and more, Fig. 4.20a), (ii) carbon microspheres with diameter of ~56 µm (Fig. 4.20b), (iii) carbon webs (Fig. 4.20c), and (iv) graphene flakes (Fig. 4.20d). These last structures could be tentatively assimilated to graphene oxide surfaces, by comparison with SEM picture published by Najafi et. al [4.9]. The composition of the microspheres is not known; however, it may consist in graphene oxide, too. The presence of oxygen is confirmed by EDS spectroscopy: thermally activated sample consist of 70% of carbon and 30% of oxygen. The presence of large amount oxygen in our samples is not surprising. The samples were stored without a particular care at ambient conditions; therefore, the graphene dangling bonds are supposed to be terminated by oxygen-containing groups, equally before and after thermal activation. The samples could also contain boron trioxide (III); however, this hypothesis is difficult to verify as is not possible to identify boron in presence of carbon by EDS method. Additionally, as temperature in the oven was not higher than 400 $^{\circ}$C, too low to allow BO_3 formation, the presence of boron trioxide is less probable.
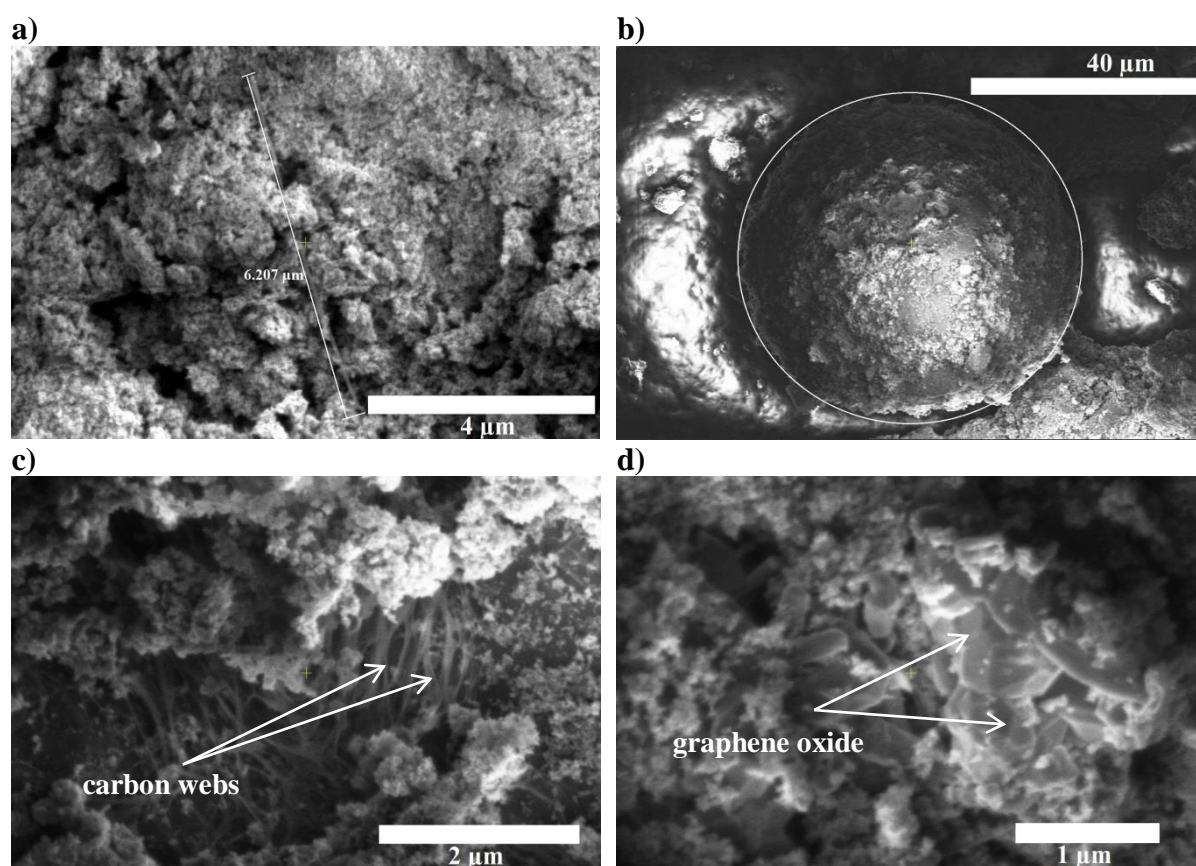

Figure 4.20. SEM images of activated sample with 23.3 wt.% of B. The images show specific carbon formation within amorphous, porous structure: a) carbon nanotube with length ~ 6 µm; b) carbon microsphere with diameter ~ 56 µm; c) carbon webs; d) graphene oxide flakes.

Fig. 4.21 shows HRTEM images for thermally activated sample containing 5.3 wt.% of boron. At nanometric scale two types of structures appear: amorphous phase composed of quasi spherical agglomerates (with ~30 nm of diameter, Fig. 4.21a), and well organized, tubular structures of the length from 30 to 90 nm, surrounded by graphene-like layers (Fig. 4.21b). The dark spots present within the tubes are accumulated carbon. We expected that the organized structures contain boron atoms incorporated into graphene structure. To confirm this hypothesis the fragment of the sample shown on Fig. 4.21b was analysed in detail.
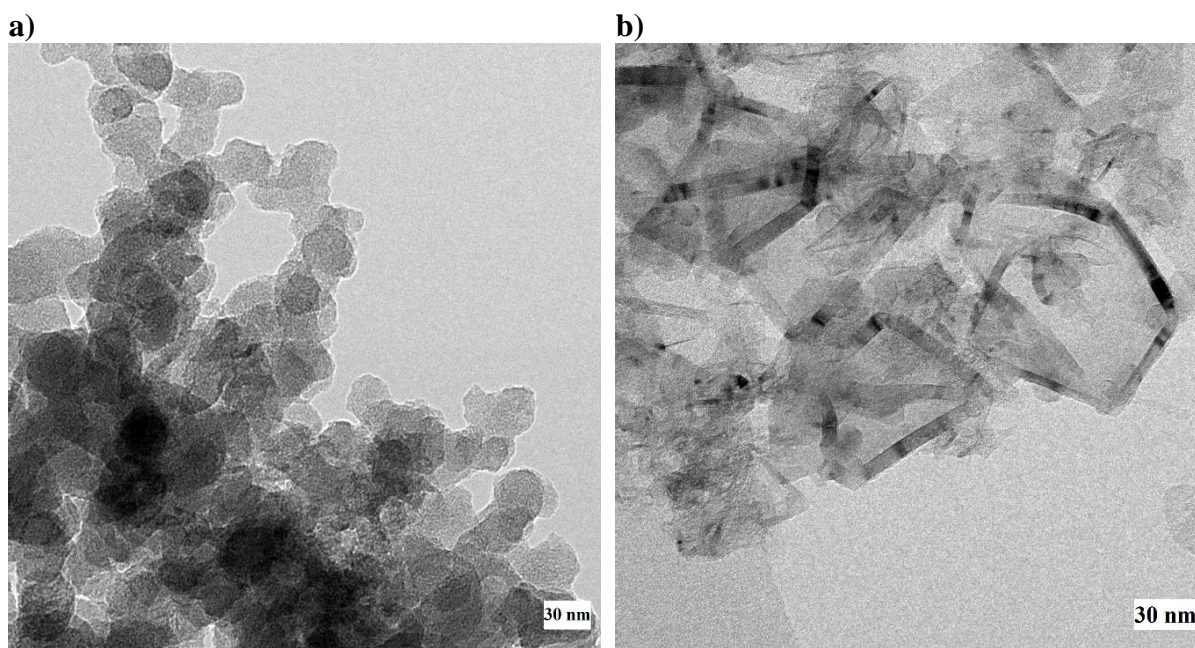

Figure 4.21. HRTEM images of thermally activated sample contains 5.3 wt.% of B. a) amorphous phase, containing spherical agglomerates, b) sample fragment containing a mixture of tubular structures and graphene-like flakes.

Fig. 4.22 shows the HRTEM images of some details of morphology of the activated sample containing 5.3 wt.% of boron. Three different types of material organization can be usually distinguished (Fig. 4.22a): core structures, layered carbon and overlapping structures. Crystallographic arrangement of the core and layered structures was analysed using Fourier Transform (FT) of their projection and showed on Fig. 4.22 c, d. Reflections points for layered structure (Fig. 4.22c) were identified as coming from [0 0 2] and [0 0 4] graphite lattice layers projected on [1 0 0] graphite lattice plane. As the projection on the [0 0 1] lattice plane does not allow the direct observation of the atomic arrangement of the layer, we cannot determine whether the layers contain substitutional boron atoms or are totally build up from carbon only. The structure of the core part of the sample is more complex. It shows many graphite stacking

fault (SF) (Fig. 4.22b), similar to those observed and described by Chen et al. [4.10]. The dispersion of layers' orientation results in noisy FT signal (Fig. 4.22d). However, three lattice planes: [1 0 -2], [0 0 3] and [1 0 1] (projected on [0 1 0] plane) can be identified. They are characteristic for boron carbide (B_4C) structure.
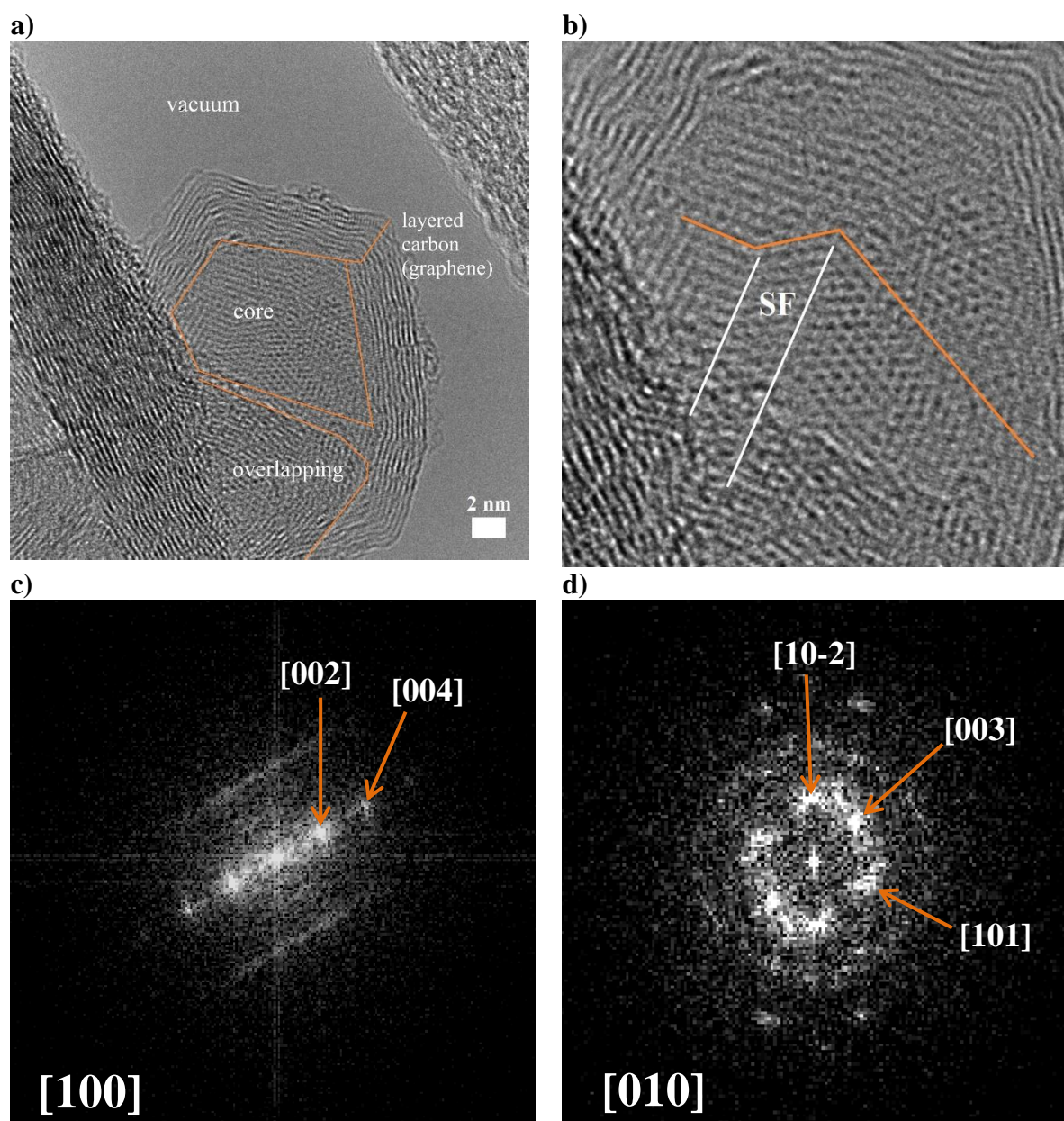

Figure 4.22. HRTEM images of thermally activated sample with 5.3 wt.% of B. a) sample fragment containing three different material organisations: core structure, layered (graphitized) carbon and overlapping structures; b) stacking fault defect (SF) in boron carbide structure; c) and d) diffraction patterns of layered carbon and core structure, respectively.

Fig. 4.23 presents the HRTEM (Fig. 4.23 a,b) and EELS (Fig. 4.23 c,d) images of the selected fragment of the activated sample containing 5.3 wt.% of boron, similar to the one presented on

Fig. 4.22. The presence and location of boron and carbon atoms can be affirmed by comparing the HRTEM images and EELS boron and carbon maps. The large core structure from Fig. 4.23a contains boron atoms, whereas the lamellar structure surrounding it is formed only by carbon atoms. In the same way, small onion-like boron structures appearing inside the core structure contain boron but are surrounded by the shells made of layered carbon. They are clearly visible on Fig. 4.23c, where they appear as small clear rings located at the same place where boron agglomerates appear.
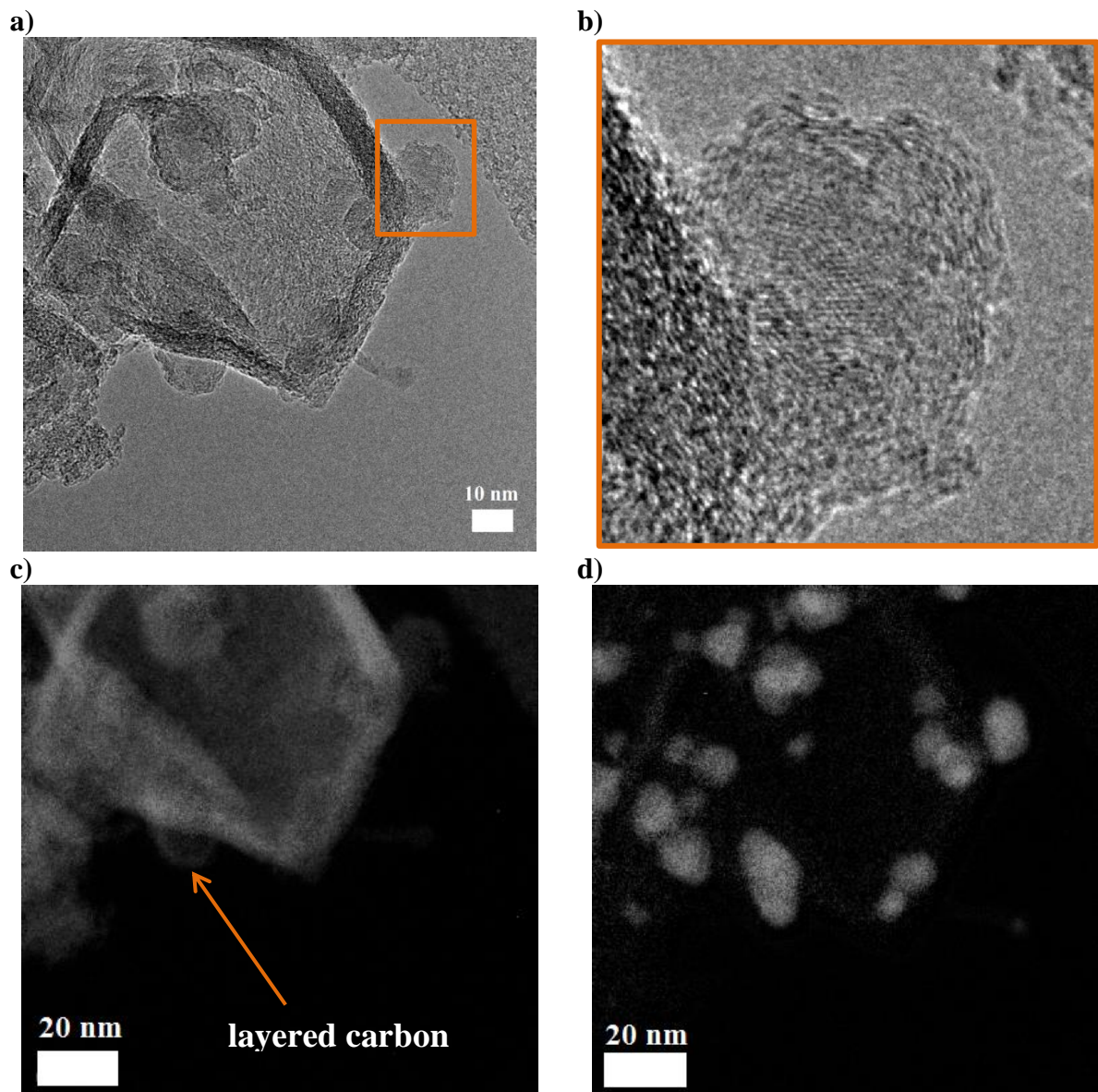

Figure 4.23. EELS analysis of thermally activated sample with 5.3 wt.% of B; a) HRTEM image of sample fragment containing core-type structure and b) zoom on analysed nanostructure; c, d) EELS carbon and boron map, of the sample fragment shown on Fig 4.23a.

4.3.1.4. XRD measurement

The structure of three thermally activated samples (all-carbon sample, and two boron containing samples with 23.3 and 5.3 wt.% of boron, respectively) was analysed using XRD. The samples were placed inside the capillary of 0.7 mm of diameter and exposed to the X-Ray radiation (λ = 0.15418 nm) for 20 minutes. Collected diffractograms were analysed using Crystallography Open Data base with Mercury program support. Fig. 4.24 presents the XRD pattern of thermally activated carbon sample. Four peaks, located at 2Θ = 26.50, 42.46, 44.61 and 54.65, perfectly correspond to hexagonal graphite structure of symmetry P63/mmc. They come from the reflexions from (0 0 2), (1 0 0), (1 0 1) and (0 0 4) graphite planes (given in Miller indexes (*hkl*)). The origin of the strong signal appearing below 2Θ = 10 was investigated previously by Lee et. al [4.11] and Braun et. al [4.12]. They both concluded that the signal appearing at the lowest angles (up to 2θ = 4) indicates that the sample is porous. The intensity of this signal increases in mesoporous samples. However, this signal may also indicate the presence of nanoparticles in the sample. If this signal is broad, the sample is mostly amorphous.
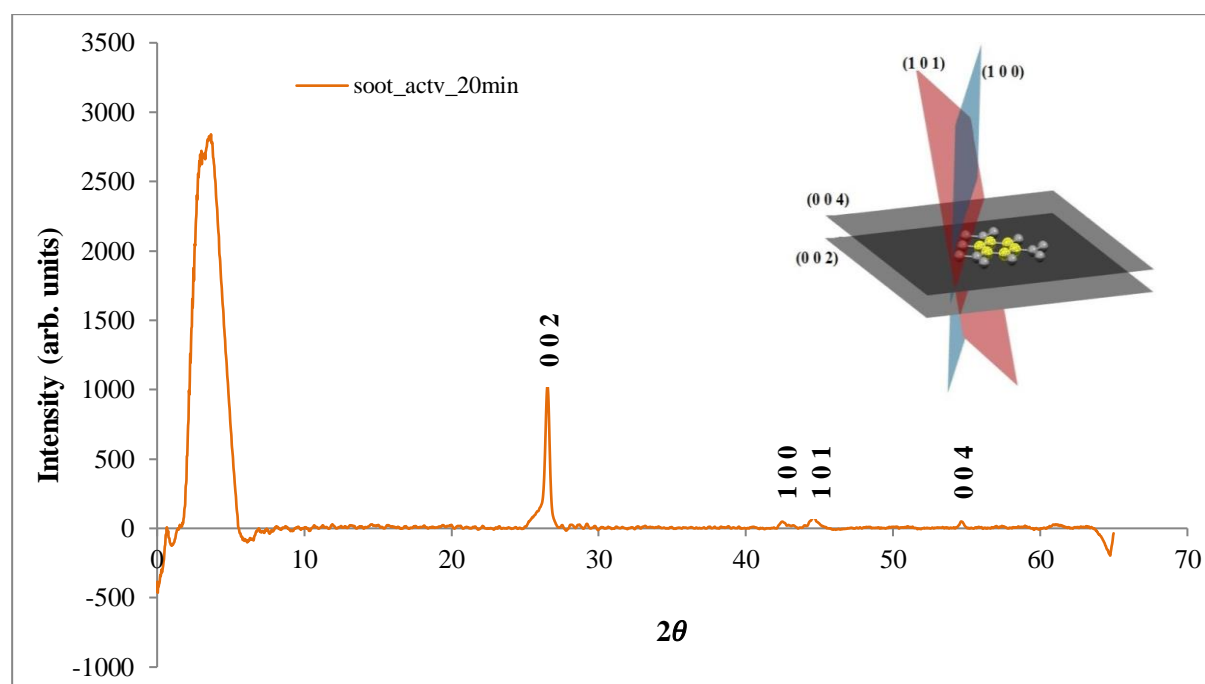

Figure 4.24. XRD pattern of thermally activated carbon sample. The insert shows a 3D picture of lattice planes. The hexagonal ring of carbon atoms is marked in yellow. Lattice planes (0 0 2) and (0 0 4) are parallels to the graphene surface, whereas (1 0 0) and (1 0 1) planes are perpendiculars to it.

Fig. 4.25 and 4.26 show the diffractograms of two boron-containing activated samples with the lowest (5.3 wt.%) and the highest (23.3 wt.%) boron concentration; for comparison, the diffractogram of pure carbon sample is also shown.

Even for the smallest boron content, the difference between diffractograms is noticeable (Fig. 4.25). The peaks related to graphitic organization, indexed (1 0 0), (1 0 1) and (0 0 4) are still present. The intense signal $2\Theta=26.48$ corresponds to (0 0 2) lattice plane in graphite. We have not succeeded to identify the shoulder peak at $2\Theta = 26.08$. The small signals collected above $2\Theta=40$, at $2\Theta = 37.89$ and $2\Theta = 53.25$ correspond to lattice planes (2 0 -1) and (2 0 5) of boron carbide structure.
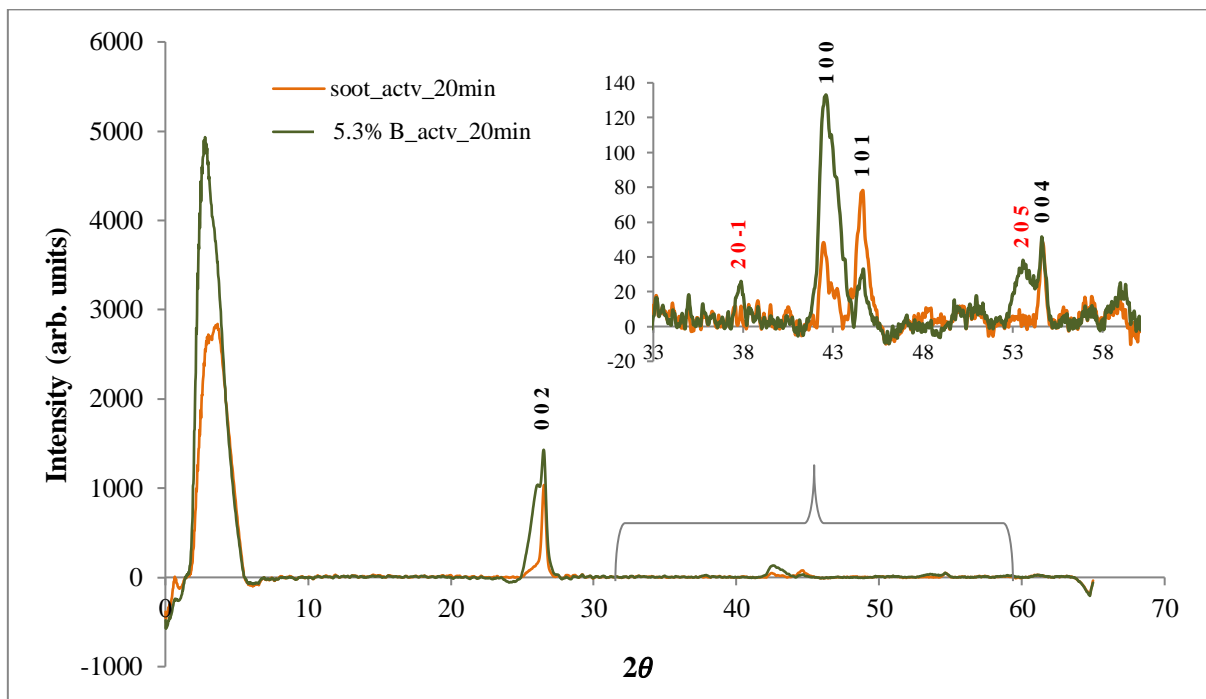

Figure 4.25. XRD diffractogram of thermally activated sample with 5.3 wt.% of B; for comparison, the diffractogram of pure carbon sample is also shown. The peaks corresponding to graphitic structure are marked in black: those corresponding to boron–containing structures are given in red.

The diffractogram of activated sample with the highest boron concentration (Fig. 4.26) contains also the signals from graphitic structure (at $2\Theta = 26.53$ (0 0 2), 42.69 (1 0 0), and 54.73 (0 0 4)). The peak corresponding to (1 0 1) plane disappeared; it means that the vertical stacking of graphene layers has been disturbed. The graphite stacking ABAB is not conserved anymore. As the concentration of boron increased, more signals that can be tentatively assigned to boron-containing structure appear. The peaks at $2\Theta = 35.02$, 37.83, 42.69, and 53.60 have been

attributed to boron carbide nanocrystals (lattice planes (1 0 4), (2 0 -1), (1 0 -5), and (2 0 5), respectively). Two of these peaks have been already observed for the sample with lower boron concentration pattern (Fig. 4.25). Furthermore, the broader peak located at $2\Theta \sim 43$ was attributed to coexisting boron (1 0 -5) and carbon (1 0 0) structures. The signals appearing at $2\Theta = 14.65$ and $2\Theta = 28.03$ can be tentatively identified as corresponding to the reflexions from the lattice planes (110) and (220) of tetragonal bulk boron nanocrystals with symmetry P42/nnm). The signals at $2\Theta=14.38$ and $2\Theta=28.71$ are not included in XRD database.
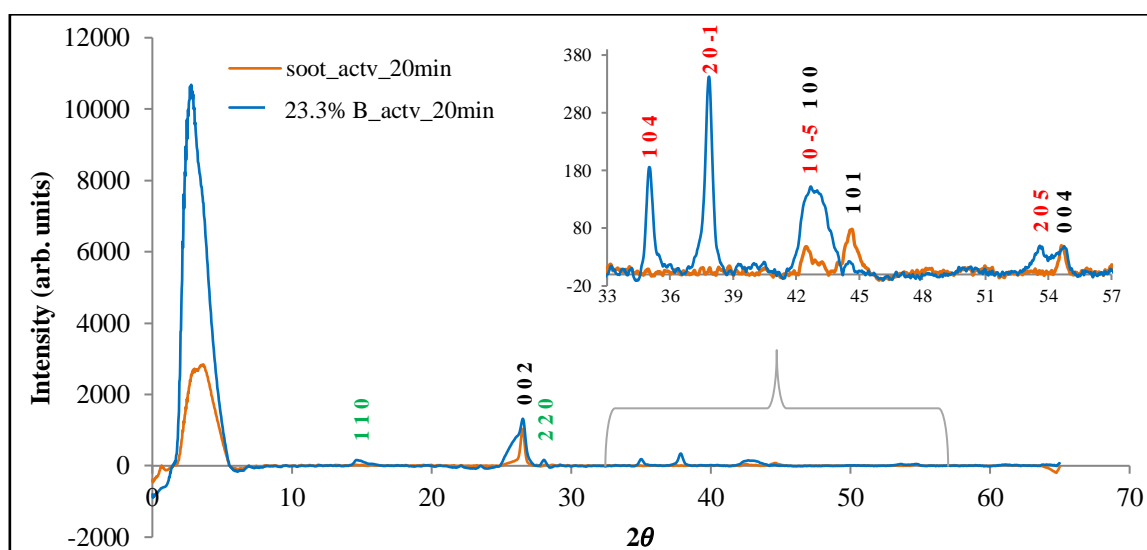

Figure 4.26. XRD diffraction pattern for the thermally activated sample with 23.3 wt.% of B; for comparison, the diffractogram of pure carbon sample is also shown. The peaks corresponding to graphitic structure are marked in black: those corresponding to boron–containing structures are given in red and tetragonal boron structure is marked in green.

Fig. 4.27 summarizes the above-described observations. (i) The intense the signal at low 2Θ values (of ~3), is a signature of sample porosity; (ii) The intensity of the additional peak appearing at the shoulder of carbon signal at 2Θ ~26 also increases with boron concentration. As in general the signals related to boron structures do not appear in this 2Θ range, this peak can result from a new carbon structure that develops in the presence of boron. (iii) The intensity of signals from boron carbide (at $2\Theta = 35.01$ and $2\Theta = 37.83$) increases with boron concentration.
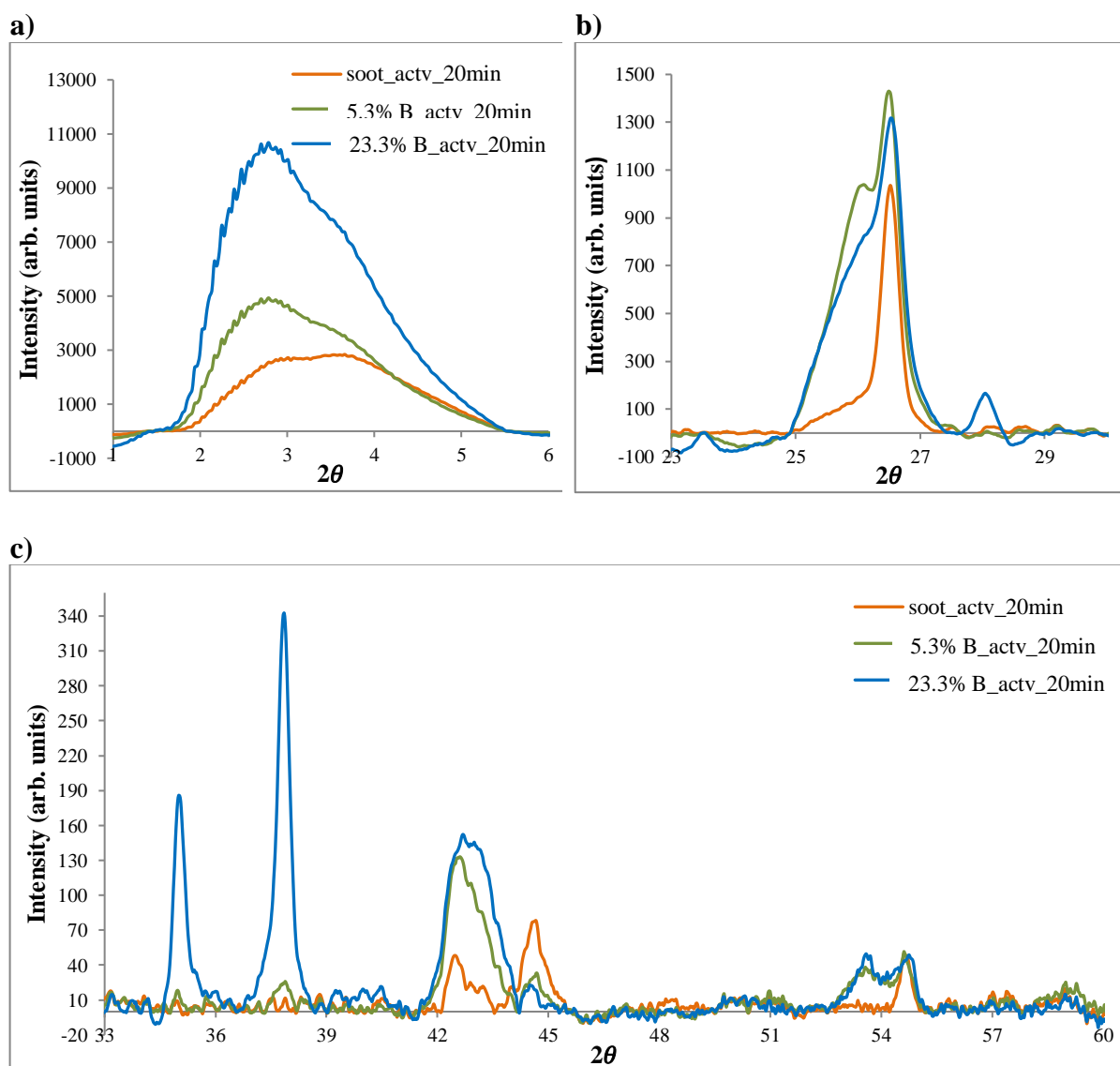
Figure 4.27. Comparison of XRD patterns for thermally activated samples: soot, 5.3 wt.% of B and 23.3 wt.% of B in three different 2θ ranges: a) $1 < 2\theta < 6$; b) $23 < 2\theta < 39$ and c) $33 < 2\theta < 60$.

4.3.1.5. ^{13}C and ^{11}B MAS NMR of thermally activated boron-carbon samples

Figure 4.28 shows ^{13}C MAS NMR spectra of all thermally activated boron-containing samples. All spectra consist in a one broad line, extending from 0 ppm to 250 ppm. Although the sample has been rotated at frequency of 10 kHz, the peaks from different residues are not resolved. This result is not typical for the one observed for organic materials, where usually the spinning rate of 2.5 kHz is sufficient to resolve the fine structure of the sample spectrum. Apparently, higher spinning rate is necessary in the case of prepared samples. Additionally, the spinning side bands (marked by * on Fig. 4.28) appear exactly at the bottoms of observation

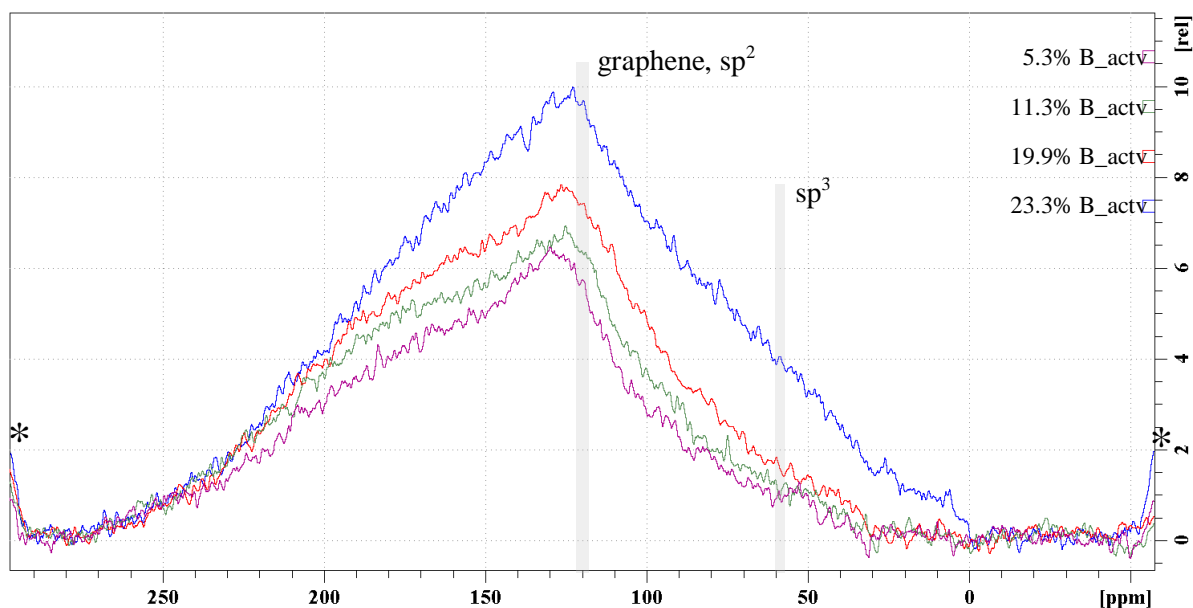windows and their replica merge with sample signal, that makes the spectrum analysis even more difficult.

Figure 4.28. ^{13}C MAS NMR spectra for thermally activated boron-carbon samples; 23.3 wt.% (blue), 19.9 wt.% (red), 11.3 wt.% (green), 5.3 wt.% (violet). The positions of resonances for sp^2 and sp^3 carbons are indicated by the grey lines.

The observation of unresolved MAS NMR spectrum is usually a sign of amorphous structure of the sample. Such a broad ^{13}C signal (extending from 0 to 150 ppm) was already observed for amorphous carbon by Kim et al. [4.13] (the authors used the MAS rate varying from 11 kHz to 14 kHz).

To get more insight into the origin of this signal we performed a deconvolution of the spectra from Fig 4.28. We were assumed the Gaussian shape of the peaks. To compare the spectra of different samples, the intensity of each spectrum was normalized to value of 10 (in relative units). Each spectrum can be decomposed four major peaks, located around 200 ppm, 150 ppm, 130 ppm, and 75 ppm (Fig. 4.29). According to data reported in the literature [4.13, 4.16] and collected on a large variety of crystalline and amorphous carbon materials, the signals at chemical shift 130 ppm and 62 ppm correspond respectively to carbon sp^2 hybridization (typical for graphene like structures) and sp^3 (tetragonal, out of plane) hybridization. The lines located between 150 and 200 ppm could be attributed to the –C=O groups, for which the signals appear usually around 180 ppm.

The intensity of signal at 130 ppm increases when concentration of boron inside the sample decreases. It means that there is higher quantity of sp^2 hybridized carbons when the concentration of boron in the sample is low. On the contrary, the signal at 75 ppm, typical for sp^3 carbon hybridization broad and intense for sample with 23.3 wt.% of boron, splits and disappears for low boron concentrations. We can expect that this signal results from sp^3 carbons being a part of boron-carbon structures like B$_4$C, where boron is located out of carbon plane and carbon-boron geometry becomes more tetragonal. The intensity of both signals located around 200 ppm and 150 ppm and tentatively related to the carbon-oxygen bonds are fluctuating independently on boron concentration.
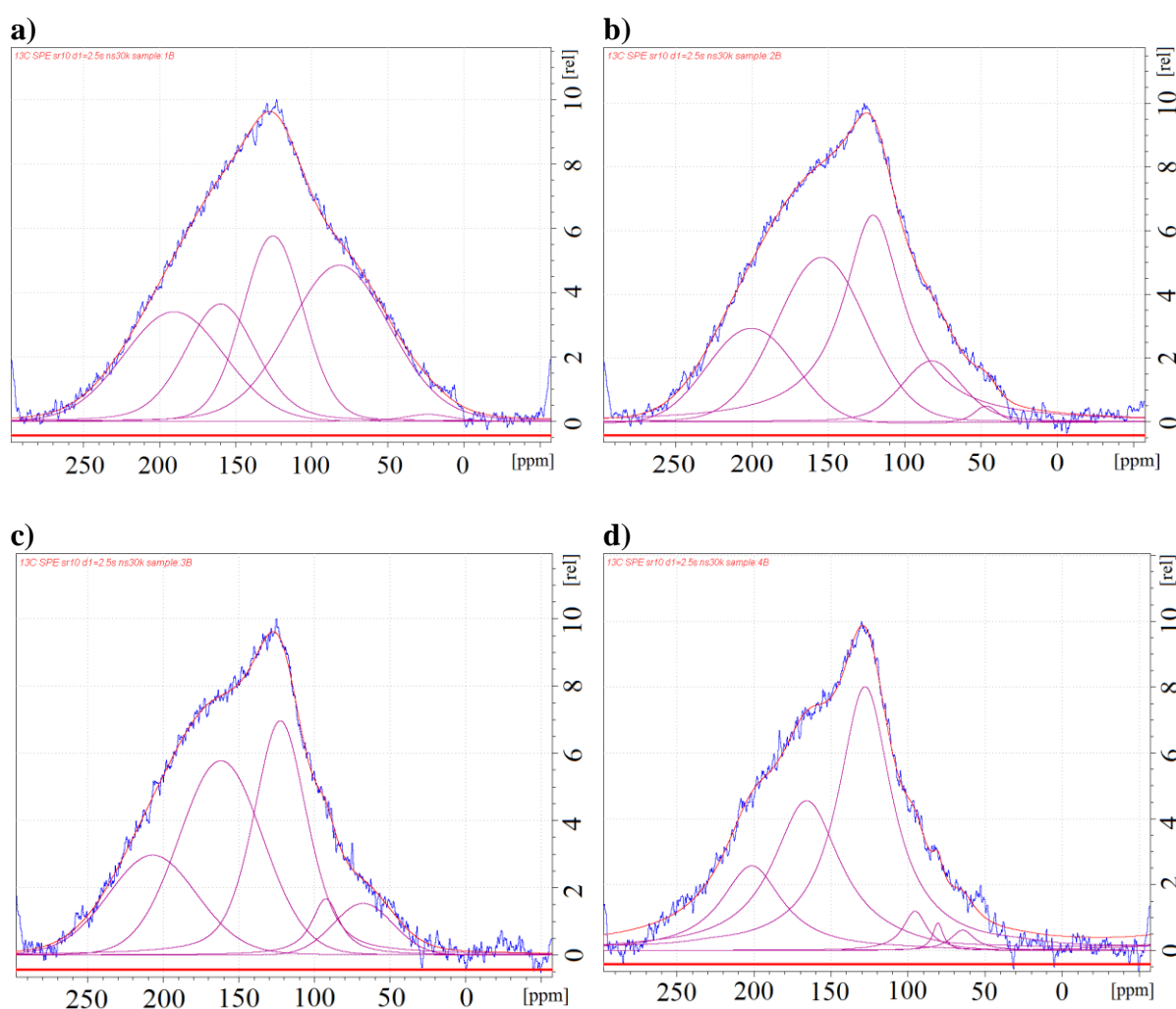

Figure 4.29. Deconvolution of ^{13}C MAS NMR spectra for thermally activated boron-carbon samples with different boron concentrations: a) 23.3 wt.%, b) 19.9 wt.%, c) 11.3 wt.%, d) 5.3 wt.%.

Fig. 4.30 shows the ^{11}B MAS NMR spectra of the same samples. Spinning side-bands (marked by *) are separated from the main peak by the distance corresponding to spinning frequency (10 kHz). As expected, the intensity of the ^{11}B signal increases with boron

concentration. According to Shirasaki et al. [4.4] (left upper corner of Fig. 4.30) the main signal corresponds to homonuclear B-B dipolar interaction in the boron carbide type structure. The peak at the shoulder of the main resonance, appearing at -10 ppm can originate from isolated boron atoms and their second-order quadrupolar interaction with carbon [4.4].
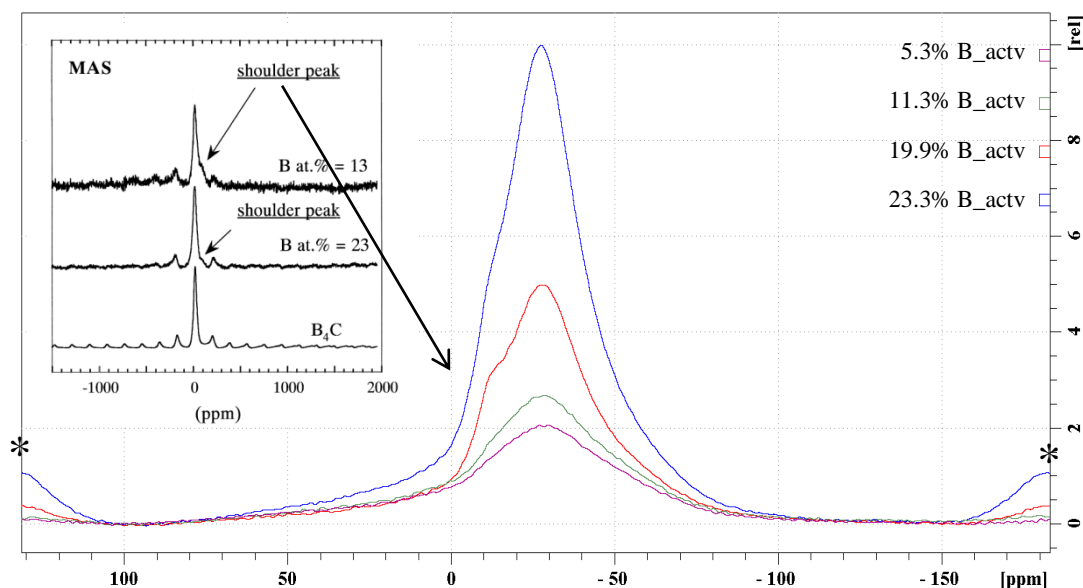

Figure 4.30. ^{11}B MAS NMR spectra for thermally activated boron-carbon samples; 5.3 wt.% of B (violet), 11.3 wt.% of B (green), 19.9 wt.% of B (red), 23.3 wt.% of B (blue). The insert shows ^{11}B MAS NMR spectra of B_4C and B_xC_{1-x} deposited at 1140 $^\circ$C [4.3].

Each spectrum from Fig. 4.30 was deconvoluted with Gaussian functions; the results are shown on Fig. 4.31. The main signal, identified as a boron carbide resonance, is located at the same chemical shift of -25 ppm in all samples. For both samples with the highest boron concentrations (23.2 wt.% and 19.9 wt.%) (Fig. 4.31 a,b) it is the dominant line of the spectrum. For lower boron concentrations (11.3 wt.% and 5.5 wt.%) the spectrum can be decomposed in three additional signals appearing at 10 ppm, -15 ppm and -55 ppm (Fig. 4.31 c,d). We have not identified the origin of these lines. They correspond probably to different interactions between dispersed boron atoms and carbons. The signal at -10 ppm broadness and its intensity is increasing when the boron concentration decreases.
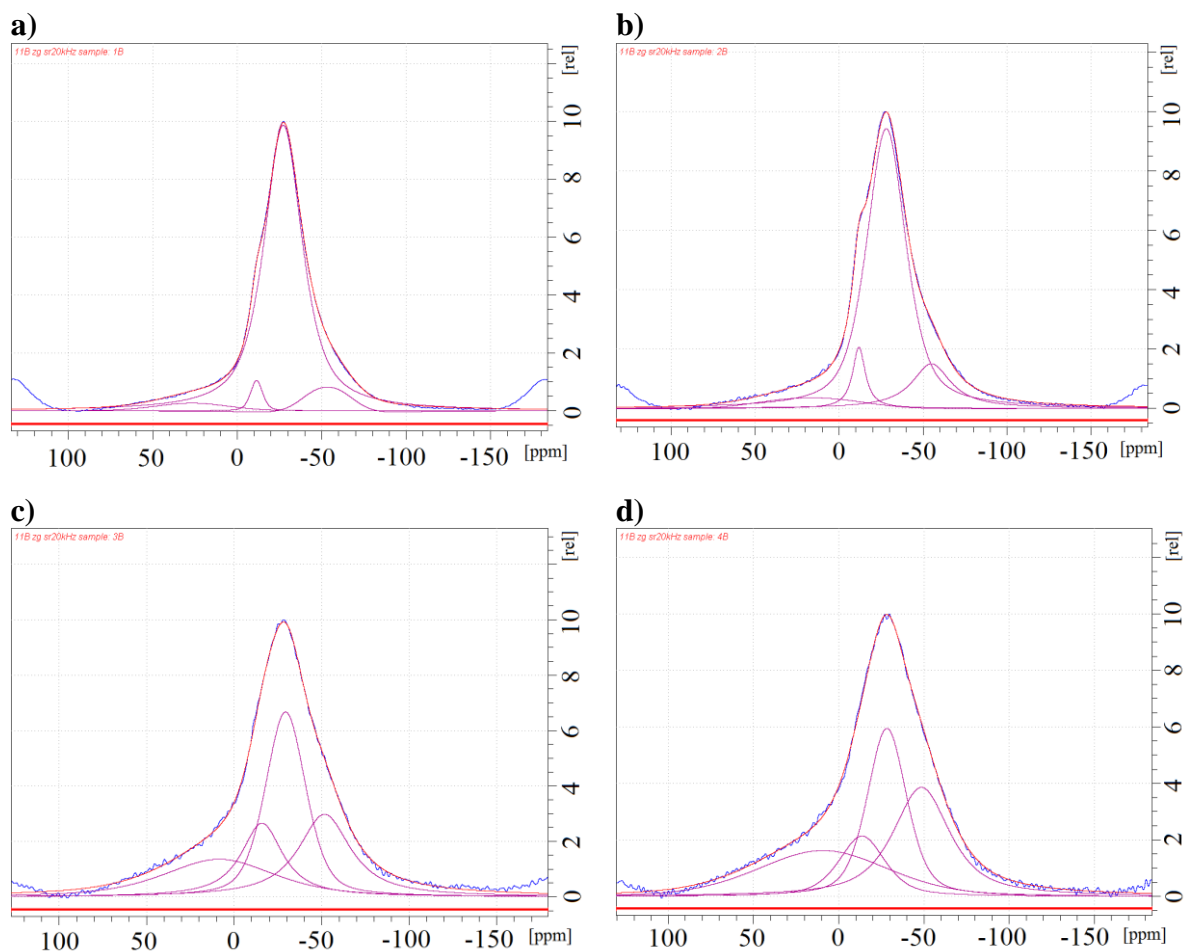
Figure 4.31. ^{11}B MAS NMR spectra for thermally activated boron-carbon samples: a) 23.3 wt.%, b) 19.9 wt.%, c) 11.3 wt.%, d) 5.3 wt.%.

4.3.1.6. Hydrogen adsorption in thermally activated boron-carbon samples

We have also determined the isosteric heat of hydrogen adsorption for thermally activated boron containing carbons. Before adsorption experiment, all samples were degassed at 250 $^{\circ}$C in high vacuum for 12 h. In each case the sample mass was between 100 mg to 135 mg. The volumetric adsorption experiment was performed using BELSORP apparatus equipped with cryostat which allows to carry out the measurements at well-defined low temperatures. The samples' dead volume was measured using nitrogen gas; its value varied between 35 to 37 cm^3. Hydrogen adsorption isotherms were measured at 67 K, 77 K and 87 K (Fig. 4.32). Between the experiments at different temperatures hydrogen was evacuated from the samples by pumping at room temperature. We assumed that at low pressures the excess and total adsorbed volumes are nearly identical.
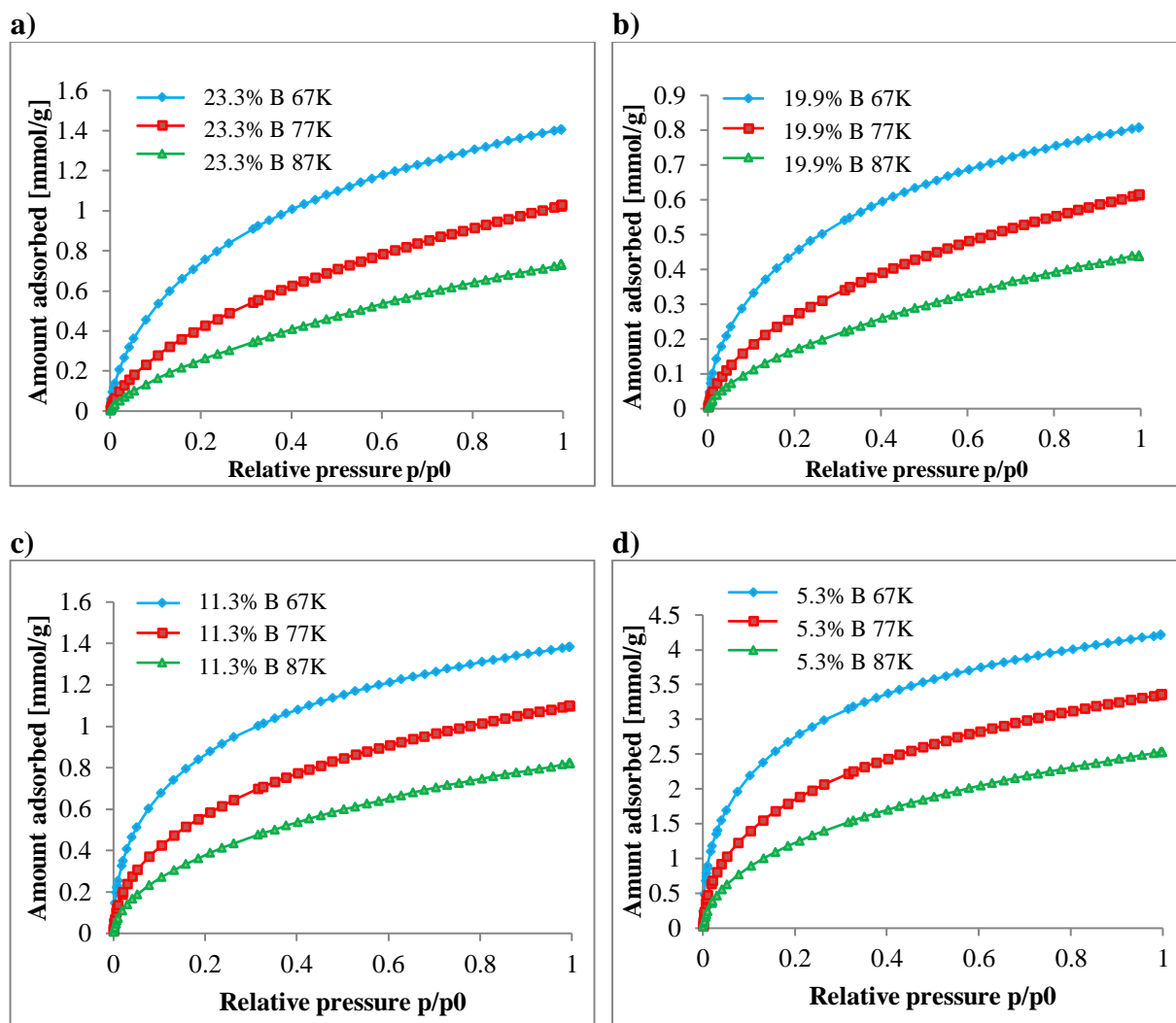
Figure 4.32. Hydrogen adsorption isotherms at 67 K, 77 K and 87 K, for all thermally activated boron-carbon samples.

The isosteric heat of adsorption was calculated from Clausius-Clapeyron equation (4.1) according to the procedure described in paragraph 4.2.1.4, using the slope of ln(p) versus 1/T at constant adsorbed amount. The calculated isosteric heat was then plotted in a function of volume of adsorbed gas (Fig. 4.33). The highest adsorption energy was obtained for activated samples containing 11.3 wt.% (8.15 kJ/mol) and 5.3 wt.% (8.17 kJ/mol) of boron The isosteric heat for activated samples containing 23.3 wt.% and 19.9 wt.% of boron is slightly lower, 7.05 kJ/mol and 7.67 kJ/mol, respectively. This small difference in adsorption energies (not larger than 1 kJ/mol) can be due to small morphological differences between the samples. In general, the calculated values are lower than those obtained on not-activated samples (ΔH = 9.06 kJ/mol, paragraph 4.2.1.3). Although this difference is not large, it is difficult to attribute it only to the differences in precisions of the experiments used in both cases (gravimetric and volumetric) for

non-activated and activated samples, respectively. It is more plausible that sample activation at ambient atmosphere blocked the access to the sample parts with the highest binding energies or have saturated them. The first possibility seems to be supported by the observation of very low porosity and sample surface after activation.
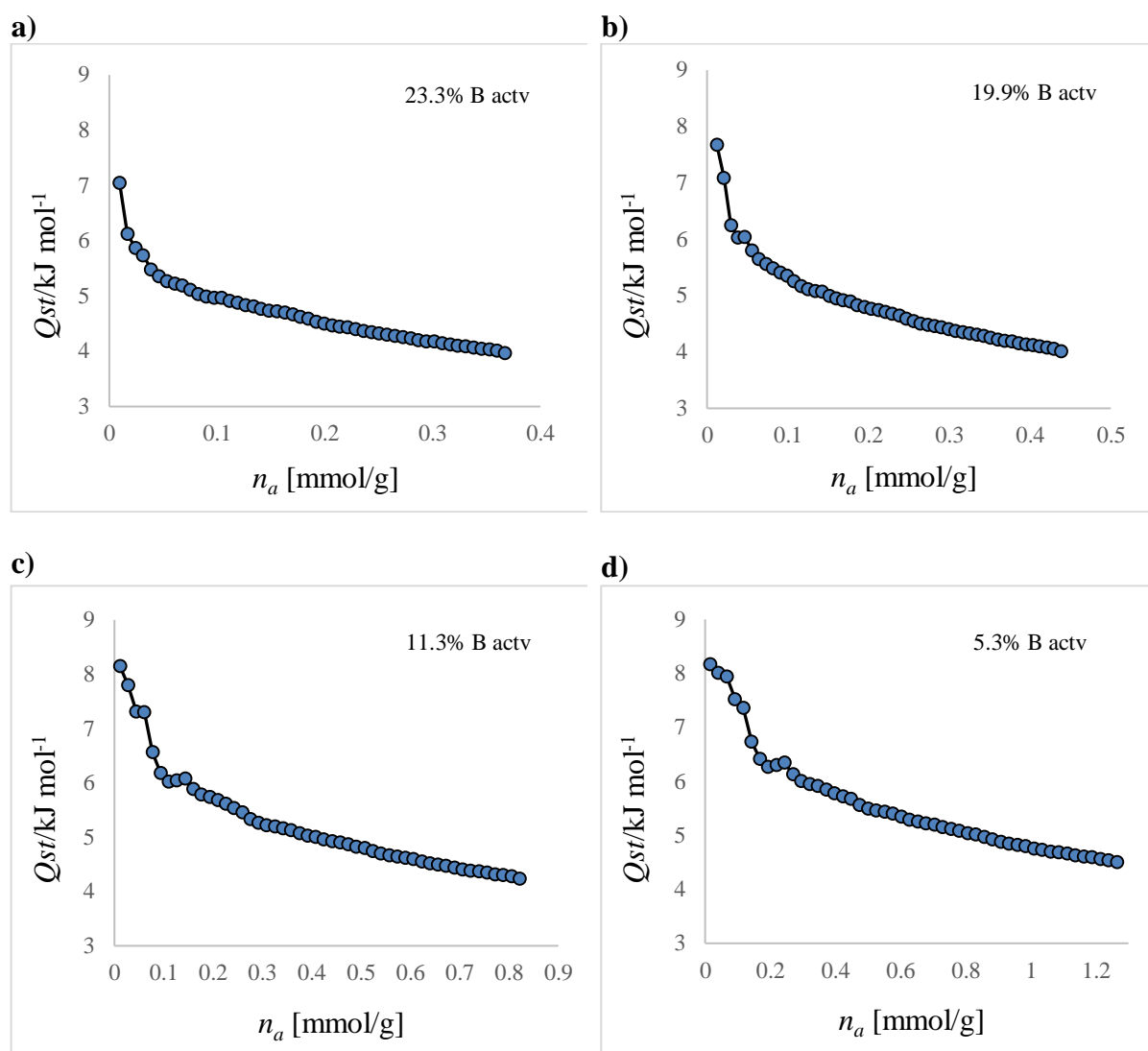
Figure 4.33. Isosteric heat of adsorption calculated from Clausius-Clapeyron equation for all thermally activated boron-carbon samples a) 23.3 wt.%, b) 19.9 wt.%, c) 11.3 wt.%, d) 5.3 wt.%.

4.3.2. Chemical activation

As the thermal activation of boron-containing carbons obtained by electric arc discharge appeared inefficient, we decided to test the efficacy of chemical activation of these materials. This chapter describes the procedure of chemical activation with KOH and its influence on

sample morphology and adsorption properties. All presented results were obtained for sample containing 11.3 wt.% of boron.

### 4.3.2.1. Chemical activation procedure

As for pure carbon samples, our protocol of chemical activation of boron containing samples was based on procedure proposed by Romanos et al. (see chapter 3.3.2). First, 200 mg of sample powder was mixed with KOH in 1:3 weight ratio in porcelain mortar. Then, the mixture has been placed inside the furnace in the ceramic crucible and heated up to 800 $^{\circ}$C with temperature ramp of 5 $^{\circ}$C/min under nitrogen gas flow (500 ml/min). After two hours of annealing at 800 $^{\circ}$C the heating has been turned off and the sample cooled down by itself.

As the samples contained boron, the procedure of removal of unreacted KOH from activated sample had to be performed with a special care. In fact, a secondary reaction of KOH with boron in presence of water can occur:

$$B + KOH + H_2O \rightarrow KBO_3 + H_2^{\uparrow}$$
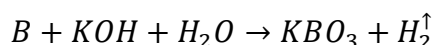
leading to the production of gaseous hydrogen. To avoid KBO_3 and hydrogen formation, during the sample rinsing with distilled water a neutralizing agent (37% diluted HCl (pH= 3.5)) was added in drops into the solution until pH= 7 was reached. However, at the very beginning of the rinsing procedure, before HCl addition we have always detected gaseous hydrogen. This fact suggest that our sample contains a not-negligible fraction on boron that can easily react with KOH. It means that either (i) the arc–produced samples contain a not-negligible fraction of unreacted boron powder (not incorporated into carbon structure), (ii) a fraction of boron atoms was released during sample activation, (iii) during the synthesis some particles of boron carbides (i.e. B_4C) have been formed and were easily accessible for molecules of reactant.

After neutralization with HCl the sample was additionally rinsed five times with distilled water to remove the formed KCl salt, and then annealed during approximately 2 hours at the temperature of 120 $^{\circ}$C, until the total evaporation of liquid. The remaining black powder had a mass of 185.5 mg; it means that the sample lost 7% of its weight during activation.

4.3.2.2. Morphology of activated samples

The morphology of boron-carbon activated sample was examined using SEM microscopy. Surprisingly, the observed structures (Fig. 4.34 a,b) are totally different from those usually observed in activated carbons that show large number of open pores and have specific surface area over 2500 m^2/g. Here the sample fragments seem to be composed of agglomerates of the size around 1 µm, parched, and apparently non-porous (Fig. 4.34b). Such morphology suggests that the specific surface areas of the sample is low. In addition, on the surface of agglomerated particles smaller formations are observed. They appear as bright spots (Fig. 4.34c), or as well-organized needles of the lengths of 100 µm and more (Fig. 4.34d).
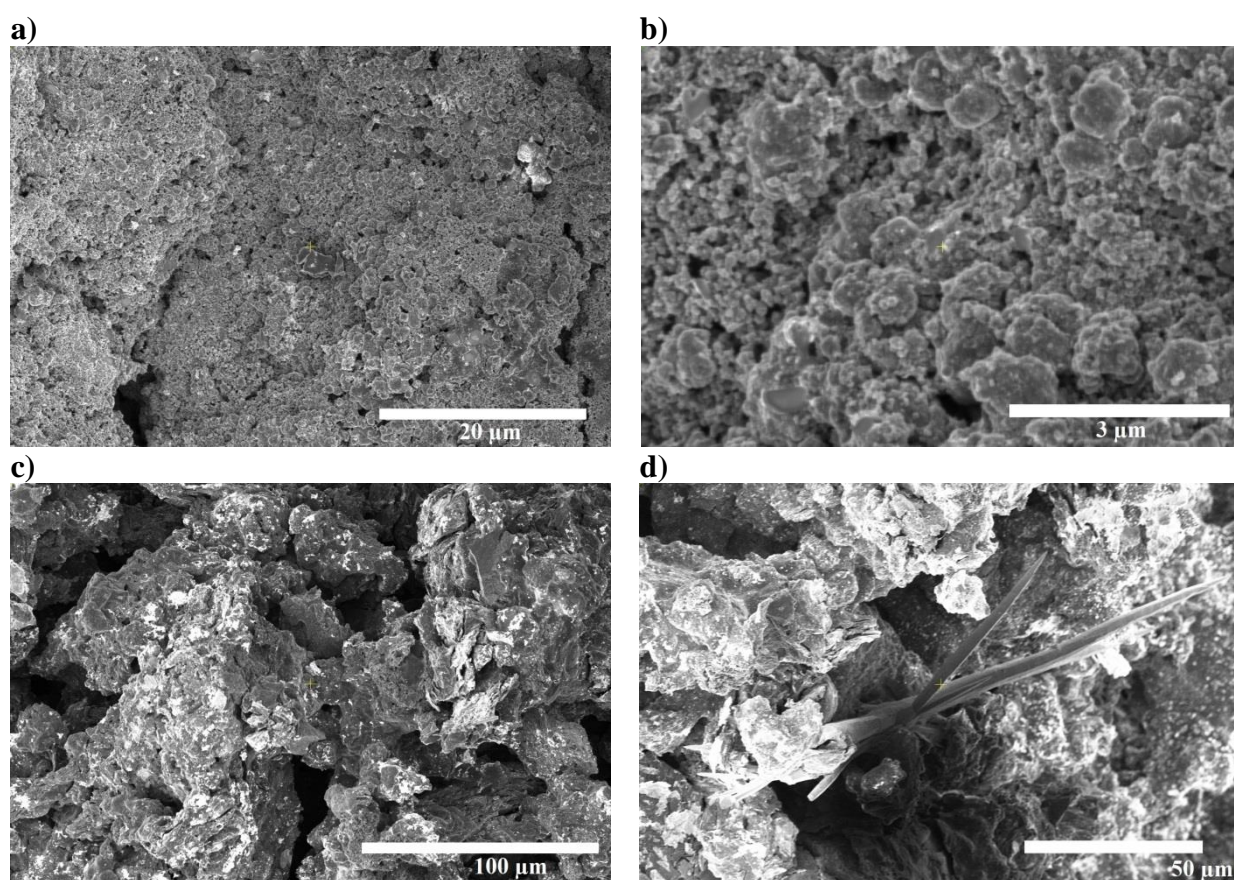

Figure 4.34. SEM images of chemically activated boron-carbon sample with 19.9 wt.% of B. a,b – sample surface showing agglomerates of the size of ~1 µm; c, d – bright spots on the surface agglomerates and needle-like structures of the length of more than 100 µm.

To get the information about the chemical nature of observed structures (in particular, that of the thin film of powder that seems to cover the surface of agglomerates), EDS measurements were carried out. Fig. 4.35a shows the chemical composition of the sample fragment presented on Fig. 4.34d. After activation, more element is present in the samples that

initially contained only carbon (and boron, not discernible from carbon in EDS experiment), and oxygen (Fig. 4.35b, Fig. 4.35e). Potassium (10 at.%, Fig. 4.35c) and small amount of chlorine (0.6 at.%, Fig. 4.35d) impurities are the residues of chemical activation with KOH, and solution neutralization with HCl. They were not properly removed from the sample after activation. It indicates that the applied rinsing protocol is not sufficient/efficient, especially to remove potassium, that covers a significant part of the sample surface.

Small amount of silicon (~1 at.%, Fig. 4.35g) and aluminium (less than 0.5 at.%, Fig. 4.35h) appear simultaneously at the same locations. They can be reasonably attributed to the traces of aluminosilicates introduced during grinding of the sample and KOH in the porcelain mortar. They are not removed from the sample by rinsing and cover the sample surface forming a thin powder film. Again, it suggests that the rinsing protocol has to be improved. One of the possible solutions is to sonicate the rising solution, to minimize the powder deposition on sample that we want to recover.

Needle –like structures contain mostly calcium, oxygen, silicium and aluminium (Fig. 4.35a-h). Similar structure was observed by Rohanova et. al [4.14] and identified as a CaO · SiO_2 crystals. Calcium (~9 at.%) was probably introduced either from porcelain mortar (during sample grinding) or from impure distilled water. As all manipulations were executed at ambient atmosphere, oxygen is present all over the sample. Depending on place of detection, the oxygen fraction in the observed area varies from 20 at.% to 77 at.%.
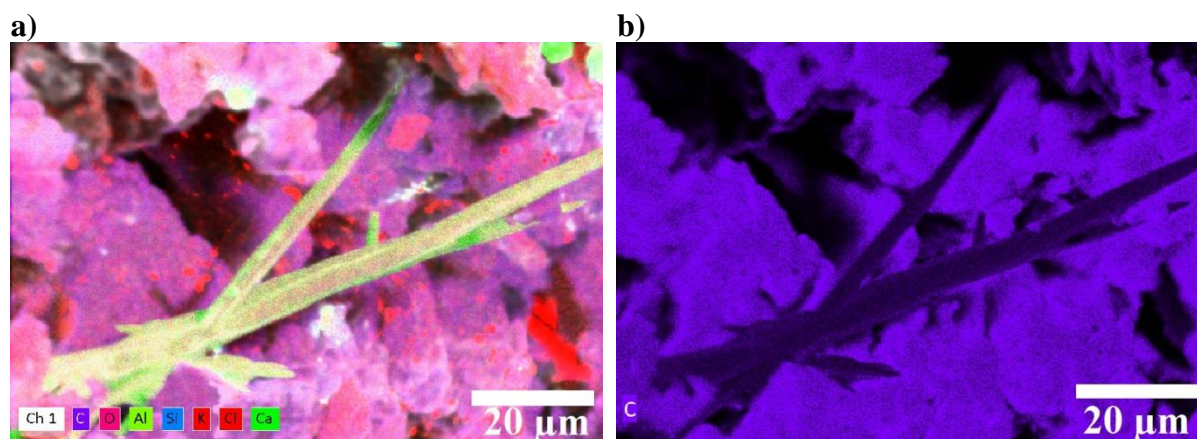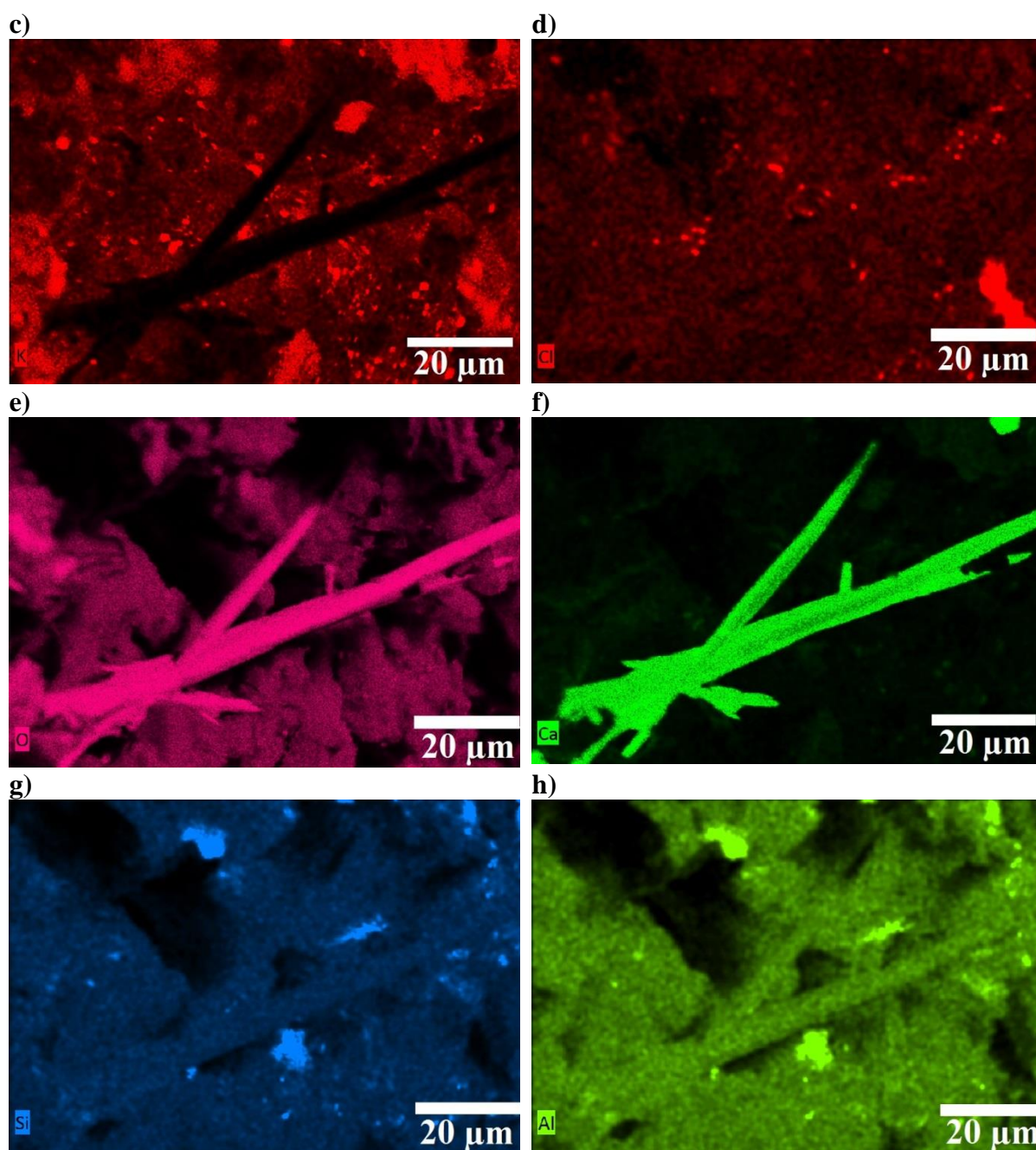
Figure 4.35. EDS images and atomic composition of sample fragment from Fig. 4.34d, containing needle-like structure; a) global representation of atomic composition, b) carbon (and boron), c) potassium, d) chlorine, e) oxygen, f) calcium, g) silicon and h) aluminium maps.

4.3.2.3. Porosity measurement

The porosity of chemically activated sample was determined from isotherms of nitrogen adsorption measured at T = 77 K (Fig. 4.36). According to IUPAC classification all isotherms are of IIb type, characteristic for non-porous or macroporous adsorbents [4.15]. The sharp rise

of the adsorbed amount at low pressure (up to so called 'knee' or point B of the isotherm) corresponds to the formation of monomolecular layer of adsorptive on the sample' surface. At higher relative pressures p/p^0 the isotherm becomes quasi-linear. Such behaviour is characteristic to unrestricted multimolecular adsorption. The narrow hysteresis loop between adsorption and desorption branches of the isotherm that opens at the relative pressure $p/p^0 \sim 0.4$ is usually the result of inter-particle capillary condensation with non-rigid aggregated samples [4.15]. Therefore, adsorption measurements confirm that the porosity is created mainly by the mesoporous space between the agglomerates.
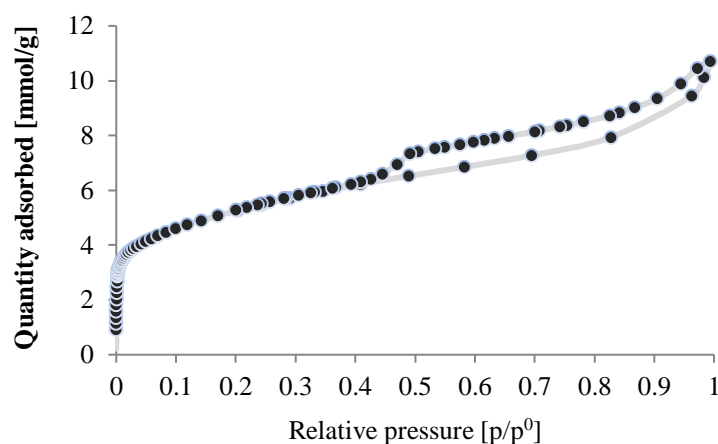

Figure 4.36. N_2 adsorption isotherm of boron-containing sample with 11.3 wt.% of B, activated with solid KOH.

Fig. 4.37 shows the distribution of pore sizes, determined using the Horvath-Kawazoe method [4.15] and assuming slit shape of the pores. The chemically activated sample contains mainly very narrow pores, of diameter from 6 Å to 8 Å. The micropore volume, estimated using t-plot method, is, as expected, low, around 0.11 cm^3/g.

The specific surface area of the sample calculated using BET method is also low, around 420 m^2/g. However, this value is 2 times larger than that of sample before activation (220 m^2/g). This is mainly due to the increase of micropore area (from 40 m^2/g to 230 m^2/g), whereas the external surface remained almost the same (~180 m^2/g before and after activation). Even those, this result is disappointing, as our goal is to prepare boron containing activated carbons with the specific surfaces larger than 3000 m^2/g. A better activation protocol has still to be developed.
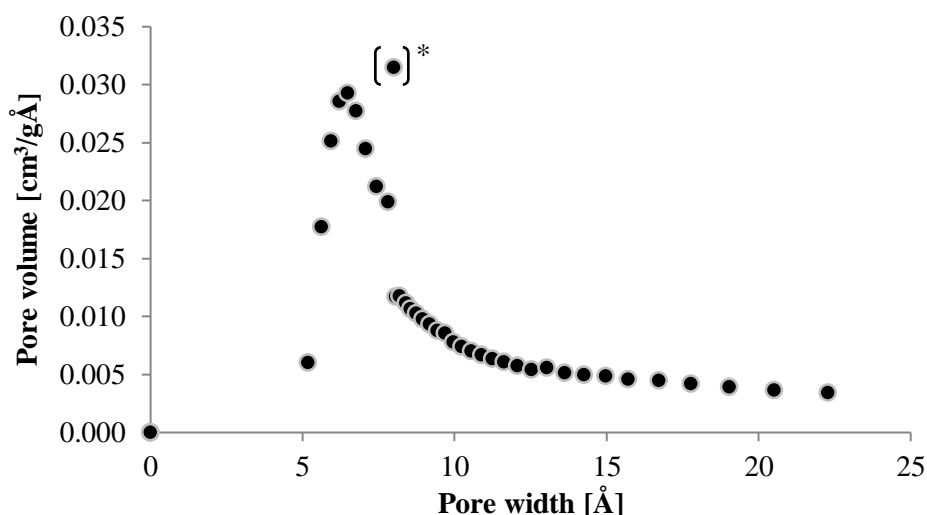
Figure 4.37. Pore size distribution of chemically activated boron-containing sample calculated from the Horvath-Kawazoe method and assuming slit shape of the pores; point marked with asterisk * is an artefact.

4.4. Summary

Synthesis of boron-carbon structures can be carried out by using electric arc discharge. Since boron is an insulator, the synthesis should be carried out under inert gas atmosphere and the pressure above 660 mbar (up to 800 mbar) to maintain plasma inside the reactor chamber.

The synthetized powder contains amorphous carbon and boron-like domains. HRTEM and XRD measurements indicate that the domains consist in boron carbide nanocrystals of ~10 nm of diameter, surrounded by graphene layers. According to MAS NMR results, they can also contain other boron compounds, such as BC_3 or boron nanoparticles.

Before activation boron-carbon samples have low SSA (around 200 m^2/g) and low microporous volume (0.02 cm^3/g for sample with the lower boron concentration). Activation (in particular chemical activation with KOH) slightly increases the porosity of boron-carbon powder. The SSA increases up to 420 m^2/g; microporous surface occupies 230 m^2/g which correspond to 80% increase with respect to its initial value. However, the result lowest than expected, probably due to the presence of boron-containing nanocrystals in the sample. Furthermore, we noticed that the activation procedures introduce many impurities into the samples and require optimization in terms of compounds and equipment used during the experiments.

Boron-carbon samples show high hydrogen adsorption energy, up to 9 kJ/mol. The energy is at least 60% higher than the one typical for activated carbons (4-6 kJ/mol).

4.5. Bibliography

[4.1] L. Firlej, Sz. Roszak, B. Kuchta, P. Pfeifer, C. Wexler, *Enhanced hydrogen adsorption in boron substituted carbon nanospaces*, J. Chem. Phys. 131, 164702, 2009

[4.2] N. P. Stadie, E. Billeter, L. Piveteau, K. V. Kravchyk, M. Dobeli, M. V. Kovalenko, *Direct synthesis of bulk boron-doped graphitic* carbon, Chem. Mater. 2017, 29, 3211−3218

[4.3] S. Turner, Y. Lu, S. D. Janssens, F. Da Pieve, D. Lamoen, J. Verbeeck, K. Haenen, P. Wagner, G. Van Tendeloo, *Local boron environment in B-doped nanocrystalline diamond films*, Nanoscale, 2012, 4, 5960

[4.4] T. Shirasaki, Alain Derré, M. Ménétrier, A. Tressaud, S. Flandrois, *Synthesis and characterization of boron-substituted carbons*, Carbon 38 (2000) 1461-1467

[4.5] J. Narayan, A. Bhauik, *Novel phase of carbon, ferromagnetism, and conversion into diamond*, Journal of Physics 118, 215303 (2015)

[4.6] L. S. Panchakarla, K. S. Subrahmanyam, S. K. Saha, A. Gobindaraj, H. R. Krishnamurthy, U. V. Waghmare, C. N. R. Rao, *Synthesis, structure, and properties of boron- and nitrogen-doped graphene*, Adv. Mater. 2009, 4726-4730

[4.7] R. Arenal, F.de la Pena, O. Stéphan, M.Walls, M.Tencé, A.Loiseau, C.Colliex, *Extending the analysis of EELS spectrum-imaging data, from elemental to bond mapping in complex nanostructures*, Ultramicroscopy 109 (2008) 32–38

[4.8] *Solid state chemistry techniques*, edited by A.K. Cheetham and P. Day, Oxford Science Publications, 1978, ISBN 0-19-855165-7

[4.9] F. Najafi, O. Moradi, M. Rajabi, M. Asif, I. Tyagi, S. Agarwal, V. Gupta, Thermodynamics of the adsorption of nickel ions from aqueous phase using graphene oxide and glycine functionalized graphene oxide, Journal of molecular liquids 208 (2015) 106-113

[4.10] M. Chen, J. W. McCauley, K. J. Hemker, *Shock-induced localized amorphization in boron carbide*, Science Vol. 299 (2003) 1563-1566

[4.11] H. I. Lee, J. H. Kim, D. J. You, J. E. Lee, J. M. Kim, W-S. Ahn, C. Pak, S. H. Joo, H. Chang, D. Seung, *Rational synthesis pathway for ordered mesoporous carbon with controllable 30- to 100- Angtrom pores*, Adv. Mater. 2008, 20, 757-762 (Aktywacja 4.3)

[4.12] A. Braun, M. Batsch, B. Schnyder, R. Kotz, O. Haas, H.-G. Haubold, G. Goerigk, *X-ray scattering and adsorption studies of thermally oxidized glassy carbon*, Journal of Non-Crystalline Solids 260 (1999) 1-14

[4.13] E. J. Kim, Y. Fei, S. K. Lee, *Probing carbon-bearing species and CO$_2$ inclusions in amorphous carbon-MgSiO3 enstatite reaction products at 1.5 GPa: Insights from 13C high resolution solide-state NMR*, American Mineralogist, Volume 101, pages 1113-1124, 2016

[4.14] D. Rohanova, A. R. Boccaccini, D. Horkavcova, P. Bozdechova, P. Bezdicka, M. Castoralova, *Is non-buffered DMEM solution a suitable medium for in vitro bioactivity tests?* J. Mater. Chem. B, 2014, 2, 5068

[4.15] F. Rouquerol, J. Rouquerol, K.S.W. Sing, P. Llewellyn, G. Maurin, *Adsorption by Powders and Porous Solids – Principles, Methodology and Applications*, 2nd edition 2014, Elsevier, ISBN: 978-0-08-097035-6

[4.16] S. Kaplan, F. Jansen, and M. Machonkin, *Characterization of amorphous carbonhydrogen films by solidstate nuclear magnetic resonance*, Applied Physics Letters 47, 750 (1985)

CHAPTER 5

Final conclusions and perspectives

We have shown that both: all-carbon and B-substituted carbon (BC_n) porous structures can be synthetized during the electric arc discharge between graphitic electrodes containing (or not) boron powder. The boron content in the resulting BC_n material can be finely controlled in the range from 0 to 25 wt.% by modyfing the boron content in the anode, and without compromising the continuity of electric discharge. The structure of produced carbons depends on the pressure of the inert gas (helium) inside the reaction vessel. At pressures close to 1 atm organized, closed carbon structures (fullerenes, nanotubes, nano-onions) are mainly formed, whereas at lower pressures (600-800 mbar) the reaction products contain mainly graphitized open structures. Low pressure of the gas inside the reactor does not have significant influence on porosity of produced material. The distribution of boron in the final products is not homogeneous. In addition to substitutional boron, boron clusters or nanocrystals were observed in all samples, independently on boron concentration in the electrode. Therefore, an additional experimental effort is necessary to improve the homogeneity of boron distribution and to increase the ratio of substitutional boron atoms in the graphitic structure. A 'brute force' approach would consist in systematic changing of synthesis conditions (type of gas in the reaction chamber, electric current during the discharge, composition of cathode…), seeking for the experimental parameters ensuring the desired boron dispersion in the synthetized material. Another way that we suggest is to explore the possibility to prepare the boron containing electrodes by compression of finely grinded, boron-graphite powders. This study was out of technical possibilities of the present work but should be performed in the future.

The as-prepared powders have low specific surface areas, of the order of 200 m^2/g and require activation. The efficacy of thermal and chemical activations has been tested for both: carbon and BC_n samples. Thermal activation at optimized conditions (annealing in air at 400 $^\circ$C for 4 hours) allowed to increase the surface area of the pure carbon samples up to 1000 m^2/g. This result can be probably further improved by carrying out the activation under dynamic (and not static) atmosphere, and changing the activation gas (steam, Ar, or CO_2 instead of air)

It was impossible to activate the BC_n powders: for all activation temperatures and annealing times the specific surface area increased insignificantly, up to ~ 300 m^2/g. We attribute this behaviour to the presence of boron clusters partially incorporated into carbon

network and preventing the activation agent (oxygen) to penetrate between carbon layers. The HRTEM and XRD analysis confirmed that the clusters (of the diameters up to 15 nm) are composed of stable boron carbide (B_4C) nanocrystals. We conclude that it will be difficult to remove them from the sample by any post-synthesis treatment, and stress again that there is the synthesis procedure that should be modified to avoid their formation in the future studies.

Similarly, chemical activation with KOH base appears to be efficient on pure carbon samples, but not on BC_n samples. The increase of specific surface area of boron containing samples depends on nominal content of boron in the material to activate and decreases for samples with higher boron concentration. This observation confirms our conclusions presented above: the penetration of activation agent between the graphene layers is limited when the pore entrance is obstructed by boron nanocrystals. Moreover, the activated samples contain a large number of impurities of various chemical nature (mainly calcium, aluminium and sodium), transferred probably during activation process from laboratory equipment (ceramic and metal mortars), and solvents used. Therefore, we consider that the protocol of chemical activation in solution, commonly used to produce activated carbons needs to be rewritten to avoid the use of solvents and optimized for solid state reactions. Ball milling technique, commonly used to homogenise the composition of the powders' mixtures and unify the size of nanoparticles may be a part of this new protocol, but the ball material has to be tested to avoid its transfer to the grinded samples.

The characterization techniques used in the present work (SEM, TEM, HRTEM, EELS, XRD) allowed the characterisation of morphology, crystallinity, and the distribution of boron atoms within the synthetized materials. The determination whether the boron atom is covalently bonded to the carbons and occupy a substitutional position in the graphene honeycomb structure is more difficult. A partial confirmation of the presence of C-B bonds in the prepared structures was obtained from HR NMR measurements. To better define atomic connections in the BC_n samples, the NMR study have to be completed by other measurements that are able to sense local environment of atoms (i.e. IR and Raman spectroscopy).

The most important result of the present work is the demonstration that boron containing nanoporous carbons prepared by electric arc discharge have isosteric heat of hydrogen adsorption of the order of 9 kJ/mol, almost twice as high as unsubstituted activated carbons (~5 kJ/mol). This result is reproducible and confirms theoretical and numerical studies suggesting

that activated carbons containing substitutional boron atoms in the graphene structure are today potentially the best candidates to store hydrogen by physical adsorption.

Summary

The intensive use of fossil fuels and the emission of combustion products (mostly CO_2) to air have already impacted global climate. We urgently need to find a technological solution to convert the global energy economy towards cleaner and renewable fuels. A possible solution consists in using hydrogen as energy vector. Today this technology is limited by the absence of material that could efficiently store hydrogen at ambient temperature and moderate pressures.

In this project we explore the possibility to prepare a new material for reversible hydrogen storage by physisorption: boron-substituted nanoporous carbons. We show that electric arc discharge synthesis may be optimized to produce graphitized structures with a variety of graphene fragment sizes, forms, and interconnections between them. The morphology, structure, chemical composition, and homogeneity of boron distribution over the carbon samples were characterized using SEM, HRTEM, EELS, and XRD techniques, and HR solid state NMR. The porosity and adsorption parameters were determined from isotherms of nitrogen adsorption at T = 77 K.

Two parameters that are essential for efficient hydrogen storage at ambient conditions are sorbent specific surface and the energy of gas adsorption at this surface. We show that material specific surface can be controlled and increased by thermal and/or chemical activation to enhance storage capacity, and that hydrogen adsorption energy in boron containing samples is twice as high as in all-carbon material.

==

Résumé

L'utilisation intensive des combustibles fossiles et l'émission des produits de leur combustion (principalement du CO_2) dans l'air ont déjà impacté le climat mondial. Trouver des solutions technologiques permettant la conversion de l'économie mondiale aux carburants propres et renouvelables devient urgent. Une de possibilités consiste en utilisation de l'hydrogène comme un vecteur d'énergie. Aujourd'hui elle est limitée par l'absence d'un matériau permettant son stockage à des températures ambiantes et à des pressions modérées.

Dans ce projet, nous explorons la possibilité de préparer un nouveau matériau pour un stockage réversible de l'hydrogène par physisorption : les carbones nanoporeux substitués au bore. Nous montrons que la synthèse en arc électrique peut être optimisée pour produire des structures graphitisées, avec la variété de tailles, de formes et d'interconnexions entre les fragments de graphène. Leur morphologie, structure, composition chimique et homogénéité de la distribution de l'hétéroatome dans la structure carbonée ont été caractérisés par les techniques SEM, HRTEM, EELS, XRD et spectroscopie RMN. La porosité et propriétés adsorptives ont été étudiées en utilisant les mesures d'adsorption de l'azote à T= 77 K.

Les deux paramètres essentiels pour un stockage efficace de l'hydrogène dans les conditions ambiantes sont la surface spécifique de l'adsorbant et l'énergie avec laquelle les molécules du gaz sont adsorbées sur cette surface. Nous montrons que la surface spécifique d'adsorption peut être contrôlée et augmentée par une activation thermique ou chimique pour optimiser le stockage, et que la présence du bore dans les structures carbonées permet de doubler l'énergie d'adsorption d'hydrogène du matériau.